Modelling extended SSD and large field dosimetry for Total Body Irradiation

Phillip Duncan-Gelder

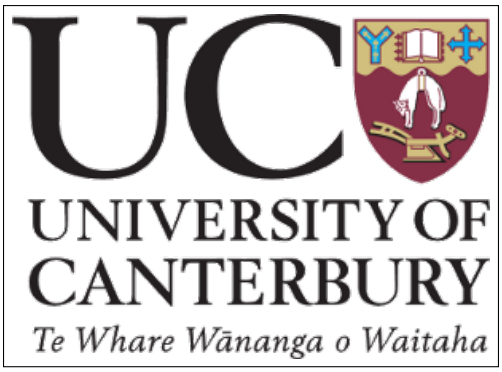

A thesis submitted for the degree of Master of Science
at the University of Canterbury, Christchurch, New Zealand.

April 2020

Abstract

This thesis describes modelling of the extended source to surface distance (341 cm and 432.6 cm SSDs) Total Body Irradiation technique used at Christchurch Hospital. Measured results are compared with manual and commercial treatment planning calculated results using both simple block phantom and complex anthropomorphic phantom setups.

A Phantom Mobility Device was developed and validated in order to improve upon the simple block phantom measurement technique in terms of both measurement speed and accuracy. The device was implemented and used to measure dose profiles and tissue phantom ratios for comparison to treatment planning system results.

Modelled results from the Monaco treatment planning system were calculated by a specifically-developed approach to the use of the software. Results from the simple block-type phantom incorporated both Monte Carlo and Collapsed Cone Convolution algorithms with these results qualitatively compared. The Monte Carlo algorithm was found to be noisy at extended SSD and therefore only the Collapsed Cone Convolution algorithm was used for the more complex anthropomorphic phantom.

Linear accelerator measurements were conducted to mirror the modelled results in terms of setup geometry so direct comparisons could be made. Wall scatter and monitor unit drift were also measured to correct for the inherent uncertainties these quantities introduce to aid comparisons with treatment planning modelled results.

Dose difference at various points were used as a metric for comparing the agreement between measured and modelled results. The feasibility of using Monaco as a treatment planning system was shown by block-phantom comparisons being clinically acceptable over a wide range of depths and distances off-axis, with minimal constraints. Whilst clinical use of Monaco could not be fully established due to limitations in the data attained from anthropomorphic phantom measurements, a description of proposed improvements to guide future work are described.

Acknowledgements

First of all I would like to thank my supervisors Dr. Steven Marsh and Dr. Alicia Moggré, for the incredible support throughout my Master's project, and particularly over the last few weeks. Their enthusiasm and vast knowledge of the field both academically and clinically have helped me learn a great deal in a short time span. Alicia, you have always inspired me to do better and be better, and Steve your sense of humour never fails to impress.

Dr. Andrew Cousins, for his scientific advice and participation in the project despite an incredibly heavy workload, and for fostering an energetic and positive environment where independence and collaboration are promoted. This type of environment is where I personally work best, and therefore to have been a part of it has been fantastic. I will never forget the 10 letters of the pirate's alphabet: I, I, R, and the seven C's.

Geoffrey Graham at the University of Canterbury workshop has played a significant part in this project. Thank you for helping design and develop the Phantom Mobility Device, as without it, or you, this project would not have been possible.

Ben Wilder has played a large part in the work of this thesis with his role being somewhere between co-worker and supervisor, he has contributed to many insightful discussions with this project. Thank you for the brilliant medical physics discussions which have helped me consolidate and broaden my knowledge base, the help when linacs have had various issues late at night, and for the help and support especially towards the end of the project when I needed it most.

Thanks also to David Little for his diverse knowledge of Monaco, helping import necessary beam models into Monaco, and for the great discussions about wine making. I have yet to try that pear wine of yours. Florentina Baluti, thank you for many valuable discussions about the project, medical physics in general, and making useful suggestions. Abby Rajasekar thanks for the continued moral support through the thesis and providing useful insights.

Additionally there are many members of staff at Christchurch Hospital who have considerably contributed, whether it be in discussing the project, answering medical physics questions, or help with setup. Victoria Beenstock for valuable input both scientifically and in formatting. Dr. Anna Arns, Jackson Roberts, Gemma Warner, Beat Billson, Dr. Nicola Thomas, Dr. Paul Ronaldson, Grace Healy, Christine Reed, and Tom Telford for all your amazing support and willingness to participate in discussion of this project. The radiation therapists and patients at Christchurch Hospital for allowing me to observe TBI treatments to get a better understanding of clinical setup.

I wouldn't be where I am today without the love and support of all my friends and family. Thank you for providing opportunities to relax, and thank you for making the time especially when finding the time was often difficult.

Contents

List of Figures

List of Tables

List of Acronyms

2D Two Dimensional.

3D Three Dimensional.

CCC Collapsed Cone Convolution.

CT Computed Tomography.

DD Percentage Dose Difference.

DOF Diode Orientation Factor.

eSSD Extended Source to Surface Distance.

linac Linear Accelerator.

MC Monte Carlo.

MU Monitor Units.

PDD Percentage Depth Dose.

PMD Phantom Mobility Device.

RGB Red Green Blue Colors.

RO Radiation Oncologist.

SAD Source to Axis Distance.

SCD Source to Chamber Distance.

SPD Source to Point Distance.

SSD Source to Surface Distance.

TBI Total Body Irradiation.

TPR Tissue Phantom Ratio.

Chapter 1

Introduction

Cancer is a leading cause of death in New Zealand, with 9063 total number of deaths in 2013 (corresponding to 30.7 % total deaths).[2,3] There were 22,166 new cases of cancer registered in 2013, with this number expected to increase over time with an ageing population. Blood cancers are the 4th largest group of registered cases with 2872 new cases in 2013 (13 % of total registrations).[2] Radiation therapy, also known as radiotherapy is a treatment technique which uses ionising radiation to kill cancer cells in the body. This technique is highly effective, with over 50 % of cancer patients receiving radiation therapy treatments.[4]

Total body irradiation (TBI) is a specialized treatment technique which delivers a radiation dose to a patient's whole body. TBI is used to treat patients with Acute and Chronic Lymphoblastic Leukemias (ALL and CLL), Myeloblastic Leukemias (AML and CML), Non-Hodgkin's Lymphomas (NHL), and for bone marrow transplants (BMTs, preventing immunological rejection of the transplanted marrow). A large surface total (effective) dose (typically between 12 Gy to 15 Gy) is delivered to kill as many lymphoblastic and myeloblastic cells as possible to suppress or destroy a patients immune system and malignant cells prior to receiving a bone marrow transplant.[5] Modern TBI treatment involves the use of external beam radiotherapy (EBRT) machines called linear accelerators (linacs), these machines are capable of delivering targeted radiation therapy treatments with millimeter accuracy and precision to kill tumorous tissues. To minimize harmful side effects (toxicities) during TBI treatments like interstitial pneumonitis (IP), treatments are often delivered in smaller doses over two or more sessions (called fractionations, or fractions of the effective dose).[6,7,8] For photon treatments using linacs, a spectrum of photon energies are produced (polyenergetic beam), therefore the beam is usually described in terms of its accelerating potential (in MV) which is equal to the peak energy of the spectrum (in MeV). Through this thesis, where energy is quantified in MV, it refers to the nominal peak energy of the photon spectrum.

Context and Motivation

The goal of TBI is to eradicate the patient's immune system therefore a dose delivered to the whole body is ideal. The maximum collimator size of most linacs is 40 cm × 40 cm, therefore producing a field-size large enough to cover the whole of the patient's body requires some geometrical setup modification to produce a larger effective field size. There are many methods that have been implemented to produce an effective field size large enough and with minimal toxicities for useful TBI treatment. These techniques include Volumetric Modulated Arc Therapy (VMAT),[9] sweeping beam,[10] translating couch[11] and many others.[12] At Christchurch Hospital an extended source to surface distance (eSSD) technique is used to maximise the radiation field. There are two treatment rooms, a primary treatment room (T2) with an eSSD of 432.6 cm with beam energy of 15 MV, and a backup treatment room (T1) with an eSSD of 341 cm and beam energy of 10 MV. Bilaterally opposed fields are used with the linac gantry rotated at a 90° angle to produce a horizontal beam, the collimator is rotated at 45° to produce a rotated square field shape which maximises the horizontal field size. Two fields are used by rotating the treatment couch after each part of a fraction to deliver dose to both lateral sides of the patient. The patient lies on their back (supine) on a treatment couch between two 2 cm thick beam spoilers with ricebags packed around the patient to produce a block-phantom like geometry comparable to commissioning measurements (illustrated later by Fig. 2.8).

Radiation dosimetry enables measurement of absorbed dose to a medium (usually water or water equivalent material), resulting from exposure to directly or indirectly ionising radiation. When a medium is exposed to a source of incident ionising radiation, there are several interactions which may occur and impart energy to the medium including Compton scattering, the photoelectric effect, pair production, and electronic interactions like bremsstrahlung production. The probability of each type of interaction, and the energy imparted to the medium are dependent on the initial energy, the type of interaction, and the tissue composition. Radiation dose interacts with biological tissue causing primarily DNA strand breaks which results in damage to cells leading to cellular death. It is challenging to measure the biological effects of radiation accurately in human tissue from a safety and ethics point of view, therefore water or water equivalent material is often used as it provides a consistent approximation of human tissue in terms of density. Radiation doses are therefore calculated in terms of their absorbed dose to water in units of Gray (Gy) where:

$$1\,\mathrm{Gy} = 1\,\mathrm{J\,kg^{-1}} \tag{1.1}$$

Accurate and reproducible radiation dose measurements are essential for the comparison and discussion about worldwide treatment outcomes in radiation therapy. Primary standard dosimetry labs (PSDLs) based around the world determine absolute dose values and issue calibration certificates regularly, this provides the link between detectors used for measuring radiation quantities in the hospital to the primary standard which ensures comparability of absolute dose between different clinics. For stan-

dard treatments like intensity modulated radiotherapy (IMRT), a ±5 % accuracy of dose is recommended for optimal patient outcome. However since achieving an even dose distribution in TBI treatment is difficult difficult to achieve, the established tolerable total dose accuracy is ±10 % for external beam bilaterally opposed fields as established by the TG-17 report.[13,14] There are many different methods of measuring absorbed dose to a medium, these each have their advantages and limitations and will be discussed in Sec. 2.1.

1.1.1 Objectives

The work in this thesis has two primary aims. The first is the development of an apparatus to improve the current methodology in measuring TBI characteristic field data (commissioning data), followed by an investigation of scattering conditions and using the device in practice. The second focus is to investigate whether the Monaco treatment planning system (TPS) can be validated and used at eSSD by comparing with measurement under various conditions.

Before we begin discussing the details of this work it is necessary to frame it within the current practice at Christchurch Hospital. This section provides a brief discussion on how both the development of a device to measure radiation dose profiles called the Phantom Mobility Device (PMD), and the validation of the Monaco TPS were motivated, and how they can be incorporated into the present clinical setting.

Part of the commissioning process of a linac usually involves the measurement of radiation dose profiles in a large water phantom which can encompass the full radiation field size for typical isocentric treatments. At eSSD a water tank which would encompass the full field size would need to be 100 cm × 60 cm × 30 cm (length × width × height), which is impractically large. Rather than using a large water tank, previous commissioning results were measured by physically moving a heavy 28.4 cm × 30 cm × 30 cm standard water tank (used for isocentric measurement) on a sticky TBI couch positioned using a tape measure. This resulted in a large positional uncertainty of ±2 cm both at depth and off axis. Additional uncertainties resulting from the time taken to complete all profile measurements, such as the change in ambient conditions or setup errors further increased the total commissioning uncertainty. To constrain this uncertainty, the question of whether a PMD which could accurately move blocks of water equivalent material and a detector to various points off-axis in a timely manner could be built to improve upon existing measurement methodology.

With common treatments like IMRT or three-dimensional conformal radiotherapy (3D-CRT), the Monaco treatment planning system (TPS) is used for planning delivered dose to target tumours. For TBI treatments however, the existing TPS model has not been validated beyond 80 cm to 110 cm SSDs. Instead, TBI treatment planning currently consists of a spreadsheet calculation based on a simplified geometric (block-phantom) model of the patient in accordance with AAPM TG-17.[13] The spreadsheet determines the number of MU to prescribe based on the prescribed dose to the midline (along the midsaggital line of the patient), and the maximum allowable lung dose set by the Radiation

Oncologist (RO). The spreadsheet takes into account rice bag packing, spoilers and the effective path length radiation through the lungs based on their respective densities. However since patients bodies and ricebag packing are both non-uniform, there exists several inhomogeneities which this model does not take into account. Treatment planning systems utilize the electron densities of tissue determined from imported computed tomography (CT) scans of a patient to determine dose given to inhomogeneous structures. It would therefore be ideal if the existing treatment planning model could reliably determine doses in a patient at eSSD to provide a planning system for TBI. There is therefore a requirement to characterise the extent of agreement between the TPS model and measured dosimetric results.

The research in this thesis presents novel findings, as whilst there have been many groups publishing about Monaco treatment planning models[15,16,17] and extended SSD TBI models validated using other TPSs like Pinnacle[18,19] and Eclipse[20], there have been no published results characterising the Monaco TPS for clinical use in eSSD TBI conditions.

1.1.2 Thesis Overview

The goals of this research were to improve upon current methodology of measuring commissioning results in block-phantom geometries, and to determine whether the Monaco TPS could be used for clinical TBI treatment planning. This project spans a variety of different subject areas including radiation dosimetry and medical physics, to software and device engineering and mathematical modelling. Necessary concepts will be introduced in a comprehensive manner in order of their significance which will allow for an understanding of the subject by those without specialist background. Chapter 2 provides an overview of radiation dosimetry, radiation therapy, treatment planning systems and algorithms with the aim of providing an understanding of the methodology for measuring dose, and how different treatment planning algorithms predict dose in a patient. Chapter 3 provides a comprehensive look at the development of a new device (PMD) for measuring radiation dose profiles in TBI conditions. This chapter will overview software development and the validation of the PMD with relevant dosimetry equipment. Chapter 4 presents a discussion on the available processes for the prediction of dose in block and anthropomorphic phantoms within Monaco. Chapter 5 progresses through all linac measurements intended for subsequent comparison to Monaco, these allow us to draw conclusions appropriately. Chapter 6 compares and contrasts TPS modelled results in Chapter 4 with linac measurements in Chapter 5, and discusses the outcomes of the research in terms of whether Monaco can be used for TBI treatment planning clinically, and the effectiveness of the PMD for TBI commissioning.

Peer-Reviewed Publication

1. Feasibility results from Chapter 6 of this work were presented at the New Zealand Physics and Engineering in Medicine (NZPEM) 2020 conference in Hamilton, New Zealand under the title "Feasibility of modelling extended SSD and large field dosimetry in Monaco for Total Body Irra-

diation (TBI)".[21].

2. Results from Chapters 3-6 have been submitted to Physica Medica under the title of "Feasibility of modelling extended SSD and large field dosimetry in Monaco for Total Body Irradiation".

Chapter 2

Background

The work in this thesis involves a number of important concepts which span several different areas of radiation oncology medical physics. It is important to introduce these concepts as they provide a basis for understanding the methods, results, discussions and conclusions made throughout the thesis. This section aims to provide an overview of the relevant background starting with an introduction to dosimetry, from particle interactions to kerma, cavity theory, and how Farmer chamber dosimetry relies on these concepts. These are followed by an overview of common dosimeters used, concepts used in modern radiation therapy practice, and finally the local treatment practice of TBI at Christchurch Hospital is provided.

Dosimetry

Dosimetry is the measurement and determination of the amount of ionizing radiation absorbed by a material. Absorbed dose (D) is a quantity which describes the energy an ionizing radiation source imparts to a medium. The absorbed dose to a point is defined as the mean energy $d\bar{E}$ imparted to a unit mass dm given by Eq. 2.1 below. Absorbed dose has units of Gray (Gy), defined as 1 joule of energy per kilogram of mass.

$$D = \frac{d\bar{E}}{dm} \tag{2.1}$$

A large portion of the work presented involves the measurement of dose. It is therefore vital to understand the key aspects of dosimetry, the particle interactions which contribute to the total dose, and the dosimeters used. This section will start with a brief overview of key particle interactions, followed by how dose to a medium is determined, cavity theory will then be introduced, and finally an overview of the dosimeters used is given. These aim to provide a clearer picture as to what dose is, how it is measured, and the considerations made for quantities which may contribute to dose.

2.1.1 Particle Interactions

The experimental work in Ch. 3 and Ch. 5 involves a number of important concepts in radiation physics as they apply to modern treatment techniques. A few different concepts will be discussed in terms of particle interactions with absorbing media and their impact on obtained and compared results. The understanding of these interactions is crucial for their discussion, and to set an appropriate basis for conclusions of this thesis. Particle interactions in volumes have been covered in-depth by many standard textbooks,[22,23,24,25] the following sections will summarise the necessary theory and results for discussion points throughout this thesis along with providing the foundation for understanding radiation dosimetry.

2.1.1.1 Photon Interactions

Photons with energies above 10 eV have sufficient energy to ionise atoms.[26] These interactions are indirectly ionising as, rather than directly producing ion pairs, photons interact with particles and the coulomb field of an absorber atom and deposit excitation energy, resulting in the emission of particles and/or photons. Photonic interactions are important not only for understanding how dose is deposited to a medium, but also for the understanding of scattered radiation. Scatter occurs when a photon interacts with an absorber atom and an interaction causes the photon to change its direction (and hence momentum). This direction change results in the photon being scattered at a scattering angle θ best shown by Fig. 2.1 . This section will provide a brief overview of photon interactions with a medium so that a fundamental understanding of dose and scatter are developed.

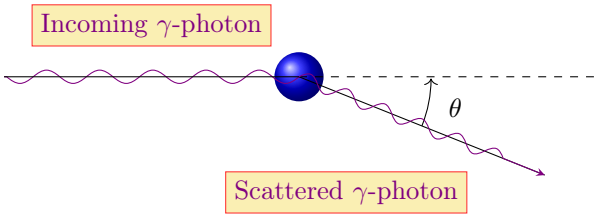

Figure 2.1: Scattering diagram showing a simple example of Rayleigh photon scattering on an atom (blue) with scattering angle θ.

Rayleigh scattering otherwise known as Coherent scattering occurs when a photon interacts with orbital electrons of an absorber atom. The photon is scattered at an angle θ with the photon's energy change being very small thus the recoil energy of the absorber atom is also small. The atom is not excited or ionised as a result of this interaction and therefore the angles the photons are scattered by are small especially for energies where $h\nu > 1\,\text{MeV}$, where ν is the photon frequency and h is the Planck constant. At lower energies and materials with increasing atomic number (Z) the angular distribution (commonly known as the Rayleigh characteristic angle, θ_R representing the half-angle of a cone which contains 75 % of Rayleigh-scattered photons) of scattered photons increases, however is

confined to $\theta_R(E = 0.1\,\text{MeV}, Z < 82) \leq 70°$. The Rayleigh characteristic angle is approximated by Eq. 2.2 expanded from Hubbell.[27]

$$\theta_R \approx 2\arcsin\left(\frac{0.026Z^{(1/3)}(m_e c^2)}{h\nu}\right) \tag{2.2}$$

Compton scattering occurs when a photon of energy $h\nu$ interacts with a loosely bound (electron shell binding energy E_B is much less than incident photon energy $h\nu$, $E_B \ll h\nu$) orbital electron of an absorber atom. Theoretically it is assumed since the electron is loosely bound that the photon effectively interacts with a "free and stationary electron". As a result of this interaction two products are realized: a scattered photon with reduced energy $h\nu'$, and a scattered electron also known as a "recoil" or "Compton" electron having kinetic energy E_K. The resulting scattered photon energy can be described as a function of its scattering angle and incident photon energy described by Eq. 2.3.

$$h\nu' = \frac{h\nu}{1 + \frac{h\nu}{m_e c^2}(1 - \cos\theta)} \tag{2.3}$$

For energies above 100 keV, the Compton effect becomes the dominant form of photon interaction. When high-energy ($h\nu > 10\,\text{MeV}$) photons undergo Compton scattering, most of the incident energy is given to the recoil electron, as shown in Fig. 2.2. This is important as the work relating to this thesis involves photon energies in the 1 MeV to 15 MeV range, therefore Compton scattering and its relative energy transfer is important for us to understand and discuss later on.

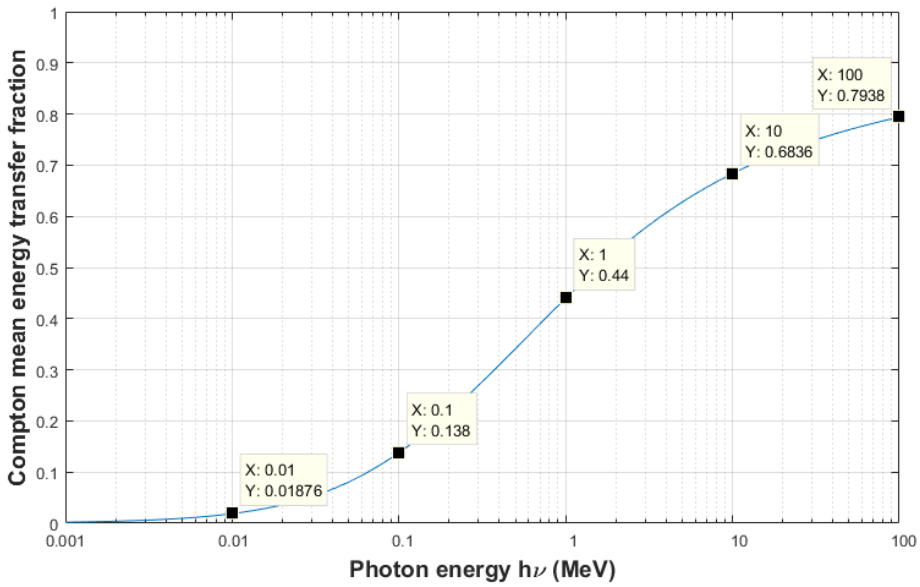

Figure 2.2: Graph of the mean energy transferred to recoil electrons, commonly known as "The Compton graph" showing the mean energy transfer fraction against incident photon energy $h\nu$ from 1 keV to 100 MeV.

Photoelectric absorption is a process where a photon of energy $h\nu$ interacts with a tightly bound

(electron shell binding energy less than but similar to that of the incident photon energy, $E_B \lesssim h\nu$) electron of an absorber atom.[23] The incident photon is completely absorbed, and the electron is ejected from the atom as a photoelectron with kinetic energy given by Eq. 2.4.

$$E_K = h\nu - E_B \tag{2.4}$$

Pair production occurs when an incident photon with energy $h\nu$ exceeds specific threshold energies when interacting with an absorber atom, the production of an electron-positron pair is possible by its Coulomb field interaction with either the absorber atom's nucleus called Nuclear Pair Production (NPP), or orbital electron commonly called Electronic Pair Production or Triplet Production (TP). For NPP this threshold energy is $h\nu > 2m_e c^2$ and results in an electron-positron pair with the photon completely absorbed. However for TP the threshold energy is $h\nu > 4m_e c^2$, and results in two electrons and a positron also with the photon completely absorbed. The derivations for the threshold energies are determined by using the energy-momentum relation as invariant. The produced pair or triplet are emitted at symmetrical angles.

Photoneutron production occurs when an energetic photon interacts directly with the nucleus of an absorbing atom causing nuclear disintegration. Nuclear disintegration results in the emission of a single neutron through a (γ, n) reaction. Since photonuclear reactions are endothermic, there are specific threshold energies required for specific atomic numbers of an absorber. Therefore linac beam energy and material of the linac, bunker, shielding, apparatus and patient are all important factors. These threshold energies are why photoneutrons are only considered for linac energies above 10 MV.

The atomic energy cross section for photonuclear reactions have a broad peak called a giant resonance extending from their threshold energy, this then diminishes from the peak as energy increases. This cross section is relatively small compared with competing processes amounting to only a few percent of the total electronic cross section, even at its giant resonance peak.[23] It is therefore usually assumed negligible in photon attenuation studies. Horikawa et al.[28] show that for angles between $90° < \theta < 270°$ neutron intensity further decreases and therefore backscattered neutrons are less likely than forward scattered neutrons.

2.1.1.2 Electron Interactions

When a charged particle such as an electron traverses an absorbing medium, Coulomb force interactions occur between the electron and the absorber's atoms and their orbital electrons. These interactions can be split into three different types: soft, hard and bremsstrahlung interactions depending on the particle's trajectory, and its distance from the center of the atom (also known as the impact parameter b) relative to the classical atomic radius a of the absorber atom.

Soft collisions occur when a charged particle traversing the absorber medium has an impact parameter b much greater than the classical atomic radius a such that $b \gg a$. In this case, the charged particle interacts via Coulomb forces with the entire absorber atom and its orbital electrons. These interactions

are low in energy transfer (as we know from classical electrodynamics that $F \propto \frac{1}{r^2}$ with r being the distance between two charges), however in a conventional medium the number of these interactions is large and accounts for approximately 50 % of the energy transferred to the absorbing medium. Soft collisions result in the transfer of energy from the traversing charged particle to the absorber atom, as a result the absorber atom can be excited to a higher energy state, or ionised by the ejection of an orbital electron.

Hard collisions occur when a charged particle traversing the absorber atom has an impact parameter b similar to the classical atomic radius a such that $b \approx a$. Hard collisions may result in a significant amount of energy being transferred by Coulomb interaction between the charged particle and an orbital electron of an absorber atom. Upon interaction, the orbital electron will be ejected from its atom traversing the medium as a δ-ray which can also undergo its own Coulomb interactions with the medium. Due to the narrow range of distances where this interaction would occur, the number of hard collisions a charged particle would experience is generally small (unlike soft collisions). Since the energy transferred between the charged particle and orbital electron is large however, approximately 50 % of the energy transferred to the absorbing medium comes as a result of hard collisions (similar to soft collisions). The maximum energy transferred between the charged particle and the δ-ray is described by Eq. 2.5.

$$\Delta E_{max} = \frac{1}{2}(E_K)_i \tag{2.5}$$

Bremsstrahlung interactions occur when the impact parameter b of the charged particle is much smaller than the atomic radius a of the absorbing medium such that $b \ll a$. When a charged particle follows this trajectory, it will primarily interact by Coulomb forces with the nucleus of the atom itself. Most of these interactions are elastic scattering events which only cause a negligible change in energy and possibly a change in direction. A small number of interactions are inelastic resulting in a significant energy loss for the charged particle followed by the emission of x-ray photons also known as Bremsstrahlung photons. This is known as a Bremsstrahlung interaction.

2.1.2 Kerma and Absorbed Dose

The above processes transfer energy to a medium, for the determination of dose, this energy transfer needs to be quantified. The kinetic energy released per unit mass (kerma) is a quantity defined for indirectly ionising radiation types (photons and neutrons) as mean energy transferred $d\bar{E}_{tr}$ by photons or neutrons to charged particles per unit mass dm of the absorbing medium. There are two types of kerma: radiative kerma K_{rad} and collision kerma K_{col} both having units of $\mathrm{J\,kg^{-1}}$. Radiative kerma is defined where a charged particle produced by a photon interaction (secondary particle) undergoes a bremsstrahlung interaction and the resulting bremsstrahlung photon has sufficient energy to leave the medium and thus its energy is not absorbed by the medium. Collision kerma is defined where secondary charged particles interact by soft or hard collisions where the medium absorbs the energy of the secondary charged particle (energy transferred from the charged particle to the absorber). The total

kerma for photons is the sum of the radiative and collision parts. Kerma is best described by Eq. 2.6 and Eq. 2.7.

$$K_{med} = \frac{d\bar{E}_{tr}}{dm} \tag{2.6}$$

$$K_{med} = K_{med}^{col} + K_{med}^{rad} \tag{2.7}$$

Absorbed Dose D_{med} is a similar concept to kerma, however rather than energy transferred it is defined as the mean energy absorbed $d\bar{E}_{ab}$ by the medium of mass dm (or energy imparted by ionising radiation to the medium). Directly ionising radiation types (charged particles) can directly impart energy to the medium through collision processes previously discussed. However for indirectly ionising radiation types (photons and neutrons) this is a two part process: firstly energy is transferred to a secondary charged particle, secondly this charged particle will then traverse the medium and impart its energy to the medium. Absorbed dose has a special unit called the Gray (Gy) where $1\,\mathrm{Gy} = 1\,\mathrm{J\,kg^{-1}}$.

2.1.3 Cavity Theory

Ionisation chambers and their use in measuring dose (dosimetry) are used for a large part of this thesis, and the principles of their operation are described in Sec. 2.1.4.1. Cavity theory applies directly to how absorbed dose is determined from measured charge and/or charge rate by an ionisation chamber. Therefore it is vital to develop the necessary concepts which make up cavity theory, as they apply directly for the considerations we need to make when measuring dose using ionisation chambers. This section will introduce the concept of charged particle equilibrium, stopping power, and the Bragg-Gray and Spencer-Attix cavity theories with the aim of providing an introduction to how dose is determined using ionisation chambers, and some potential limitations of ionisation chamber dosimetry.

2.1.3.1 Charged Particle Equilibrium and Transient Charged Particle Equilibrium

As previously discussed, when photons travel through an absorbing medium they may interact with the atoms of the medium through various interactions where secondary charged particles (positrons and electrons) may be released into the medium. A special case of these secondary charged particles known as charged particle equilibrium (CPE) can exist under certain conditions. If CPE exists, then the sum of all secondary charged particles with energies E_K which enter a medium of volume V is equal to the sum of all secondary charged particles which leave the volume V with equal kinetic energies E_K. Under CPE, energy in volume V is balanced in "equilibrium", as the energy lost by secondary electrons which leave the medium is replenished by the energy of secondary electrons entering the medium. CPE is shown schematically by Fig. 2.3.

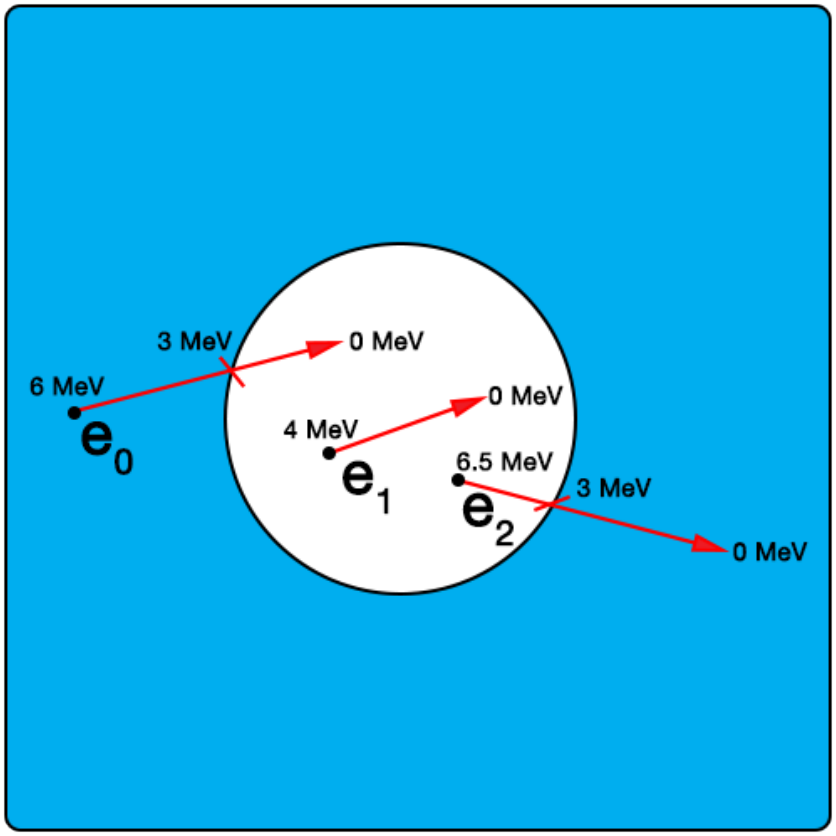

Figure 2.3: Diagram illustrating CPE in a medium. Monoenergetic photons which are not shown are irradiating a block of material shown in blue, the white circle within represents a sphere of volume V. Secondary charged particles produced (black) are shown with their tracks in red, initial and final energy and the energy where they cross the boundary into or out of V.

The three charged particle tracks shown with respect to CPE existing are;

1. charged particle e_0 entering the volume V with energy of 3 MeV and depositing all remaining energy within V.
2. charged particle e_1 produced in volume V and depositing all of its energy within V.
3. charged particle e_2 produced in volume V leaving V with energy of 3 MeV.

This demonstrates CPE, as the sum of all charged particles entering V is equal to the sum of charged particles which leave V and the sum of energy of charged particles entering V is equal to the sum of energy of charged particles leaving V.

In the case where CPE exists, this means that the dose deposited in V, D_{med} is equal to the collision kerma K_{med}^{col} in V.

$$D_{med} \overset{\text{TCPE}}{=} K_{med}^{col}(1 + \mu\bar{x}) \tag{2.8}$$

A more realistic description of charged particle equilibrium for high energy beams ($h\nu > 3\,\text{MV}$) is the concept of transient charged particle equilibrium (TCPE). TCPE exists for depths $z > z_{max}$ where a relationship exists between in-air dose and collision kerma in air and substituting this relationship into the CPE equality. The transient relationship between dose and collision kerma is given by Eq. 2.8, where μ is the effective attenuation coefficient of the medium and $\bar{x}$ is the mean-free path electrons transport their energy across the medium in the beam direction. The buildup regions exists where TCPE does not exist in the region where $z < z_{max}$. The depth where TCPE is established is energy-dependent. For energies 10 MV and 15 MV, the depths where TCPE is established are approximately 2.5 cm and 3 cm respectively.[23]

2.1.3.2 Stopping Power

The Bragg-Gray and Spencer-Attix cavity theories discussed later in Sec. 2.1.3.3 rely on the concept of stopping power, it is therefore important to provide a simple conceptual introduction. Stopping power is a quantity which describes the energy loss of a charged particle per unit path length of an absorbing medium it travels through. Since interactions between electrons and absorbers can be split into collision and radiative processes, there are two different respective stopping powers S_{col} and S_{rad}. S_{col} decreases for increasing Z of an absorber whereas S_{rad} increases for increasing Z. The collision stopping power is described by the corrected Bethe equation, in Eq. 2.9.[29,30]

$$S_{col} = 4\pi \frac{N_A}{A} \left(\frac{e^2}{4\pi\epsilon_0} \right)^2 \frac{z^2}{m_e c^2 \beta^2} Z \left\{ \ln \frac{2m_e c^2}{I} + \ln \frac{\beta^2}{1-\beta^2} - \beta^2 - \frac{C}{Z} - \delta \right\} \tag{2.9}$$

where:

I is the mean ionisation energy.

Z is the atomic number of the absorber.

A is the mass number of the absorber.

z is the atomic number of the charged particle (for electrons and positrons this is 1).

β is the speed of the particle relative to the speed of light, $\frac{v}{c}$.

C/Z is the shell correction factor.

δ is Fermi's density correction factor.

2.1.3.3 Bragg-Gray and Spencer-Attix Cavity Theories

The determination of absorbed dose in a medium such as a water or a tissue-equivalent phantom involves placing a radiation dosimeter (cavity) within the phantom. The absorbed dose to the cavity D_{cav} can then be measured. Usually the dosimeter cavity is a different medium to the external phantom (for example, air-cavities within tissue-equivalent phantoms) where absorbed dose to a point D_{med} is to be determined. This difference in medium can lead to the cavity perturbing the photon and charged particle fluence in the phantom leading to inaccuracies in the measurement of D_{med}. The Bragg-Gray

and Spencer-Attix cavity theories deal with the complex relationship between D_{med} and D_{cav} such that dosimeters can be used accurately for the measurement of dose within other mediums. This section will discuss the Bragg-Gray and Spencer-Attix conditions and what these mean for radiation dosimetry in cavity dosimeters.

For a cavity to be classified as a Bragg-Gray cavity for photons with an energy $h\nu > 200keV$, two conditions must be met which are as follows:

1. The size of the cavity, d must be much smaller than the range of secondary charged particles, R which cross it ($d \ll R$). This condition avoids the cavity perturbing the secondary charged particle fluence produced by photon interactions within the medium so that the secondary charged particle fluence of the cavity is approximately equal to that of the medium ($\varphi_{cav} \approx \varphi_{med}$). small cavities also provide better spatial resolution of measurements.

2. The absorbed dose in the cavity, D_{cav} is deposited solely by secondary charged particles crossing the cavity. Photon interactions are ignored as they are rare and therefore negligible.

These conditions allow for the relationship between dose and charge to be established as follows:

$$D_{med} = \frac{Q}{m_{air}} \left(\frac{\bar{W}}{e}\right) \left(\frac{\bar{S}}{\rho}\right)_{air}^{med} \tag{2.10}$$

The Spencer-Attix cavity theory extends the Bragg-Gray theory for small cavities by establishing an energy threshold for secondary charged particles in the medium. This threshold energy means that secondary charged particles which have enough energy to produce bremsstrahlung photons which can carry energy outside of the cavity are excluded. To do this, a mean restricted mass collision stopping power ($\frac{\bar{L}_\Delta}{\rho}$) with kinetic energy threshold Δ of 10 keV replaces the unrestricted mass collision stopping power ($\frac{\bar{S}}{\rho}$) in Eq. 2.10.

The Bragg-Gray cavity theory establishes a well understood method for which absolute dose can be determined in a small air cavity which is representative of a dose in the medium it is placed within. The Spencer-Attix extension of the Bragg-Gray theory to exclude higher energy electrons increases the accuracy of the determination of dose significantly therefore allowing for the appropriate determination of absolute dose in modern ionisation chambers.

2.1.4 Dosimeters

Three different dosimeters are used in Ch. 5 for the measurement of dose in block-phantoms and anthropomorphic phantoms. This section will provide an overview of the dosimeters used, starting with Farmer-type ionisation chambers, followed by radiochromic film, and ending with diodes. The goal is to provide an understanding of how these dosimeters work, how they are used, and their drawbacks.

2.1.4.1 Farmer-type Ionisation Chambers

Farmer chambers are a type of thimble ionisation chamber, that consist of a cylindrical thimble-shaped wall and a cavity with typically $0.6\,\mathrm{cm}^3$ air volume. A central and outer electrode with a polarizing voltage applied to the outer electrode with the central electrode grounded, generates an electric field between the two electrodes. As secondary electrons produced in a larger external volume cross the sensitive volume of ambient air inside the chamber they ionise it causing electrons and positions to be produced, which are separated by the electric field across the electrodes. Depending on the polarity of the voltage applied, a positive or negative charge will then be recorded by an electrometer over time.

There are several advantages and disadvantages of Farmer chambers. Advantages include: High accuracy and precision, simplicity of measurement and reproducibility, flat energy response over a wide range of energies, negligible directional dependence, instant readout, able to determine absolute dose, correction factors and cavity physics well understood. Disadvantages include: spatial resolution limited by collection volume, leakage currents from the chamber, electrometer and cable, non-water equivalent chamber materials and medium so many correction factors need to be applied, high voltage supply required.

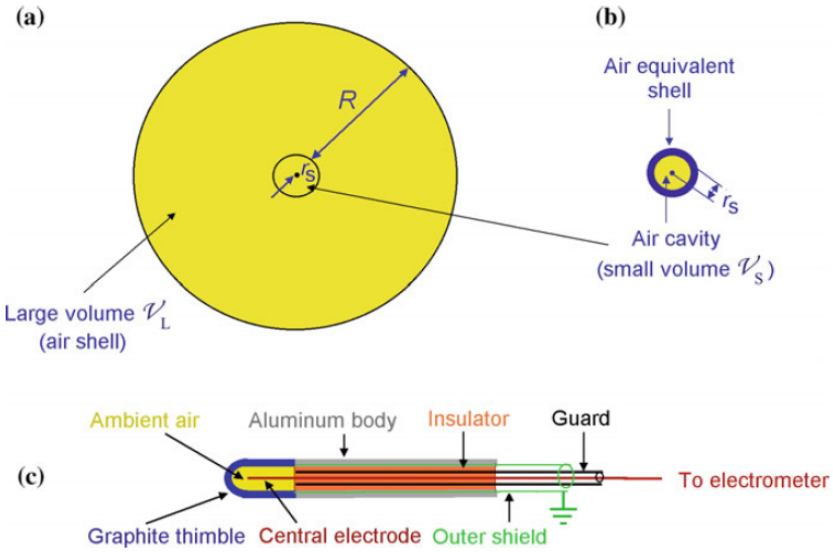

Figure 2.4: Schematic diagram of farmer chamber operation. (a) Shows the air cavity within a larger volume V_L which could be any measurement medium. (b) Represents the cross section of the cylindrical Farmer chamber with central and outer electrodes in blue. (c) Illustrates the entire farmer chamber. (Reproduced from Podgorsak EB. Radiation Physics for Medical Physicists. Springer Publishing, 2016, with permission)

Fig. 2.4 illustrates schematically the internal components of a farmer chamber in a medium of volume V_L. The volume V_L may be air, water, or any other type of medium the chamber measures a dose within. We have previously discussed the Bragg-Gray and Spencer-Attix cavity theories and

how they consider the perturbation of electron and photon fluence by the cavity within the medium. An expression for absorbed dose to the medium based on the charge measured by a farmer chamber is provided by Eq. 2.11.

$$D_{med} = \frac{Q}{m_{air}} \left(\frac{\bar{W}}{e} \right) \left(\frac{\bar{L}_{\Delta}}{\rho} \right)_{air}^{med} \tag{2.11}$$

Where Q is the charge produced in the chamber cavity, m_{air} is the mass of air within the chamber cavity, $\left(\frac{\bar{W}}{e}\right)$ is the mean energy required to produce an ion pair in air and $\left(\frac{\bar{L}}{\rho}\right)_{air}^{med}$ is the restricted mass stopping power ratio of the medium of volume V_L to the air in the cavity.

The concept of TCPE is important for the accuracy of farmer chamber dosimetry as the measure of charge or charge rate from secondary charged particles ionising air depends on the energy and fluence equilibrium of charged particles in the cavity. As previously mentioned when TCPE does not exist, the relationship between collision kerma and absorbed dose does not hold and therefore the measured charge or charge rate for depth $z < z_{max}$ would not be representative of dose.

In clinical practice, quantities such as stopping power ratio and mean energy required to produce an ion pair are not measured, instead a secondary standards dosimetry lab (SSDL) which have equipment calibrated to a PSDL, perform calibrations for and provide calibration coefficients for a given chamber in clinical use. These calibration coefficients include the absorbed dose per nano coulomb to water $N_{D,w,Q}$, and the radiation quality coefficient k_{Q,Q_0} which corrects for the differences in SSDL and treatment centre beam qualities. There are a few other centre-measured factors such as k_{pol} the response of an ion chamber with respect to its polarizing voltage, k_{TP} corrects for the chamber response based on changes in ambient pressure and temperature, k_s corrects for lack of total charge collection due to recombination of produced ion pairs. These correction factors fit in with IAEA's TRS-398 $N_{D,w}$ formalism[31] for the determination of absorbed dose to water in high-energy photon and electron beams using an ionisation chamber. Calculating absorbed dose to water using this formalism is done using Eq. 2.12.

$$D_w = N_{D,w,Q_0} \times M_Q \times k_{Q,Q_0} \times k_{TP} \times k_s \times k_{pol} \tag{2.12}$$

Where M_Q is the charge measured by an electrometer and D_w is the absorbed dose to water.

Of note is the interchangeability of charge and dose to charge rate and dose rate, as if we substitute charge for charge rate, $\dot{M}_Q$ then the calculated quantity is absorbed dose rate to water $\dot{D}_w$. Additionally, the derivation of Δk_{TP} from k_{TP} is given by Eq. 2.13, this is important for later discussion of small variations of temperature and pressure in terms of the correction factor.

$$\begin{aligned} k_{TP} &= \frac{P_0 \times T}{P \times T_0} \\ \Delta k_{TP} &= \frac{P_0 \times \Delta T}{P \times T_0} - \frac{P_0 \times T \times \Delta P}{T_0 \times P^2} \end{aligned} \tag{2.13}$$

2.1.4.2 Radiochromic Film

Radiochromic film dosimetry is a type of chemical dosimetry based on the change in colour of radiation sensitive film when exposed to ionising radiation. Dose is inferred from the film's colour change. The film develops in real time with no post-exposure treatment required. To determine dose the film is scanned on a flatbed scanner where the amount of light which is transmitted through the film is directly related to the dose of ionising radiation absorbed by the film, and by the scanning light's wavelength. For absolute dosimetry measurement, a set of calibration film is typically required along with an absolute measure of dose to the calibration point to generate a calibration curve for which the relationship between dose and the three colour channels (red, green and blue) can be established. Once this relationship has been established this can be used to determine the absorbed dose for a measurement.

The advantages of radiochromic film are that they are near tissue equivalent (effective Z between 6.0 and 6.5 compared with approximately 7.42 for water[32] which is a reasonable approximate for human tissue in its entirety), have a high spatial resolution, large dynamic range, relatively low energy dependence in the MV range, insensitive to ambient conditions during measurement and allows for 2D dose mapping. Disadvantages include: non-instant readout, determination of absolute dose requires careful calibration, reproducibility difficult to achieve between differing film batches. Several studies evaluate the Gafchromic EBT-3 radiochromic film used in this thesis[33,34,35] in terms of the compositions, lateral response artifacts, sensitivities, resolution and energy-dependence over a range of doses for photon beams.

2.1.4.3 Diode Detectors

Silicon diode detectors are a common choice used for relative dosimetry due to their higher sensitivity, instantaneous output and small size compared with ionisation chambers. Their major limitations include energy dependence in photon beams, directional dependence, thermal effects and radiation-induced loss of sensitivity over time. Modern diodes used in dosimetry have been made to reduce negative effects and are well suited for relative measurements, output constancy checks and in-vivo patient dose monitoring. Diodes are currently often used for in-vivo patient dose monitoring during TBI treatments.

Radiation Therapy Quantities in Practice

Given a linac beam incident on a patient or phantom, the absorbed dose varies dependent on a number of factors. This variation includes beam energy, depth, field size, distance from the source, beam collimators, scatter and changes in ambient conditions. The determination of dose in a patient requires considerations and understanding with respect to these parameters and impacts. It is therefore essential to establish the variation of dose along the central axis and off-axis of the beam at varying depths in a patient or phantom. A number of quantities have been defined for this purpose which will be explored in this section, along with other quantities and terms in radiation therapy used through this thesis.

Monitor Units are a measure of beam output from a linac as measured by an ionisation chamber within the linac head called a monitor unit chamber. linacs are calibrated such that their nominal output at 100 cm SAD at 10 cm depth in water is 1 cGy MU^{-1}. This means for every monitor unit delivered, 1 cGy of dose is delivered to a point 10 cm deep in water at 100 cm SAD.

Dose profiles are a measure of dose at a perpendicular plane transverse to the radiation beam direction. Profiles provide an understanding of the variation of dose as a measurement point moves away from the beam's center (central axis shown schematically in Fig. 2.5), or off-axis. Since linacs produce a 3D dose which can be visualised as a 2D dose profile there are two primary profile directions: inline where off-axis deviations are inline with the gantry and crossline with off-axis deviations perpendicular to the gantry.

Percentage depth doses (PDDs) quantify how dose varies with depth in a phantom and distance from a radiation source. The PDD is determined by measuring doses at varying depths within a phantom with a fixed source to surface distance (SSD). For a given phantom and linac setup, determined PDDs are a function of field size, energy, depth, and SSD.

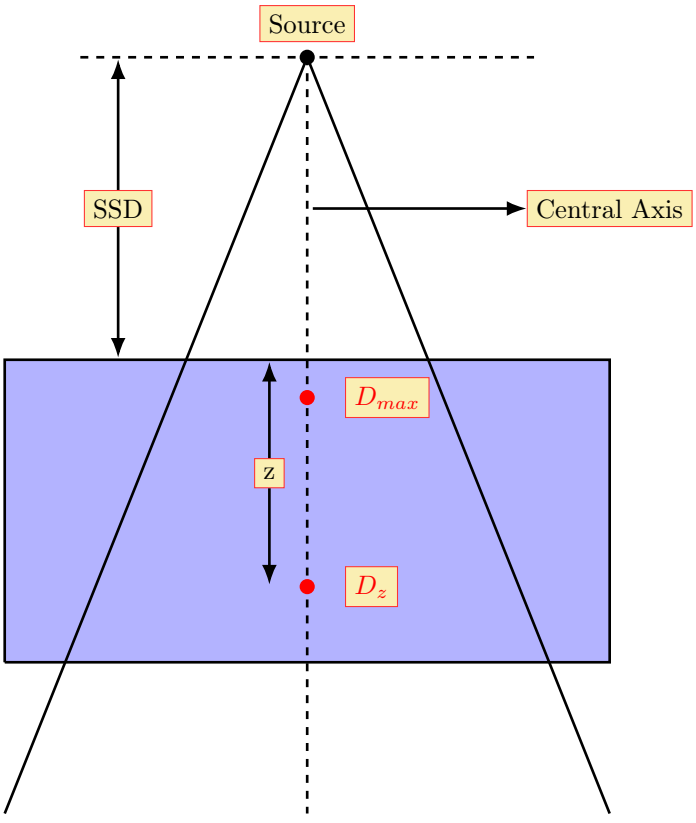

Figure 2.5: Setup for measuring a PDD showing schematically the SSD, depth z and doses D_z, D_{max} in a water phantom.

Tissue phantom ratios (TPRs) quantify how depth within a phantom affects the dose to a point for a fixed source to axis distance (SAD) best illustrated by Fig. 2.6. The TPR is acquired by measuring

doses at a reference depth and alternative depths whilst keeping the SAD fixed. Doses at the alternative depths are then divided by the dose at the reference depth to determine the TPR as given by Eq. 2.14.

$$TPR(h\nu, z) = \frac{D_z}{D_{z_{ref}}} \tag{2.14}$$

Where D_z is dose at alternative depths z and $D_{z_{ref}}$ is dose at the reference depth as shown by Fig. 2.6 below.

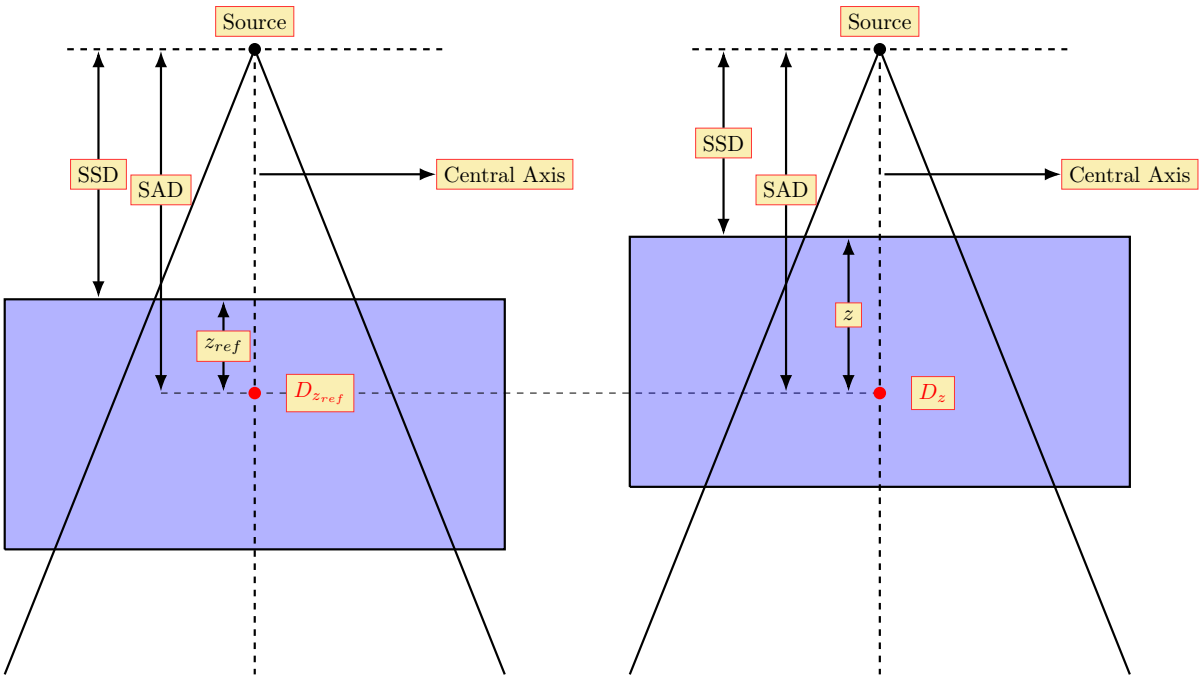

Figure 2.6: Tissue phantom ratio diagram showing schematically the SSD, SAD, depth z and doses D_z, D_{ref} in a water phantom. This illustrates that for SAD to remain fixed that the SSD must change when determining the TPR at each depth.

Off-Axis Ratios (OARs) relate the ratio of the dose for a given depth at distances away from CAX given by Eq. 2.15. The OAR is dependent on the field size, beam energy, depth and off-axis distance. The plot of off-axis factors for a given depth including the CAX point is known as the beam profile.

$$OAR(h\nu, A, z, x) = \frac{D_{z,x}}{D_{z,x=0}} \tag{2.15}$$

Where $D_{z,x}$ is the dose at depth z and off-axis distance x, and $D_{z,x=0}$ dose at depth z at CAX.

Output Off-Axis Ratios (OOARs) are a similar concept to the OAR, however rather than normalizing doses off-axis to the CAX point for each depth, the doses are normalized to the point where output is determined. Output is typically determined at CAX and at a depth of 10 cm in a water or solidwater phantom. OOAR is determined using Eq. 2.16 and much like OAR depends on depth, field size, beam energy and off-axis distance.

$$OOAR(h\nu, A, z, x) = \frac{D_{z,x}}{D_{z_o,x=0}} \tag{2.16}$$

Where $D_{z,x}$ is the dose at depth z and off-axis distance x, and $D_{z_o,x=0}$ dose at output depth z_o at CAX.

The OOAR is clinically useful concept when calculated from measured data, as it provides a lookup table where dose can be determined directly from the table, and is proportional to the number of MU delivered (subject to treatment correction factors). The OOAR is essentially a dose profile of all TPRs at the output point. The plot of OOARs vs off-axis distance or depth is still a dose profile or TPR (respectively), they have however a different point of normalization (which is more clinically relevant).
Percentage Dose Differences (DDs) are a quantity defined for the comparison between two or more doses and their agreement with one another.

$$DD(\%) = 100 \times \frac{D_1 - D_2}{MAX(D_1, D_2)} \tag{2.17}$$

Where D_1 and D_2 are doses at two different spatial points in a radiation field. These doses can be absolute, relative, or normalized doses with the dose difference reflecting the difference between the quantities at different points relative to their maximum.
The clinically useful field size or dosimetrically useful field size is defined as an effective field size which achieves a 95 % isodose coverage of the phantom or patient, for TBI purposes. This means that the whole patient is covered by 95 % of the total dose.

Treatment Planning Algorithms and Systems

Treatment planning in radiation therapy represents a major part of the overall treatment process. TPSs are used to generate beam shapes and dose distributions to maximize dose delivered to a tumour and minimize dose to healthy normal tissue. There are a number of different approaches modern TPSs use for determining dose within the patient, several algorithms and methods have been developed for the calculation of dose each with their own advantages and drawbacks. These algorithms and methods include Monte-Carlo (MC), Collapsed Cone Convolution (CCC), Pencil Beam Convolution (PBC), Analytical Anisotropic Algorithm (AAA) to name a few. The Monaco TPS used through this thesis uses two primary algorithms: CCC and MC. This section will discuss the MC and CCC algorithms generally, and then conclude by comparing the algorithms as they are implemented in Monaco.

2.3.1 Monte Carlo Simulation

Monte Carlo simulation (MC) is an important concept in RT treatment planning. The MC method is a broad methodology of simulation using defined randomness as input such that it is possible to emulate a real system with many coupled degrees of freedom or where inherent randomness exists. In an MC dose calculation, tracks of each ionising particle passing through a medium are simulated.[36] Particle interactions with the medium are simulated along the track using a random number generator and the

probability distribution of the different interaction types that may occur given the particle's energy. Interactions are simulated along the track until the particle has lost all of its energy via interactions with the medium. For the calculation of dose to a given volume of interest (VOI) the algorithm just needs to determine the change in energy for particles traversing the VOI divided by its total mass. For the simulation of dose deposition many primary particles and their associated secondaries are tracked until all the energy is either absorbed or leaves the simulated world. Accuracy of results is improved by increasing the number of simulated primaries (commonly referred to as histories).

2.3.2 Collapsed Cone Convolution Algorithm

Collapsed Cone Convolution (CCC) algorithms were developed to provide a faster means of determining expected dose to VOIs whilst maintaining a suitable ($\leq 2\,\%$)[37] difference from the true dose. The CCC algorithm works in three primary steps: Photons are first ray traced through the medium (consisting of volumetric segments called voxels). As photons interact with the medium, energy is transferred to the medium and its voxels, collectively called the total energy released per unit mass (TERMA).[38] Secondly the interactions in the voxels produce secondary electrons which traverse in all directions and transfer their energies to nearby voxels. The energies transferred to voxels from an interaction point is accumulated into a kernel (which is typically pre-calculated with MC simulations). Finally the total dose deposited in the medium can be determined via the convolution of the TERMA distribution with the kernel.

2.3.3 Monaco Treatment Planning System

Monaco is a treatment planning system developed by Elekta (Elekta AB, Stockholm, Sweden) which incorporates PBC, CCC, and MC algorithms for calculation of dose to VOIs. Christchurch Hospital primarily uses CCC and MC in treatment planning practice, and it has been shown in other TPSs that, for eSSD TBI and for lung dose calculations, PBC performs significantly worse than CCC and MC algorithms.[19,37] Therefore it was deemed for this thesis that only the existing CCC and MC algorithms (validated up to 110 cm SSD), would be evaluated.

Monaco uses VMC++ for its MC calculation of dose. VMC++ is a unique implementation whereby particles of the same energy but different position are bundled into sets called particle sets. A simple transport equation is formulated based on stopping power and the continuous slowing down approximation of charged particles, whereby a particle transport equation of interactions with the medium can be formulated in terms of energy rather than path length. This, with the combination of electron track history repetition from homogeneous media, means that VMC++ proves to be significantly more efficient than a standard MC simulation.[39] The model, whilst more efficient, does take several aforementioned shortcuts which may make it unusable at eSSD.

CCC calculation of dose in Monaco is performed using the technique discussed in Sec. 2.3.2. Since pre-calculated kernels are used, if these do not extend beyond 110 cm SSD this may cause errors in the

calculation of dose. An advantage of CCC however is the use of ray tracing. Since photons are ray traced through media, this may enable CCC to accurately compute interaction points at eSSD.

It is unclear which algorithm will perform the best at eSSD. One of the central aims of this thesis is to evaluate both algorithms at eSSD in a homogeneous phantom.

Local Treatment Practice of TBI

This section covers the local practice of TBI, starting with common equipment used, followed by introducing current TBI treatment planning, then discussing how patients are setup for treatment and finally discussing in-vivo dosimetry used for checking doses during treatment.

2.4.1 Common Equipment Used

There are several key items of equipment used for measurement of dosimetric quantities in this thesis. This section provides a quick reference to these pieces of equipment, along with shorthand names used through the thesis for them.

- Solid Water HE commonly referred to as "blue solid water", Original Solid Water commonly referred to as "brown solid water" both produced by Sun Nuclear Corporation.[40,41]
- 0.6cc NE2571A farmer chamber (Phoenix Dosimetry Ltd.)[42]
- PTW UNIDOS E T10009 Electrometer.[43]
- PTW T41023 water tank.[44]
- Two linacs are used, an Elekta Synergy (in treatment room 1) and an Elekta Versa HD (in treatment room 2).[45,46]
- RANDO Alderson (Radiology Support Devices Inc.[1]) Anthropomorphic phantom.

2.4.2 Treatment Planning

TBI Treatment planning currently consists of a spreadsheet calculation using a simplified geometric model using commissioned profiles and TPRs. The spreadsheet calculates dose along the patient midline along with the maximum lung dose. As mentioned these calculations are based on a simplified model and do not take into account things like inhomogeneities, full tissue scatter conditions, and variations in organ sizes and positions.

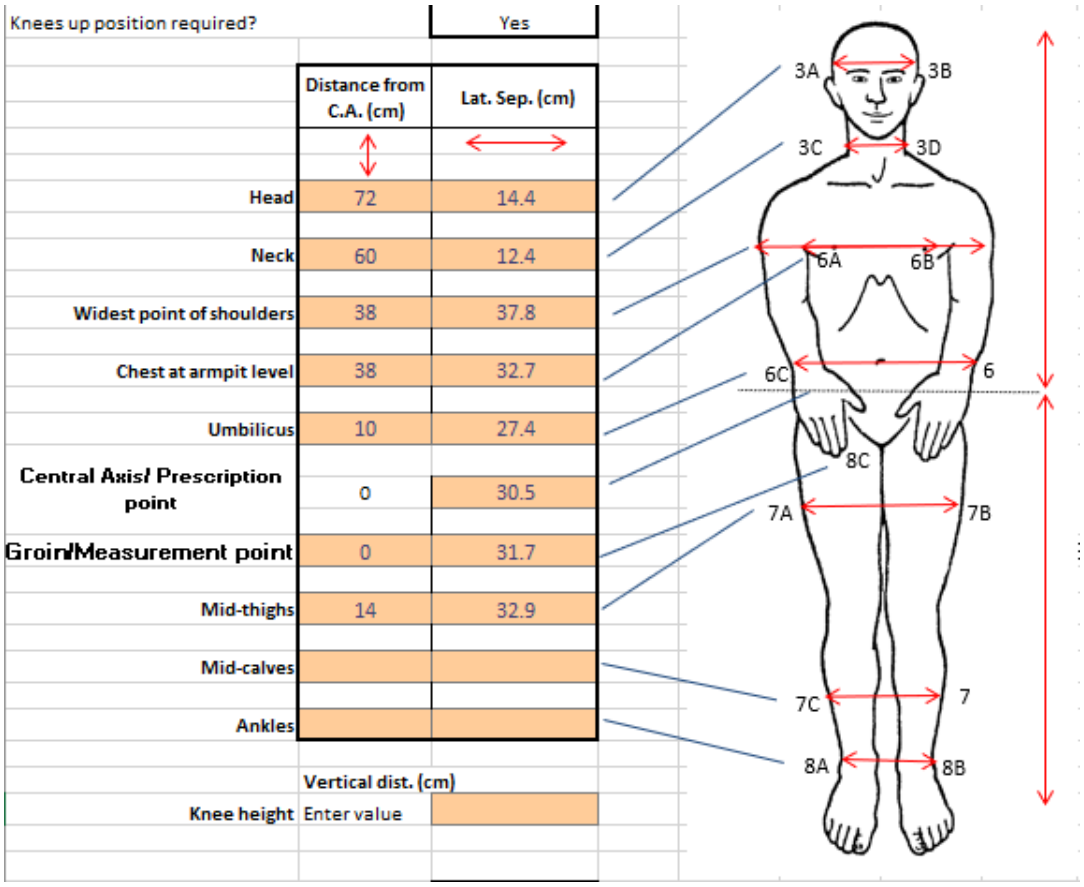

Figure 2.7: Schematic of the TBI calculation spreadsheet showing patient dimensions measured prior to treatment.

Patient dimensions are physically measured prior to treatment and values are entered into the spreadsheet, best illustrated by Fig. 2.7. The allowed lung maximum dose and prescribed midline dose are entered along with patient-specific information. Expected midline doses are then determined along with the number of monitor units to use for field and the perspex side panel separation. This information is then saved and used during patient setup.

2.4.3 Patient Setup

The current TBI treatment technique at Christchurch Hospital involves opposed bilateral fields to a patient lying supine at eSSD. The gantry is rotated at 90° and collimators angled at 45° such that the long-axis of the patient is in line with the diagonal of the field this is best shown by Fig. 2.8. Two treatment configurations are currently used;

1. Treatment room T1 (T1) with 10 MV photon energy and SMD of 341.0 cm with dosimetrically useful field size of 120 cm.
2. Treatment room T2 (T2) with 15 MV photon energy and SMD of 432.6 cm with dosimetrically useful field size of 170 cm.

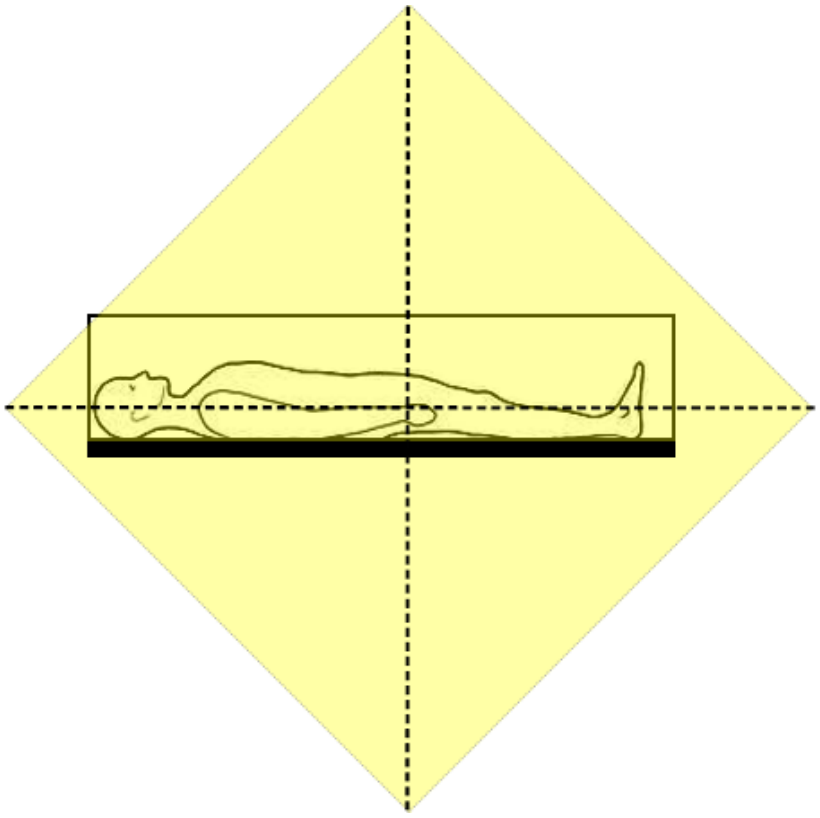

Figure 2.8: Schematic of TBI patient setup viewed from the beam's eye view. The yellow represents the diamond-shaped radiation field defined by the collimator at a 45° angle. Dashed lines represent the beams axis and cross over at the groin midline prescription point. The black solid rectangle outline around the patient represents the beam spoilers with ricebags packed within to make a uniform 3D rectangular volume.

Patients treated on T1 have to bend their legs at the knees, Patients treated in T2 can usually lie flat (unless they are taller than 170 cm). The midline CAX dose rate is in the range of 5 cGy/min to 15 cGy/min. Rice bags packed around the patient are used as a dose distribution modifier (bolus) to minimize the variation in midline doses due to changes in patient lateral separation. From previous measurements, the rice bags were found to have the following attenuation factors:

1. T1 (10 MV x-rays): 0.891
2. T2 (15 MV x-rays): 0.880

Two 2 cm thick perspex side panels cover the length of the patient and act as beam spoilers in order to increase the electron fluence hence removing skin sparing effect of the high energy beams. These spoilers have attenuation factors of:

1. T1 (10 MV x-rays): 0.993
2. T2 (15 MV x-rays): 0.992

2.4.4 In-vivo Dosimetry

In-vivo dosimetry involves using dosimeters to measure radiation dose to the patient during treatment. During TBI treatments, diode dosimeters (discussed in Sec. 2.1.4.3) and a farmer chamber are used for in-vivo dose verification. Diodes are placed at key locations on the entrance and exit to the head, neck, chest, umbilicus, mid-thighs, mid-calves and ankles and the farmer chamber is placed in the groin with a single groin diode taped to the thigh closest to the beam. Diodes are calibrated yearly to be within a 2 % tolerance with respect to dose measured.

Diode and farmer chamber measurements are compared with spreadsheet calculations for validation that predicted midline doses are within ±10 % of the measured midline doses (determined by interpolating measured diode results), and the farmer chamber prescription point dose.

Chapter 3

Phantom, Phantom Mobility Device, and Dosimetry

This chapter discusses the development of the Phantom Mobility Device (PMD) and validation of equipment used for measuring dose. Firstly we will outline the purpose of the development of the PMD, followed by the design and considerations. Software development will then be discussed, followed by the validation of dosimetric equipment and the PMD. Finally a brief section about the implementation of the PMD into the clinic will be given providing a reference to the produced protocol document.

Purpose

We have previously introduced that localization uncertainties during the TBI commissioning measurements of profiles and TPRs in a block phantom were relatively large ($\pm 2\,\text{cm}$). To reduce this uncertainty in the measurement point, a device which would move a water tank, or blocks of solid water, along with a detector, was devised. This section discusses the design, validation and implementation of the PMD and dosimetry related to its automation.

Design

A device was developed using a belt-drive system for movement of blocks of solid water material. Previously a worm-drive design was considered for movement of the phantom, but considering an estimated weight of $60\,\text{kg}$ (excluding the tray) and the total length of the drive ($2\,\text{m}$), there was concern about possible flexing in the centre causing additional localization uncertainty and instability over a long period. This is why the belt-fed system was chosen as the final design.

(a)

(b)

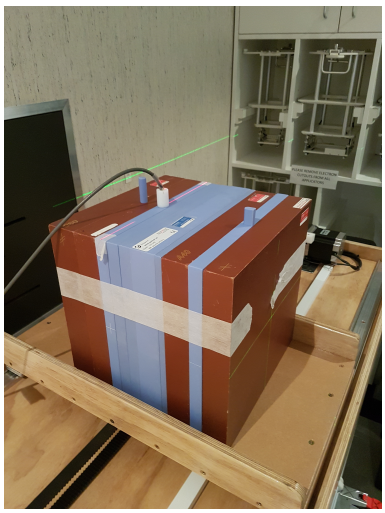

Figure 3.1: Image of the final PMD design (a) shows a full complete view of the PMD and control box (white). (b) Demonstrates the PMD in-use, filled with solid water.

Fig. 3.1 shows the final design featuring a belt-fed track system with a wooden tray supporting blocks of solid water, this sits on a large frame which fits atop of the treatment couch. The inner free area of this tray was 600 mm × 300 mm such that solid water can fit onto the tray and can be stacked in all 3 directions. The belt mechanism was driven by a stepper motor with resolution of 0.015 mm/step, controlled using an RS232 interface, allowing for the automation of measurements since both the movement and electrometer read-out are interfaced digitally over RS232. The entire assembly is an overlay sitting on-top of the bare treatment couch, thus the corner of the overlay could be kept at the same corner of the couch, thus allowing for repeat measurements over multiple days/weeks without sacrificing measurement-point localization accuracy.

The PMD was built by Geoffrey (Geoff) Graham at the University of Canterbury physics workshop. Final design was decided on after discussions of material type, the mechanisms used and their sustainability in an environment subjected to ionising radiation, and the design in terms of how it would be applied and used to constrain measurement uncertainty as much as possible.

Software Development

A program written primarily in C# named TBIControl was developed to interface with the PMD and electrometer over RS232. TBIControl made the process of measuring profiles and TPRs semi-autonomous. This section covers a few key points of what was included in the software as this is important for the reproducibility of results in this thesis. The code and compiled binary is linked in Appendix D.

3.3.1 Main Menu

The main menu of TBIControl is focused on connecting the necessary equipment via RS232 and validating the equipment is connected. RS232 is connected to by selecting the relavent port in the dropdown menu beneath the respective PMD and electrometer and pressing the "connect" button. Once connected a handshake output may be received (if configured in the options for the handshake command), this handshake may be a serial number of the device or something similar (user-configurable) and will output to the read-only text box beneath the connection options. To disconnect simply "close" the connection via the red button next to the connect, this will free up the COM port. Fig. 3.2 illustrates these menu options.

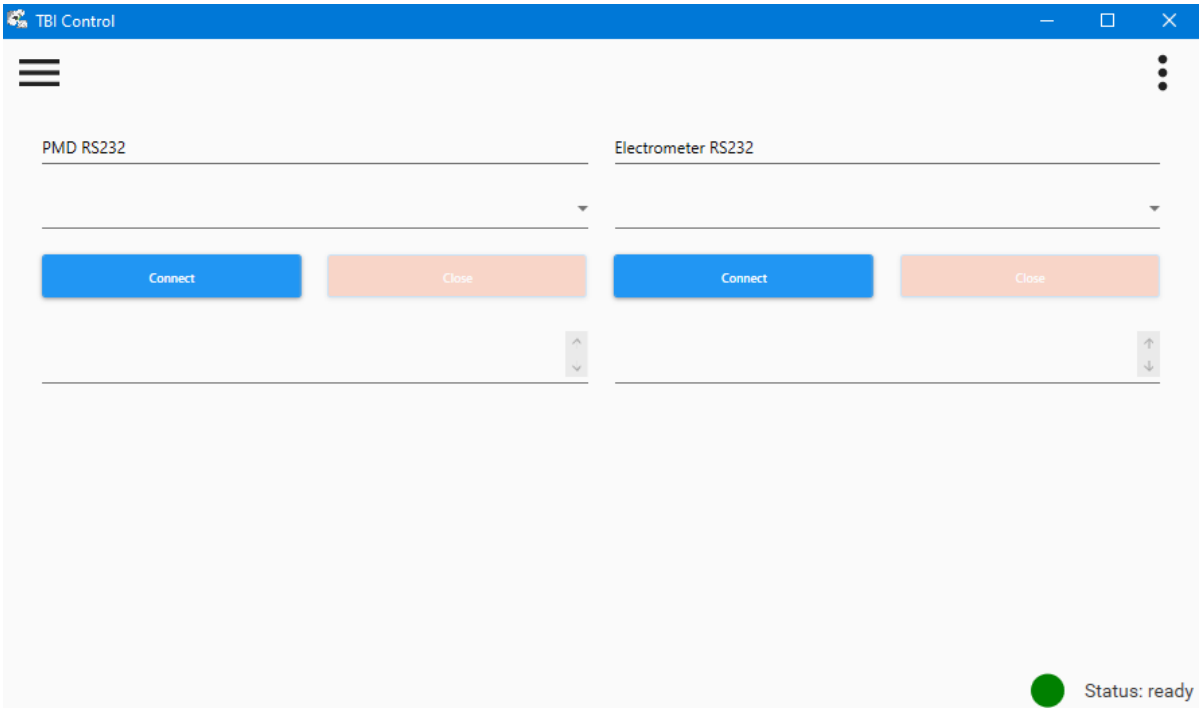

Figure 3.2: Image of TBIControl's main menu showing PMD and electrometer RS232 drop down, connection options and handshake output.

At the upper left and right within all pages, there is a method menu (top left) and an options menu (top right). The method menu contains the range of functions which can be used with the PMD and

electrometer, and the options menu contains configurable settings and a way of exiting the program. The bottom right of the program contains a coloured circle with the status of the program, it is red when busy and green when idle.

3.3.2 Settings

Due to the wide range of possible configurations for other PMDs and electrometers, and due to time constraints involved with this thesis, it was determined that a completely user-configurable settings menu should be created. This allows end users to configure TBIControl for their own devices by researching the documentation provided by their product manufacturers and entering the relevant information in the settings. Some information may be more trivial than others to obtain, the base commands for example should be in the default documentation of most manufacturers electrometers, and should be known to those who build a PMD. Commands such as the data index however may be a little more difficult to find, PTW had extensive documentation where they provided sample output of commands where the data index was readily determinable, however this will vary between manufacturers.

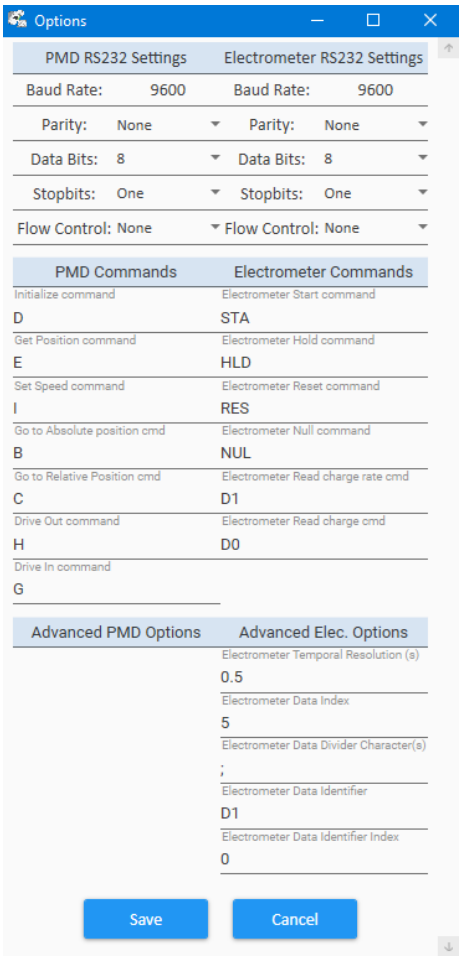

Figure 3.3: Image of TBIControl's user-configurable settings within the options menu.

Fig. 3.3 shows the various user-configurable settings for both the electrometer and PMD. Most settings have informative tool tips about what they are and where this information can be found for different devices. Once saved these settings are persistent for the program and are saved under "%AppData%/Local/TBIControl".

3.3.3 Move PMD

The Move PMD interface was developed for full control over the PMD. The speed and position of the PMD tray were configurable, along with being able to initialize the PMD to prepare it for use. The move mode could also be changed so that the tray could be moved to absolute discrete locations or in relative steps from its current location, it could also be sent out to its maximum extents in both directions.

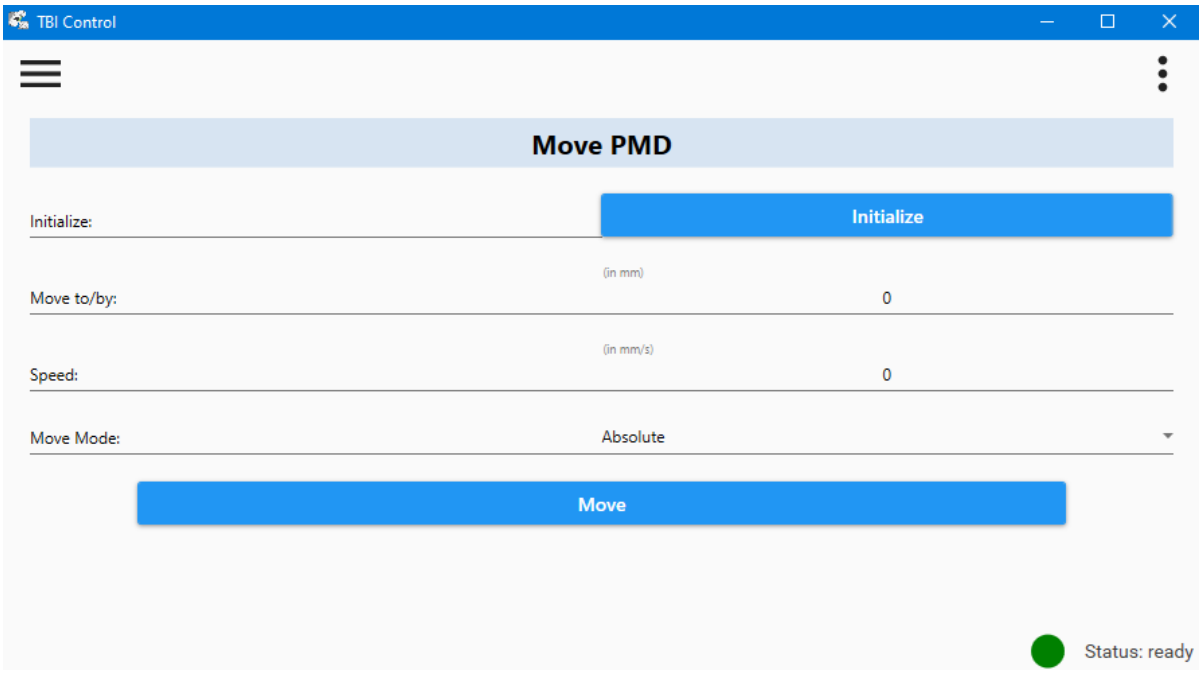

Figure 3.4: Image of TBIControl's Move PMD method.

The Move PMD interface is best illustrated by Fig. 3.4, where all user editable settings are shown.

3.3.4 Electrometer Read

Electrometer read was designed to read out charge rates from the electrometer over a set period of time. These charge rates were all output as text in comma separated values format in the "Charge Rate Output" text box. Once measurement had completed, the arithmetic mean, standard deviation, and standard error of the mean were all computed and provided in the respected text boxes shown in Fig. 3.5.

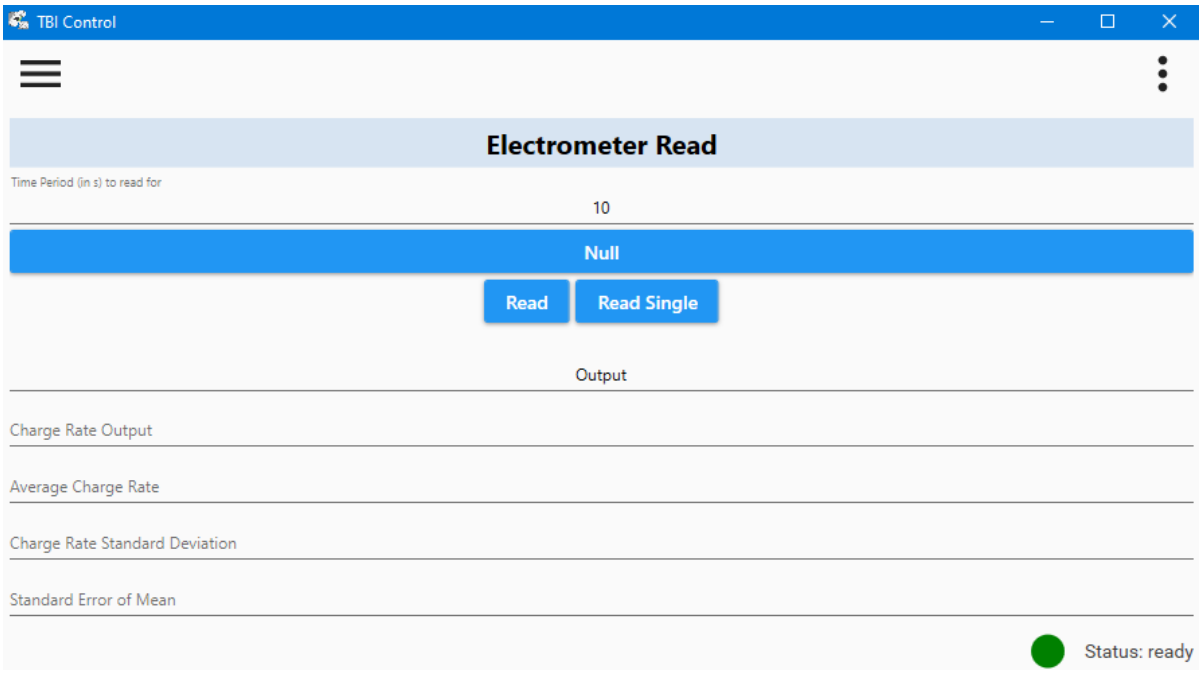

Figure 3.5: Image of TBIControl's Electrometer Read method.

The purpose of electrometer read was to test reading out the electrometer over long periods of time to ensure stability, and for measurement of charge rates at specific points over time which were useful in following sections.

3.3.5 Step and Record

Step and record mode was designed to semi-autonomously acquire profiles over a range of depths with an electrometer and PMD connected via RS232. A user would enter input parameters for measurement as shown by Fig. 3.6. Once entered and started with the solid water and chamber in position at the first depth, the PMD would record a profile step-wise. Multiple charge rates are recorded for each point off axis whenever either the electrometer buffer updated or 0.5 s elapsed since last measurement (whichever happened first). Charge rates are averaged, providing the mean charge rate, standard deviation, and experimental standard deviation (uncertainty of the mean) determined using methods discussed in Appendix B. Once the profile acquisition is complete for a given depth, it will ask whether the recording was "successful", selecting "no" will cause a repeat of this profile measurement. This was useful for preventing linac termination faults requiring segments of data to be remeasured after the set was complete. Finally at the end of all profile measurements over all depths the data is saved under "SRsave-DDMMYYYYHHMMSS" format. This data can be plotted on the spot using the plotting controls, or exported to a spreadsheet for external analysis.

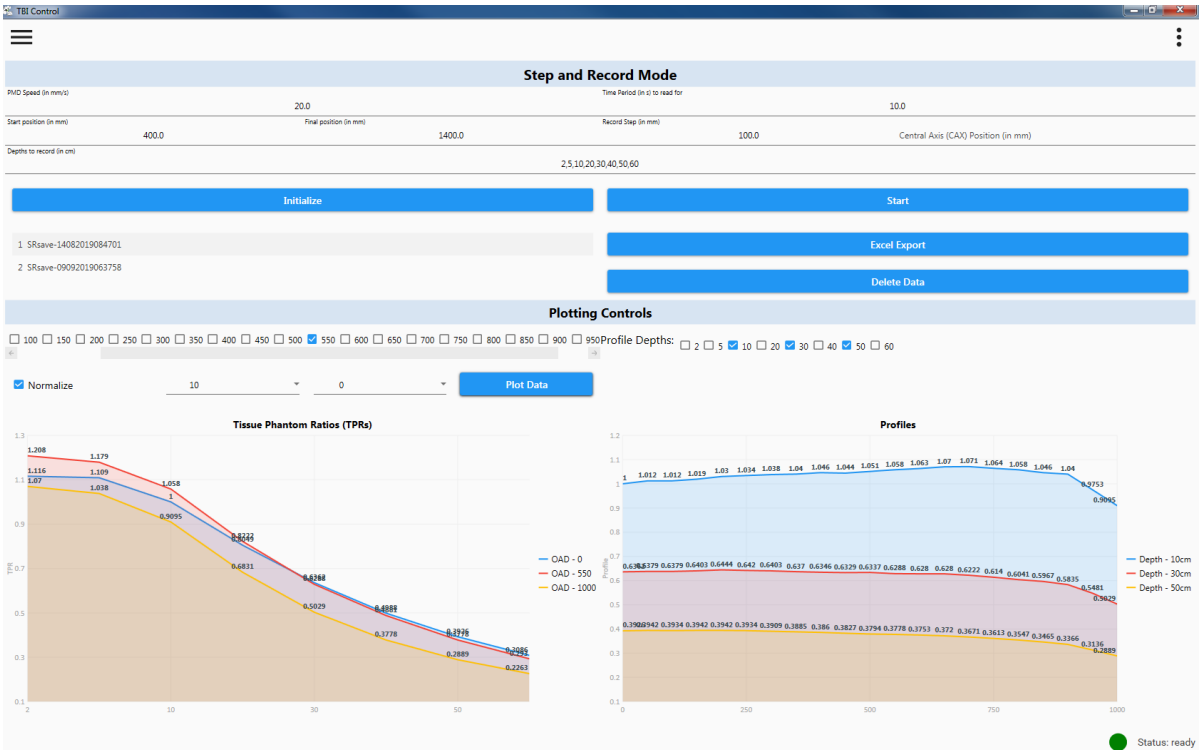

Figure 3.6: Image of TBIControl's Step and Record method.

Fig. 3.6 shows step and record mode with two sets of real data acquired, saved and plotted using the plotting controls.

Equipment Validation

Once the PMD had been built, it was necessary to validate the necessary dosimetry equipment along with the PMD itself so that any limitations of equipment used could be quantified. This was important for measurement using the PMD, and for the software design of TBIControl's methods as it allowed for appropriate use of the PMD when making dose profile measurements.

3.4.1 Electrometer

Quantifying the temporal resolution of the PTW Electrometer over RS232 was important, since we would be using it with the PMD for measurement of charge and charge rate. To quantify this, the electrometer's bias voltage was set to 0 V, and a 3 V_{pp}, 3.3 Hz signal was applied via a BNC to TNC connector from a Signal generator to our electrometer. This allowed the determination of the temporal resolution of our electrometer by continually reading out the charge and current via the RS232 interface with python at the highest possible baudrate (19200).

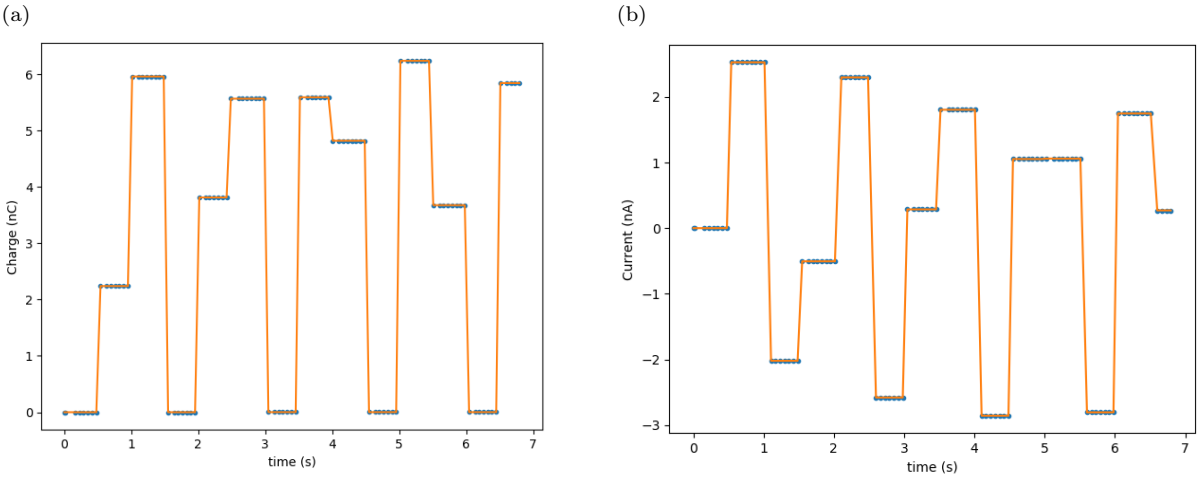

Figure 3.7: Temporal resolutions of both measured (a) charge and (b) current, using a signal generator and PTW Electrometer.

Fig. 3.7 shows that the temporal resolution of the electrometer when read-out is in-fact limited to 0.5 s (which is the update-time on the electrometer's display), this is demonstrated as even though there is a changing current/charge faster than the 0.5 s display update (3.3 Hz Square wave from signal generator), the multiple data points at each output have the exact same data value in the interval of t_0 and $t_0 + 0.5$ s.

3.4.2 PMD Speed and Positioning

The speed and positioning accuracy of the PMD were required to be validated immediately after it was built. Since the device was intended to measure profiles and TPRs, the speed and position were important quantities to measure such that the off-axis positional uncertainty of the farmer chamber could be realized.

A python script was created to characterise PMD motion in terms of speed by having the PMD traverse a set distance and recording the time it took to reach that point. The script would also sample the change in distance over smaller time steps to record a set of speeds. These speeds were analysed and initially it was found that as the speed increased, the actual speed became increasingly less than the reported speed. This data was collected and provided to Geoff and he was able to make the appropriate adjustments to the assembly code on the micro-controller such that the speed was then equal to the reported speed for all speeds tested.

Positioning accuracy was tested vigorously by moving the PMD to set points across the entire 1.8m track and verifying the position via measurement with a ruler with 1 mm divisions. Due to the limitations of time and the measurement device used, the PMD was only verified to a ± 1 mm position accuracy. These limitations could be overcome by using a vernier caliper for sub-millimeter precision.

Figure 3.8: PMD speed and positioning validation using a python script on a laptop (left) connected by RS232 to the PMD (right).

Validation setup of the PMD is shown in Fig. 3.8. Along with testing the positioning accuracy, positioning of the PMD over time was also tested. This was done using a python script to test the PMD in position step mode and continuously back and forth. Positions were again tested using a ruler for the PMD step mode and were validated to a ± 1 mm position accuracy over a 4 h continuous run time. For continuous mode, an audio sound was set up to play from the testing laptop at specific positions, this was then compared with a ruler placed at these positions. At high speeds continuous mode was very difficult to measure with high accuracy therefore for speeds $v > 10$ mm/s the positional accuracy could only be validated to ± 2 mm whereas for speeds $v < 10$ mm/s the positional accuracy could be validated to $\pm$ 1 mm. The measurement of continuous movement positioning could have been improved with the use of a laser at each validation point.

3.4.3 PMD Scatter Contribution

The PMD contained a number of metal components and additional material over the base TBI couch. In Sec. 2.1 we discussed different types of scatter and its contribution to dose. Therefore it was important to determine whether the additional material the PMD introduced would contribute any measurable scatter to the measurement point. If the scatter was measurably significant it could perturb measurements made using the device, therefore directly affecting results.

To evaluate this, charge rate was measured for various points along the PMD with a farmer chamber with a buildup cap (wall thicknesses of 2 mm 2.5 mm for energies 10 MV and 15 MV respectively)

suspended in-air using a retort stand. For each point along the PMD the couch was moved such that the chamber was kept at CAX such that measurements were directly comparable with no off-axis considerations required. A measurement was also taken on the base couch without the PMD such that the scatter could be characterised as a proportion of the primary beam output. Measurements were taken using TBIControl's electrometer read (Sec. 3.3.4) with 10 s of record time per step.

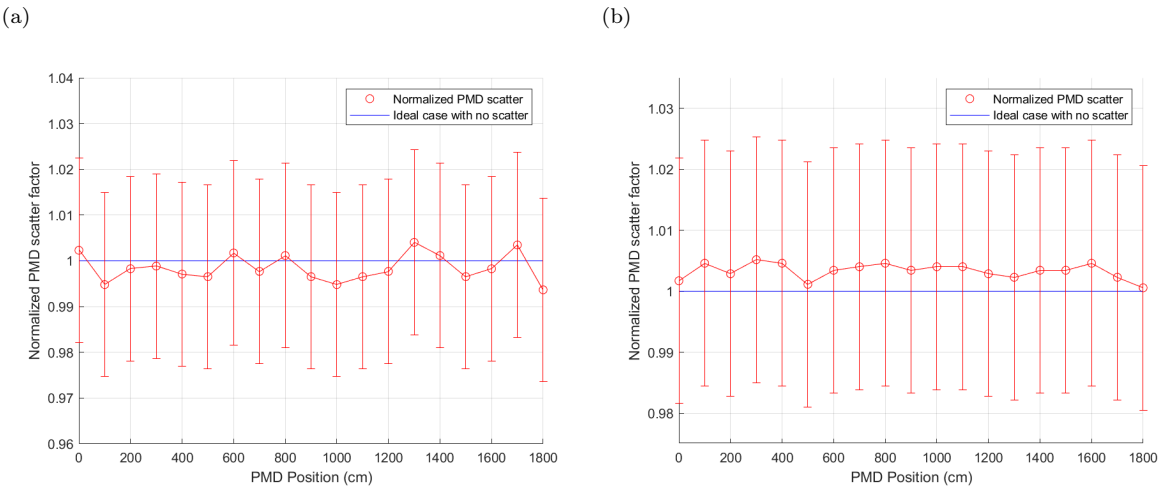

Figure 3.9: Normalized PMD scatter in (a) T1 treatment room and (b) T2 treatment room. In-air charge rate measured at various positions along the PMD normalized to the in-air charge rate on the bare couch without the PMD.

Fig. 3.9 shows our PMD scatter for various points along the PMD (red) with reference to an ideal case with no scatter (blue). All measurements in both T1 and T2 fluctuate about the ideal case given their uncertainty (95 % confidence interval) evaluated according to Appendix B. Intended measurements conducted with the PMD would use solid water, with the detector in all but one direction (the direction with the least amount of PMD material) being surrounded by $\approx$ 12 cm of attenuating solid water material. Given the scatter factors combined with uncertainties, along with the intention of use, it is reasonable to conclude that the PMD would contribute no measurable amount of scatter to measurements, given the uncertainties.

Implementation

Over the course of using the PMD several times for profile and TPR measurement, an optimal best practices document was created for implementation of the PMD for future measurements. The motivation behind the document was to promote consistency and understanding in measurement whilst allowing measurements to be performed as efficiently as possible. The document is now appended to the TBI protocol document, and is provided in Appendix A.

Chapter 4

Treatment Planning System Modelling at eSSD

This chapter discusses modelling of eSSD TBI dosimetry and treatment using Monaco and the existing spreadsheet described in Sec. 2.4.2. Firstly a block phantom was contoured in Monaco with modelled results acquired to determine whether the difference of agreement between modelled and measured results was clinically acceptable given measurement and model uncertainties (DD $< 6\,\%$). Once this was determined, anthropomorphic measurements were justified, so the RANDO (Alderson RANDO phantom, Radiology Support Devices Inc.[1]) phantom CT was used to model point doses for comparison to measured point doses. The modelled block phantom and anthropomorphic measurement sets along with spreadsheet determined midline and peak lung doses provide the basis for comparison to the measured sets to determine the possibility of clinical implementation. This chapter provides methods and results of phantoms modelled in Monaco along with the existing spreadsheet determined results of midline doses using the RANDO phantom. Firstly we will look at our block-phantom Monaco modelled results, followed by anthropomophic phantom Monaco results, finally we will provide the existing spreadsheet midline and peak lung doses given the RANDO phantom geometry and compare these with Monaco modelled midline and peak lung doses. This chapter sets up the basis for comparison of results in Ch. 6, along with providing a quantitative assessment of the existing spreadsheet relative to the Monaco model.

Block Phantom

Determination of profiles and TPRs in a block phantom using both the MC and CCC algorithms were initially undertaken to validate the feasibility of using Monaco for eSSD treatment planning. Results from each algorithm were compared with each other along with the determined uncertainties produced by Monaco. The intended end result was to compare these results with measured beam profiles and

TPRs in a block phantom composed of a combination of solid water and water to determine the difference of agreement between measured and modelled results, which is discussed in chapter 6.

4.1.1 Methods

In order to compare Monaco beam profiles and TPRs at various depths in a water phantom to those measured during commissioning and with the PMD, the following steps and procedures were undertaken.

1. Monaco required an external volume to prevent it from crashing and so that the dose algorithms would not have issues with isocentre "being outside a treatment/patient volume". Therefore producing a phantom using Elekta's DICOM creation tool CarpeDicom (Elekta AB, Stockholm, Sweden) with 1 cm divisions (smaller divisions caused Monaco to crash) of dimension 500 cm × 220 cm × 50 cm was done to fulfil this requirement.

2. Creating one external volume of smallest relative electron density to water (minimum allowed was 0.01) of dimension $(SMD - 100\,\text{cm}) \times 220\,\text{cm} \times 1\,\text{cm}$ $[x, y, z]$ which encapsulated our internal structure(s), this slice was placed at the edge of the empty phantom so as to be within the phantom but as far away as possible from the internal structures (at position $y = 109.5\,\text{cm}$) and the beam. This external volume is best illustrated by Fig. 4.1.

3. Added an interest point which the beam could use as isocentre, close to the edge of the external volume, this interest point would vary in x and y positions in order to adjust for off-axis distances and TPR depths (such that the beam moved closer at deeper depths to maintain 432.6 cm source to point distance (SPD) for a point at the measurement depth).

4. Creating the water phantom, due to the 1 cm divisions in Carpedicom the phantom had to be created between $z = 15.5\,\text{cm}$ and $z = -14.5\,\text{cm}$, therefore in order to ensure correct centering, the isocentre interest point needed to be shifted to 0.5 cm, along with the other interest points for OOAR measurements.

5. Added multiple interest points at x-positions (for different depths in the phantom) to compare with commissioning depth data. Depths used were 2 cm, 5 cm, 10 cm, 20 cm, 30 cm, 40 cm, 50 cm, and 60 cm.

6. Adjusted prescription to a fixed 2000 MU in order to maintain a constant output for all depths and off axis distances (OADs), and to reduce impact of noise from small statistical fluctuations.

7. Set beam parameters to the usual TBI treatment conditions with gantry angle 90°, 45° collimator angle and 40 cm × 40 cm field size set at the isocentre interest point.

8. Varied the off-axis distance by moving the isocentre interest point by 10 cm in the y-direction and in various distances (2 cm, 5 cm, 10 cm, 20 cm, 30 cm, 40 cm, 50 cm, and 60 cm) in the x-direction to record the depth-dose at each off-axis distance to determine TPR.

9. Determined the OOARs for each point using the reference depth at 10 cm and 0 cm off-axis using Eq. 2.16.

10. From these OOARs, graphing TPRs and profiles for each OAD and depth respectively was done to compare with our commissioning data.

11. Four different phantoms were created for measurements for the varying depths (30 cm × 30 cm × 30 cm, 40 cm × 30 cm × 30 cm, 50 cm × 30 cm × 30 cm, and 60 cm × 30 cm × 30 cm) to ensure that a direct comparison between Monaco data and the commissioning results could be made since during commissioning additional build up material was added on at each measurement point, rather than having a 60 cm × 30 cm × 30 cm phantom and varying the measurement points.

12. For depths 40 cm, 50 cm, and 60 cm, an additional 5 cm × 28 cm × 30 cm structure of 0.01 relative electron density to water was created to reduce the point dose uncertainty in Monaco. Without this object, sometimes the marker at this maximum depth or measurement point in Monaco would be at the boundary between the block phantom and air, causing larger than expected uncertainties by an order of magnitude at this point. These uncertainty reducing objects did not change the mean or total dose to the point. This object is shown in Fig. 4.1 as the green object.

13. Calculation variables used were a 0.5 cm grid spacing, for MC a 1.00 % statistical uncertainty per calculation was used with 2500 MU for additional constrained uncertainty. Anything finer than the 0.5 cm grid spacing would cause Monaco to crash.

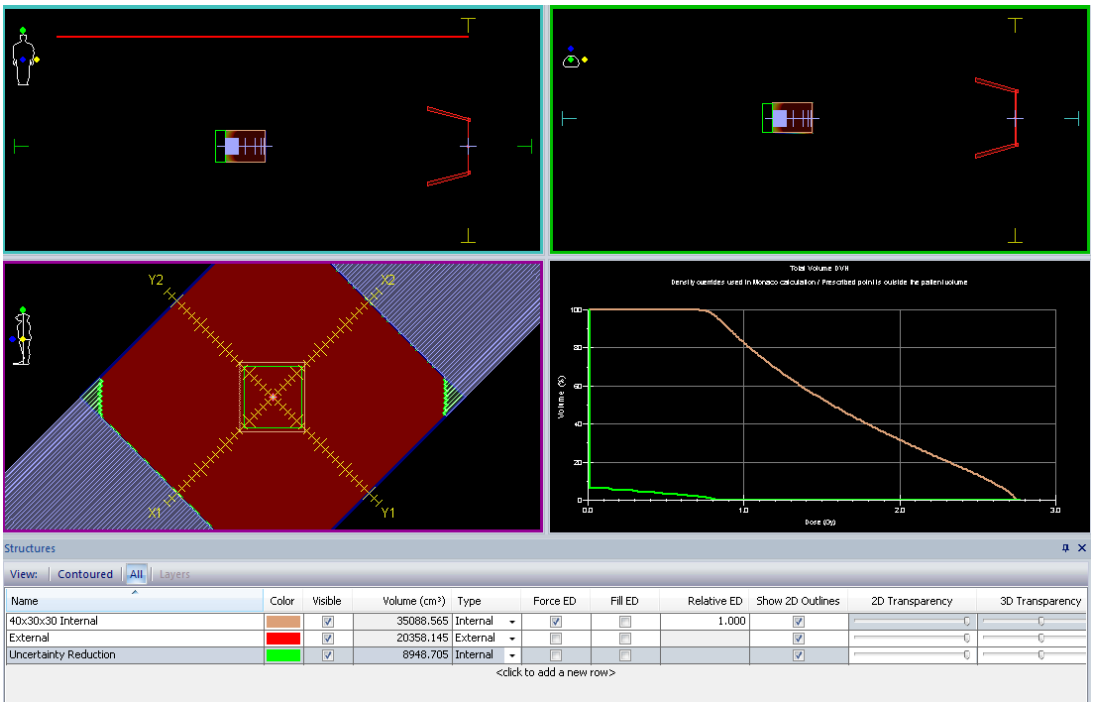

Figure 4.1: Monaco Phantom Setup example with 40 cm × 30 cm × 30 cm phantom illustrating the set up of the beam, external volumes, block phantom, and uncertainty reducing object.

Fig. 4.1 illustrates the phantom set up in Monaco using the 40 cm × 30 cm × 30 cm as the example as this shows the point-dose uncertainty reducing structure (green contour) explained in 12. The external volume created in step (2) did not contribute any difference to the point doses, this was verified by moving these volumes such that they were directly next to the phantom (positions $z = 15.5$ cm and $z = -14.5$ cm which made no difference to the point doses. It was also tested via comparing point doses with two planes at positions $y = 109.5$ cm and $y = -109.5$ cm with a beam at 100 cm SSD, to with no planes at 100 cm SSD. The point doses in this case were also identical.

4.1.2 Results

4.1.2.1 MC Model

Modelled dose data using the MC model described in the methods above was tabulated and OOARs from Eq. 2.16 determined. These OOARs were plotted as a function of off-axis distance and depth so that the profiles and TPRs could be evaluated qualitatively.

(a) (b)

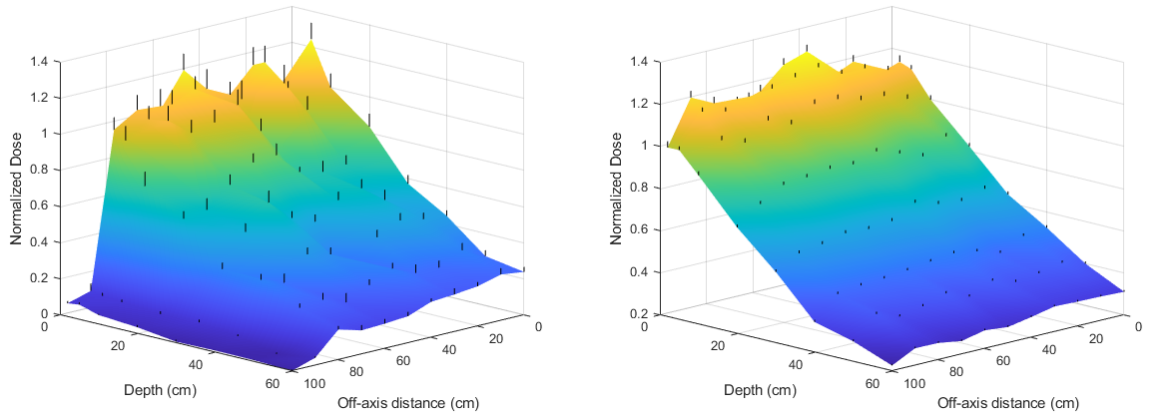

Figure 4.2: Dose from Monaco's MC model normalized to the output point for various OADs and depths, plotted against OAD and depth for (a) T1 treatment room and (b) T2 treatment room. Profiles and TPRs are shown by these 3D plots with uncertainty bars with a 95 % confidence interval plotted for each measured point in black.

Fig. 4.2 shows qualitatively, Monaco's MC model poorly represents a dose profile and TPR for all depths and OADs. For both T1 and T2 the MC model appears noisy, with T1 having significantly large error bars relative to the normalized dose.

4.1.2.2 CCC Model

Modelled dose data using the CCC model described in the methods above were tabulated and OOARs from Eq. 2.16 determined. These OOARs were plotted as a function of off-axis distance and depth so that the profiles and TPRs could be evaluated qualitatively.

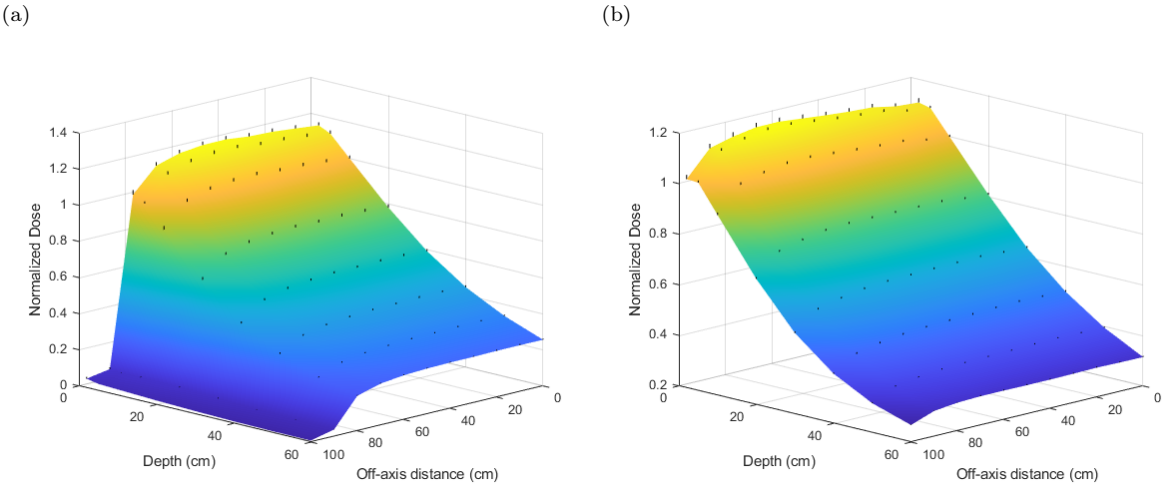

Figure 4.3: Dose from Monaco's CCC model normalized to the output point for various OADs and depths, plotted against OAD and depth for (a) T1 treatment room and (b) T2 treatment room. Profiles and TPRs are shown by these 3D plots with uncertainty bars with a 95 % confidence interval plotted for each measured point in black.

Fig. 4.3 shows qualitatively, Monaco's CCC model represents a reasonably accurate dose profile and TPR for all depths and OADs. Unlike with the MC model, the CCC model has smooth profiles and TPRs, which is what we would qualitatively expect for a homogeneous block phantom.

4.1.3 Discussion

An attempt to model wall backscatter in Monaco was also done for both T1 and T2 geometries. Unfortunately due to the large size of the surrounding walls at these extended SSDs these attempts would cause Monaco to reach maximum memory and CPU utilization and persistently crash after a long (20 min) computation time. Therefore given the memory (32 gb available) and processor constraints available, the wall could not be modelled in Monaco with either T1 or T2 geometries. Wall scatter contribution was however measured empirically as shown and discussed in Sec. 5.3.

Anthropomorphic Phantom

Validation of the Monaco model in an anthropomorphic phantom was crucial for determining whether Monaco could be implemented as a TPS for TBI treatments. The best available heterogeneous phantom at Christchurch Hospital is the RANDO phantom (Fig. 4.4), which includes appropriate density materials for lungs, bone and other tissues to provide a model which was as close as possible to a human patient. A CT of this phantom was readily available for importing into Monaco to calculate doses for comparison to measured data and existing spreadsheet calculated midline doses.

Figure 4.4: Stock photo of the Alderson RANDO phantom.[1]

This section will discuss the methods of modelling the RANDO phantom at eSSD in Monaco, along with obtained results in preparation for comparison to measured data in Ch. 6 and a discussion about TPS limitations. In addition, spreadsheet calculated midline doses will also be compared with Monaco results to see how well Monaco compares with existing treatment planning. Since it was previously determined by the block-phantom geometry that the MC algorithm was noisy and poorly represented profiles and TPRs, the MC algorithm was not evaluated for the RANDO phantom and only the CCC algorithm will be used for determination of dose in the RANDO phantom.

4.2.1 Methods

To compare point doses in Monaco to those determined from film, diode, and farmer chamber measurements (discussed in Sec. 5.5), and those calculated with the spreadsheet, the following steps and procedures were taken.

1. A CT of RANDO was imported into Monaco.

2. An external volume of smallest relative electron density to water (0.01) with dimension $(SMD - 100\,\text{cm}) \times 60\,\text{cm} \times 1\,\text{cm}$ $[x, y, z]$ was created, which encapsulated our internal structures. This slice was was placed as far away (in the z-direction) as possible from both the internal structures and the beam. This external volume allowed for the extending of the allowed SSD in Monaco without perturbing the dose delivered. Fig 4.5 best illustrates the complete setup of structures.

3. Two spoilers of thickness 2 cm were created with internal separation of 43.7 cm and external separation of 47.5 cm with the spoiler on the left side of RANDO being right up against RANDO's shoulder so that modelled results represented measurement setup. These two spoilers had electron densities of 0.993 and 0.992 for T1 and T2 respectively as discussed in Sec. 2.4.

4. Ricebags were modelled by creating a volume extending from the most superficial point of the phantom through to the most inferior, and the most anterior through posterior. The lateral bounds of the volume were 1.5 cm space between the volume and the spoilers on either side, this was to account for an estimated 1.5 cm of ricebag packing inefficiency being air-gaps within and between the ricebags. The ricebags were set to electron densities of 0.891 and 0.880 for T1 and T2 respectively as discussed in Sec. 2.4.

5. Multiple points of interest were placed at 2.5 cm depth divisions between several key slices in RANDO for comparison to film measurement. Key slices were the head (slice 3-4), neck (slice 9-10), chest (slice 17-18), umbilicus (slice 30-31) and groin (slice 34-35).

6. Points of interest were also placed at the entrance and exits of the head (slice 2), neck (slice 9), chest (slice 15), umbilicus (slice 27), and groin (slice 35) slices for comparison to diode measurements. These exact points of measurement were along the approximate middle (AP) of RANDO. Of note are that these differ from those used for the film comparison, so results may vary slightly.

7. Additionally points of interest were also placed at the half-way point between interest points used for diode comparisons, these would represent the midline doses for comparison to the spreadsheet and the farmer chamber measurement (taken at the groin).

8. Two beams on either side of RANDO were created, both had 45° collimator angles and their gantry angles were 90° and 270° for the right and left fields respectively.

9. Only the CCC calculation algorithm was evaluated here as it was found the MC model was too noisy for clinical viability. The CCC variables used were a 0.5 cm grid spacing, 1500 MU for T1 comparison and 2400 MU for T2 comparison.

10. The left and right fields were computed individually, with the results averaged.

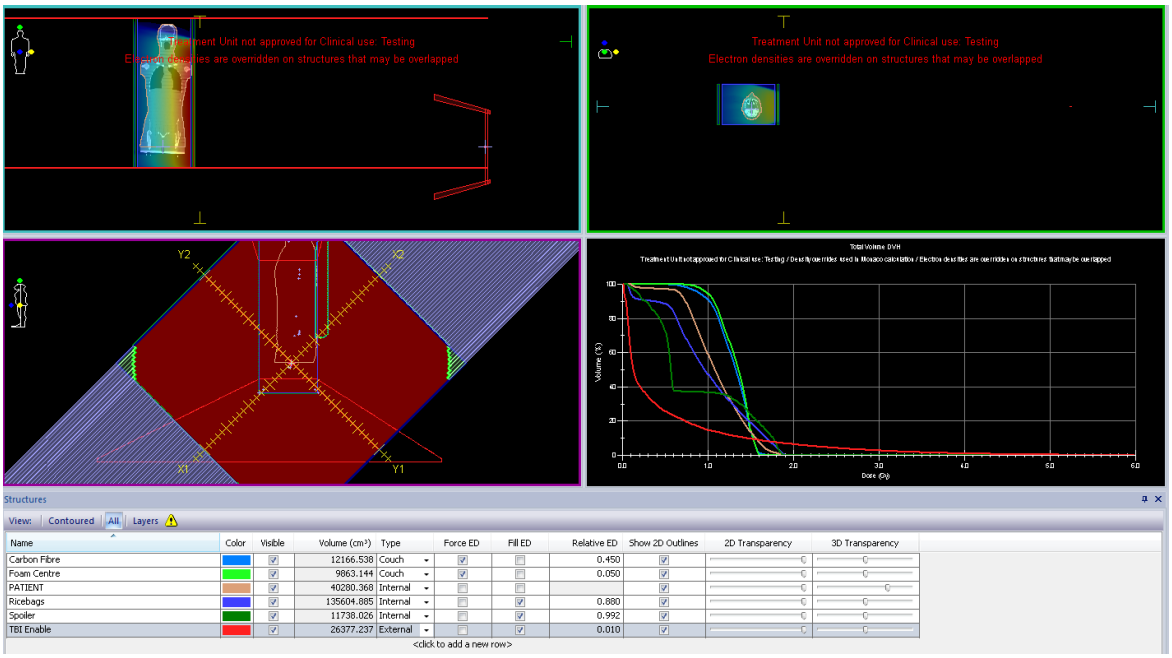

Figure 4.5: Monaco Anthropomorphic phantom setup demonstrating structures discussed in method points 1-4.

The complete setup of the RANDO phantom in Monaco is best illustrated by Fig. 4.5. The spoilers, ricebags, and external contour (TBIEnable) are all shown, along with a T2 beam geometry to the left side of RANDO.

4.2.2 Results

4.2.2.1 Film Comparison

Doses were determined for various depths in RANDO using methods above. These doses were to be compared with measured film data to evaluate the CCC model in a heterogeneous phantom. Only a left beam was used for the dose calculation as this was mirrored by measurement only being made using the left field.

Fig. 4.6 illustrates our depth doses in Monaco for various slices in RANDO in both T1 and T2. Qualitatively the depth dose curve looks as we would expect for homogeneous media, however for heterogeneous media these depth dose curves seem to be overly simplistic.

(a) (b)

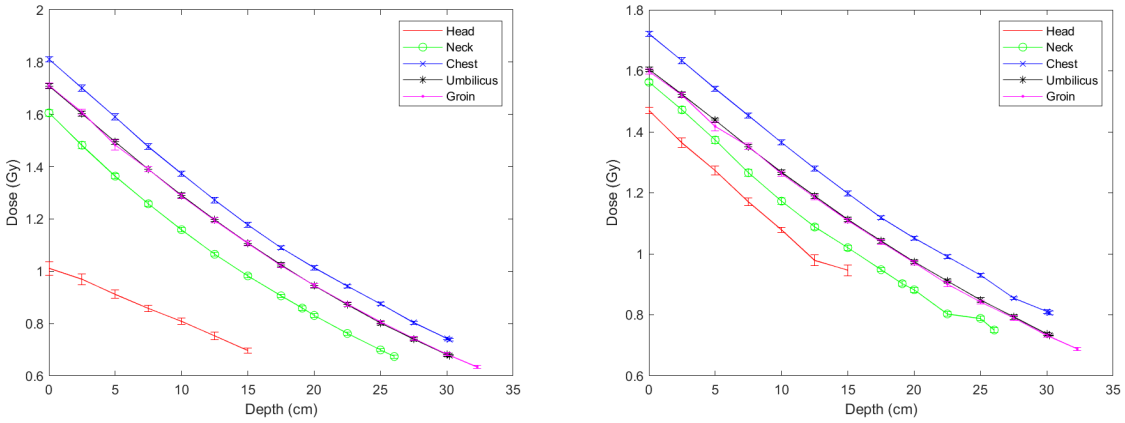

Figure 4.6: Monaco determined depth dose distributions with various slices in RANDO for (a) T1 treatment room and (b) T2 treatment room.

4.2.2.2 Diode Comparison

To compare our Monaco model to diode measured results in Ch. 5 and Ch. 6, we needed to determine dose at the corresponding points where diodes would be placed. These points were placed as discussed in the methods, and doses for both T1 and T2 models were computed for both left and right beams, 1500 MU and 2400 MU were used for T1 and T2 respectively as these approximately gave 1 Gy dose to the midline. These monitor units would also be delivered for the corresponding measured dose for direct comparison between the model and measurement later in Ch. 6.

	Region				
Depth (cm)	Head	Neck	Chest	Umbilicus	Groin
Left ENT	0.412	1.275	1.847	1.717	1.715
Left EXIT	0.576	1.015	0.715	0.674	0.594
Right ENT	0.570	1.138	1.713	1.718	1.764
Right EXT	0.547	0.900	0.648	0.673	0.625
Average ENT	0.491	1.207	1.780	1.718	1.740
Average EXIT	0.562	0.958	0.682	0.674	0.610

Table 4.1: T1 Table of Monaco entrance (ENT) and exit (EXIT) doses (in Gy) for various points where diodes were placed.

	Region				
Depth (cm)	Head	Neck	Chest	Umbilicus	Groin
Left ENT	1.456	1.387	1.749	1.621	1.591
Left EXIT	0.962	1.109	0.788	0.736	0.657
Right ENT	1.253	1.267	1.636	1.613	1.648
Right EXT	0.819	0.996	0.722	0.726	0.681
Average ENT	1.355	1.327	1.693	1.617	1.620
Average EXIT	0.8905	1.053	0.755	0.731	0.669

Table 4.2: T2 Table of Monaco entrance (ENT) and exit (EXIT) doses (in Gy) for various points where diodes were placed.

Tables 4.1 and 4.2 give the Monaco simulated doses at the entrance and exit points of the head, neck, chest, umbilicus and groin regions (exact slices of points provided in methods). An average of the left and right fields are also computed for comparison to measurement.

4.2.2.3 Midline and Peak Lung Doses

To compare Monaco with existing spreadsheet calculations and the groin farmer chamber measurements, midline doses were also computed for points along the midline which corresponded to points sampled in the spreadsheet. Doses along the midline were computed for the head, neck, chest, umbilicus and groin. Interest points were placed directly between the entrance and exit points placed for the diodes comparison. Additionally the peak lung doses were determined using an interest point at the closest point in the lungs to the beam.

	Region				
Depth (cm)	Head	Neck	Chest	Umbilicus	Groin
Left Field	0.660	1.138	1.181	1.097	1.045
Right Field	0.569	1.013	1.081	1.099	1.083
Average	0.615	1.076	1.131	1.098	1.064

Table 4.3: T1 Monaco Midline doses (in Gy) for various regions determined for both left and right fields and averaged.

	Region				
Depth (cm)	Head	Neck	Chest	Umbilicus	Groin
Left Field	1.192	1.221	1.205	1.111	1.060
Right Field	1.021	1.102	1.106	1.105	1.086
Average	1.107	1.162	1.156	1.108	1.073

Table 4.4: T2 Monaco Midline doses (in Gy) for various regions determined for both left and right fields and averaged.

Midline doses in Monaco for T1 and T2 are shown in Tables 4.3 and 4.4 respectively. Doses are determined for both the left and right fields and averaged to determine the average midline dose determined in Monaco. The peak lung was determined by combining the average entrance and exit doses from Sec. 4.2.2.2 and then dividing by two (as treatment is bilateral). For T1 and T2 peak lung doses were determined to be 1.231 Gy and 1.224 Gy respectively.

4.2.2.4 Spreadsheet Dose Comparison

Dose differences were calculated using Eq. 2.17, where D_1 were the spreadsheet midline doses and D_2 were the average of the left and right field Monaco midline doses from Tables 4.3 and 4.4.

	Region				
Depth (cm)	Head	Neck	Chest	Umbilicus	Groin
T1 Midline Dose (Gy)	0.961	1.077	1.179	1.090	1.070
T2 Midline Dose (Gy)	1.103	1.114	1.168	1.083	1.078
T1 DD (%)	36.004 %	0.093 %	4.071 %	-0.729 %	0.561 %
T2 DD (%)	-0.361 %	-4.131 %	1.027 %	-2.256 %	0.464 %

Table 4.5: Spreadsheet calculated midline doses for T1 and T2, along with dose differences between spreadsheet calculated midline doses and averaged left and right field Monaco determined midline doses

The spreadsheet calculated peak lung doses for T1 and T2 were 1.200 Gy and 1.170 Gy respectively. Therefore T1 and T2 have respective peak lung dose DDs between the spreadsheet and Monaco of 2.518 % and 4.412 %. It is shown by Table 4.5 that T2 has a clinically acceptable agreement between spreadsheet calculated and Monaco determined doses. For T1 the only region where we see disagreement is the head, this is most likely due to the head region being in the beam's peripheral steep dose gradient region (penumbra). The head region for T1 being in the penumbra is not as significant as other doses due

to the greater variation of dose in the penumbral region. In most cases Monaco seems to overestimate the dose to the midline relative to the spreadsheet, there are only three points where Monaco predicted midline doses are less than the spreadsheet: the groin region for both T1 and T2, and the chest region for T2. Nevertheless with the exception of the T1 head dose, the predicted midline doses and peak lung doses are all within clinically acceptable agreement between spreadsheet calculated and Monaco determined doses. Verifying by comparison to actual measurements covered in the next chapter are necessary so that appropriate conclusions can be drawn in Ch. 6.

Chapter 5

Linac Measurements

This chapter provides introductions, methods, and results for measurements made with the linacs in TBI conditions. First we look at quantifying the monitor unit drifting of the linac, followed by determining the field symmetry and impact of wall scatter. Dose profiles and TPRs are then determined from measurements in a block-phantom, and finally point doses in an anthropomorphic phantom are measured. The results from this chapter are then subsequently used in Ch. 6 for comparison to the TPS model.

Monitor Unit Drifting and Fluctuation

During testing of the PMD, it was discovered that there was considerable drifting of the dose rate (MU/min) on both T1 and T2 treatment machines over a time span of several minutes up to a steady state where small fluctuations (± 1 MU) were observed. Since charge rate was the quantity measured when using the PMD, to fully understand the uncertainty of future measurements, it was necessary to quantify the dose rate drifting both in terms of the time to reach a steady state dose rate $t_{\dot{D}_{SS}}$ along with the steady state variation $\sigma_{\dot{D}_{SS}}$. The steady state variation is then expressed as the relative uncertainty (u_r) calculated using Eq. 5.1 below derived from Appendix B.

$$u_r = \frac{\sigma_{\dot{D}_{SS}}}{\mu_{\dot{D}_{SS}}} \tag{5.1}$$

Since many of the measurements using the PMD were done by measuring dose rate, it is important to have quantified the uncertainty resulting from the fluctuation from the linac, as well as knowing the appropriate time to begin measurement for each linac.

Measurement of monitor unit fluctuation in both T1 and T2 was done using an NE2571 farmer chamber with an appropriate brass buildup cap for each energy (2 mm and 2.5 mm wall thickness for 10 MV and 15 MV respectively), held in-air using a metal retort stand. The chamber was then attached via triaxial cable to the PTW electrometer and the electrometer then plugged in to a laptop via RS232 to USB. Charge rate was then continuously readout via TBIControl's electrometer read discussed in

Sec. 3.3.4. Resulting data was then analysed using Matlab to determine $t_{\dot{D}_{SS}}$, $\sigma_{\dot{D}_{SS}}$, $\mu_{\dot{D}_{SS}}$ and calculate u_r.

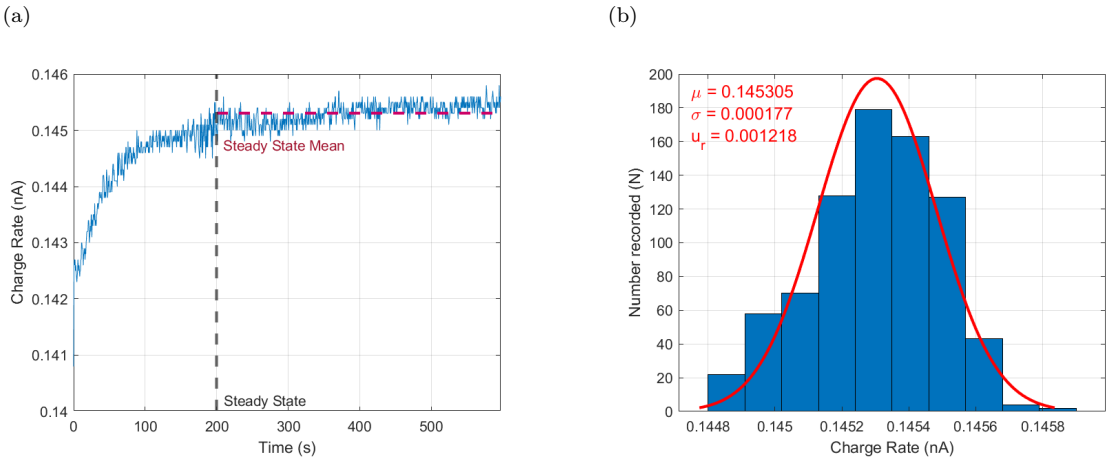

Figure 5.1: T1 graphs of (a) monitor unit drift and fluctuation displaying points of determined steady state and mean, and (b) monitor unit fluctuation histogram for $t > t_{\dot{D}_{SS}}$ showing a Gaussian distribution and fit with fitted quantities $\sigma_{\dot{D}_{SS}}$, $\mu_{\dot{D}_{SS}}$, and CV.

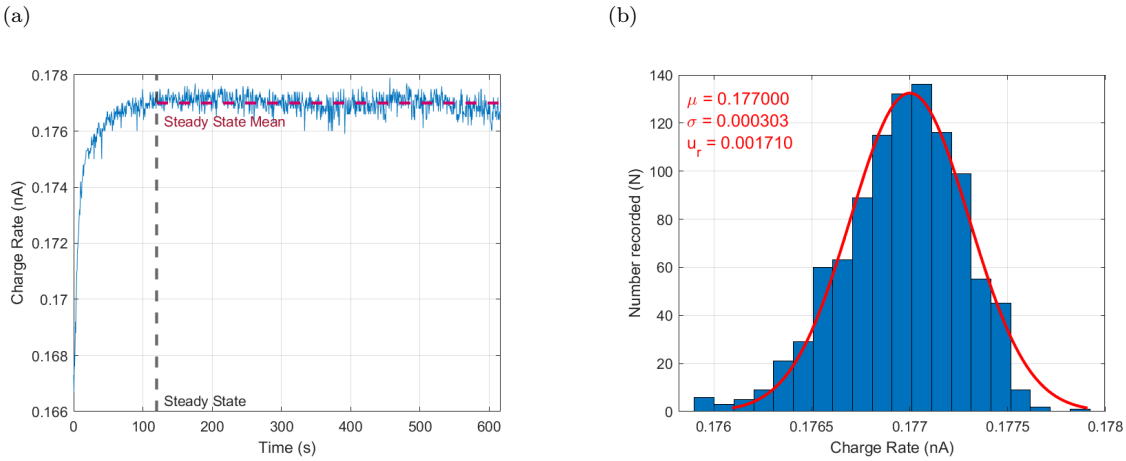

Figure 5.2: T2 graphs of (a) monitor unit drift and fluctuation displaying points of determined steady state and mean, and (b) monitor unit fluctuation histogram for $t > t_{\dot{D}_{SS}}$ showing a Gaussian distribution and fit with fitted quantities $\sigma_{\dot{D}_{SS}}$, $\mu_{\dot{D}_{SS}}$, and CV.

Fig. 5.1 and Fig. 5.2 show the approximate $t_{\dot{D}_{SS}}$ is 200 s for T1 and 120 s for T2. The mean, standard deviation and coefficient of variations are also displayed on the respective histograms which show the Gaussian distribution of charge rate data. The relative uncertainty of charge rate at steady-state was considered the population type A uncertainty (uncertainty types and their combination are discussed in

Appendix B) of measured charge rate when using the PMD. This was therefore used as the total type A uncertainty for measurement of charge rate as it provided the spread of values around the maximum for the approximate population of measured charge rates.

Symmetry

One of the key assumptions made when making measurements using the PMD is that our radiation beam is symmetrical. IEC 60976 provides a standard called the point difference quotient (PDQ) which is a measure of beam symmetry. The PDQ is given by Eq. 5.2, this PDQ has been modified from the standard equation by subtracting 100, this is done to "zero" our difference quotient percentage at 0 %.

$$PDQ = 100 \times \max\left(\frac{D_{left}}{D_{right}}, \frac{D_{right}}{D_{left}}\right) - 100 \tag{5.2}$$

Beam symmetry data was measured at 2.5 cm and 3 cm depths in a 30 cm × 30 cm × 30 cm solid water block phantom for T1 and T2 respectively. The respective depths were selected for two reasons. Firstly they were the z_{max} depths for T1 and T2, therefore TCPE existed. Secondly the minimum possible depth was chosen where TCPE existed such that flattening of the beam from interactions with the phantom was minimal. The measurements were taken in 2 cm divisions off axis with 10 s measurement time using TBIControl's step and record mode (Sec. 3.3.5).

Two analyses were performed with respect to symmetry data: the zeroed point difference quotient given by Eq. 5.2, and the symmetry given by simply the left half of the field subtracted from the right half given by Eq. 5.3 below. Eq. 5.2 gives us the overall symmetry of our field, whilst Eq. 5.3 gives us information about the differences in dose with respect to the field side.

$$PD_{(R-L)} = 100 \times \frac{D_{right} - D_{left}}{D_{right}} \tag{5.3}$$

The field symmetries of T1 and T2 are plotted in Fig. 5.3 and Fig. 5.4 respectively. From the plotted symmetries it is shown that within the clinically useful field sizes, T1 and T2 have a maximum asymmetries of (2 ± 1) % and (2 ± 1) % (with 95 % confidence intervals) respectively. AAPM Task Group 40 (TG-40) [47] and the updated Task Group 142 (TG-142) [48] reports on quality assurance provide a 3 % tolerance for beam symmetry.

The dose symmetry of a field is affected by many factors, including small beam steering deviations onto the flattening filter, and small variations in collimator jaw positions to name a couple. These variations usually cause beam hardening or softening to one half of the beam, therefore resulting in superficial dose asymmetries between the two halves of the beam. At greater depths, these asymmetries become less significant [49] as lower energy components of the beam deposit dose superficially.

The measurement of symmetry was taken at the shallowest possible depths where TCPE existed for T1 and T2. At greater depths the beam would become more symmetric. Our measurements show given the uncertainty, that over the clinically useful field size the beam symmetries of T1 and T2 are both

within tolerance and therefore we can assume beam symmetry. This provides a justification for why profiles will only required to be measured for one half the clinically useful field shown later in Sec. 5.4.

(a)

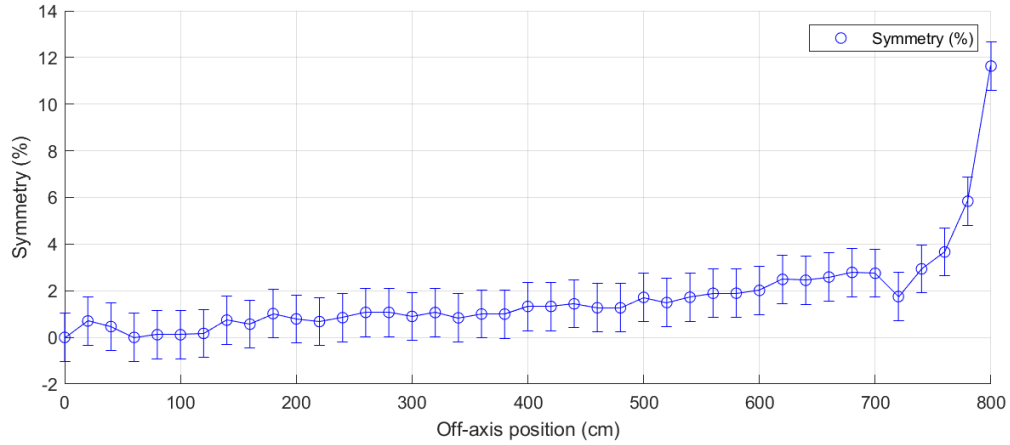

(b)

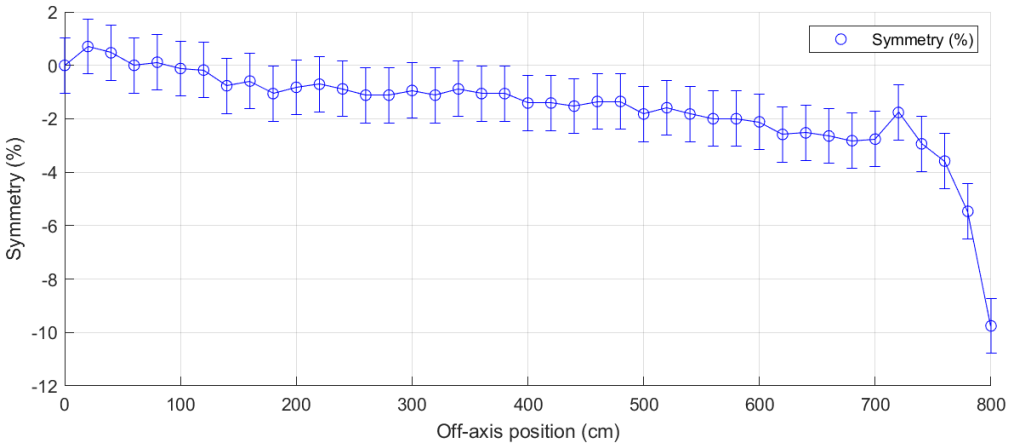

Figure 5.3: Profile symmetry graphs determined using data measured on T1 calculated using two different methods. (a) The zeroed IEC 60976 standard given by Eq. 5.2. (b) The symmetry from the right half of the field minus the left half normalized to the right half of the field.

(a)

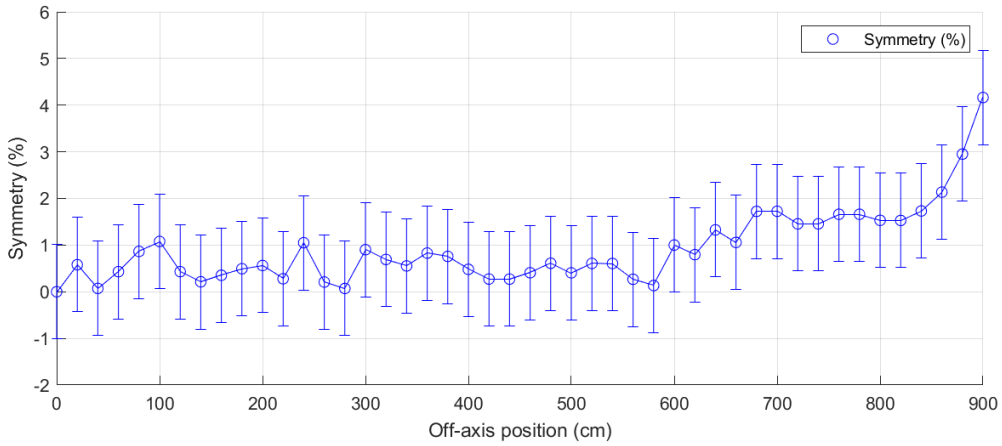

(b)

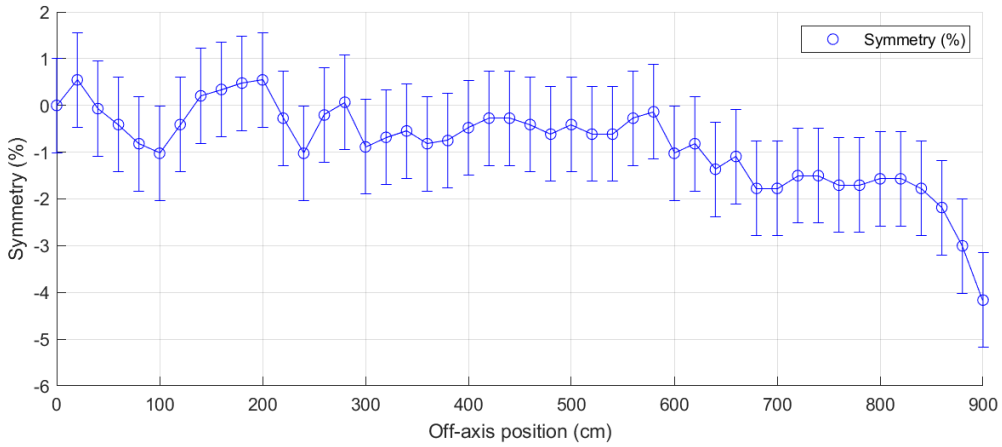

Figure 5.4: Profile symmetry graphs determined using data measured on T2 calculated using two different methods. (a) The zeroed IEC 60976 standard given by Eq. 5.2. (b) The symmetry from the right half of the field minus the left half normalized to the right half of the field.

Wall Scatter

Backscattered radiation from the reinforced concrete wall behind the couch in the beam-line was important to quantify. Since the Monaco TPS model could not incorporate wall scatter as discussed in Sec. 4.1.3, it was necessary to determine the impact backscatter has on the measurement of profiles and TPRs in order to determine whether the lack of modelling this in Monaco would be a significant impediment to achieving an accurate beam model.

Radiation backscatter was measured in-air using a farmer chamber with an appropriate build up cap at various distances from the wall to the SMD and off-axis distances. For each measurement point, two quantities were measured: the dose rate with no shielding $\dot{D}_{SS}$ (dose rate of source + scatter), and the

dose rate with 58.4 cm of lead shielding blocking the chamber from the primary beam, $\dot{D}_S$ (dose rate of wall scatter). The lead shielding had dimensions of 58.4 cm × 10 cm × 5 cm, made up of the smallest sized blocks available so that the field projected on the wall was perturbed as little as possible. For off-axis distances the effective displacement of the front lead block (the angle which the lead had to be at relative to the chamber) was determined using Eq. 5.4.

$$\Delta X_{max} = \frac{OAD}{SCD} \times L_{lead} \tag{5.4}$$

Where OAD is the off-axis distance, SCD is the source-chamber distance, L_{lead} being the length of lead 58.4 cm used, and ΔX_{max} is the maximum horizontal displacement of the lead, at distance L_{lead} from the chamber. Fig. 5.5 best illustrates how this effective displacement was used to align the lead blocks to appropriately shield the farmer chamber when making measurements off-axis.

(a) (b)

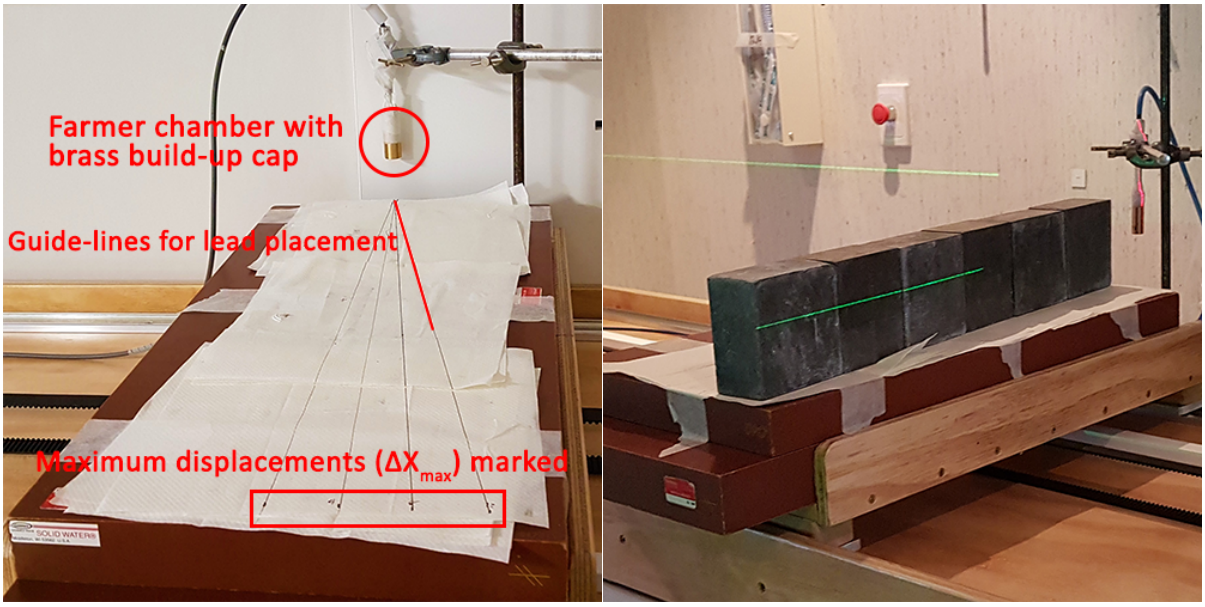

Figure 5.5: Experimental set up of wall scatter measurements. (a) Shows the chamber set up with the retort stand, maximum displacement markings and guide lines for the placement of lead bricks in-front of the chamber. (b) An example measurement of wall scatter with the lead bricks placed along the guide lines.

To determine the relative (%) wall scatter S_{wall} at each point the wall scatter dose rate needed to be normalized to the dose rate of the source. Since the measurement without lead was of the combined source and wall scatter, the wall scatter needed to be subtracted from this such that the wall scatter could be normalized to the source only and thus would not be an underestimate of the wall scatter. Relative wall scatter was determined using Eq. 5.5

$$S_{wall} = \frac{\dot{D}_S}{\dot{D}_{SS} - \dot{D}_S} \tag{5.5}$$

Where shielded and non-shielded dose rates were calculated using Eq. 2.12.

	SCD at isocenter (cm)					
OAD (cm)	341	348	358	368	378	388
0	3.2 ± 0.1	3.3 ± 0.1	3.5 ± 0.1	3.7 ± 0.1	3.9 ± 0.1	4.0 ± 0.1
25	2.2 ± 0.1	2.3 ± 0.1	2.7 ± 0.1	3.0 ± 0.1	3.1 ± 0.1	3.5 ± 0.1
50	2.5 ± 0.1	2.6 ± 0.1	2.8 ± 0.1	3.0 ± 0.1	3.3 ± 0.1	3.9 ± 0.1
75	1.8 ± 0.1	1.9 ± 0.1	2.3 ± 0.1	2.6 ± 0.1	3.1 ± 0.1	3.6 ± 0.1

Table 5.1: Relative wall scatter (%) for T1 at various different source-chamber and off-axis distances.

	SCD at isocenter (cm)				
OAD (cm)	432.6	437.1	447.1	457.1	467.1
0	3.3 ± 0.1	1.0 ± 0.1	1.6 ± 0.1	1.8 ± 0.1	1.8 ± 0.1
25	2.3 ± 0.1	0.9 ± 0.1	1.5 ± 0.1	1.7 ± 0.1	1.9 ± 0.1
50	2.6 ± 0.1	0.8 ± 0.1	1.5 ± 0.1	1.8 ± 0.1	1.7 ± 0.1
75	1.9 ± 0.1	0.8 ± 0.1	1.6 ± 0.1	2.4 ± 0.1	2.0 ± 0.1

Table 5.2: Relative wall scatter (%) for T2 at various different source-chamber and off-axis distances.

It was important to also determine the approximate energy range of the backscattered photons from the wall. A simple Matlab model of wall backscatter from Compton scattered photons was created using Eq. 2.3 to determine the maximum energy of scattered photons we could expect for various measurement points along the SMD.

The energy of Compton scattered photons are only considered here as other processes or scattering events which could contribute dose to a point at depth in a phantom were assumed to be negligible. Rayleigh, Delbrück, Thompson scattering are negligible in the MeV energy range for large angles $\theta > 40°$ when compared with Compton scattering by differential cross section.[23] Processes which produce charged particles like pair production, photoelectric absorption were also assumed negligible. Since the depth being considered was 10 cm deep in the phantom (from the wall's perspective), when taking into account the range of electrons and positrons, the fact that the rate of energy loss of electrons in high energy therapeutic electron beams is approximately 2 MeV/cm,[22] and the scatter in air between the wall and the solid water phantom, most if not all electrons would contribute no dose to depths $z \leq 20$ cm in the phantom. Dose resulting from the production of photoneutrons in the wall material was also

assumed negligible as would only make up a small percentage of an already small percentage, discussed in Sec. 2.1.1.1. Finally from the arguments discussed, the assumption that only the energy of Compton scattered photons need to be considered when determining whether depths $z \leq 20\,\text{cm}$ in our phantom need to be corrected for wall scatter is reasonable to make.

Fig. 5.6 and Fig. 5.7 show for a chamber at SMD, the energy of backscattered photons in both treatment rooms is in the range of 0.25 MeV to 0.36 MeV. When taking into consideration the air scatter between the wall and the phantom, and attenuation of photons with respect to depth in a phantom, it is reasonable to assume that wall scatter contributions for depths (measured from the linac side of the phantom) less than or equal to 20 cm will be negligible. Therefore scattering results will only be applied for the depths 30 cm and greater, and will not need to be applied for comparison to anthropomorphic phantoms due to rice bag packing and the beam spoilers.

This measurement of wall scatter is important for the comparison of results between Monaco calculated and linac measured dose profiles in block phantoms. As discussed in Sec. 4.1.3, memory and processing limitations meant that the wall could not be modelled in Monaco. Therefore measuring the relative wall scatter provides a factor for which Monaco doses can be corrected to provide a more accurate comparison with measurement later in Ch. 6.

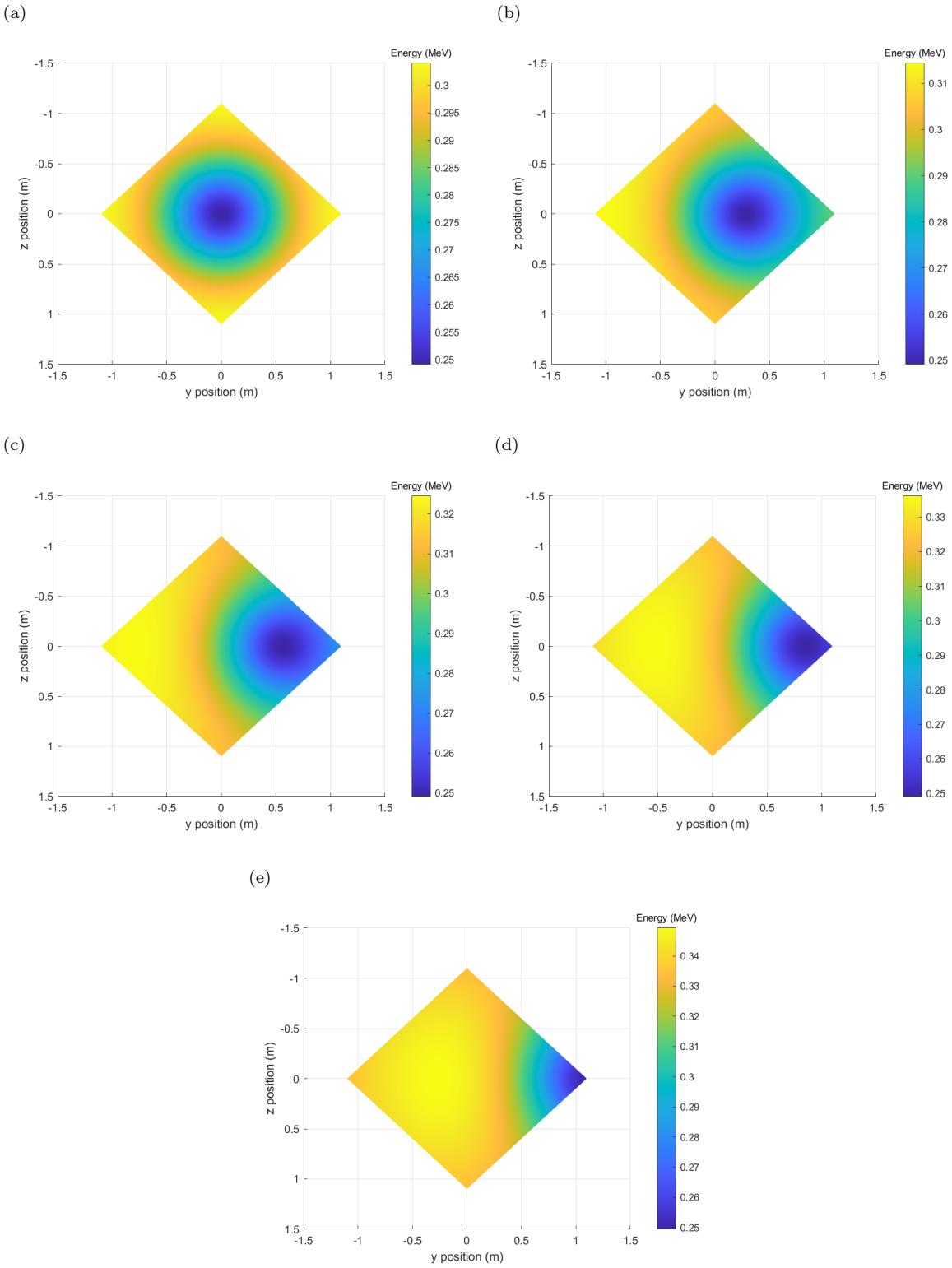

Figure 5.6: T1 Photon energy from points along the wall in the radiation field projected onto the wall as received by the detector at SMD. (a) With detector at CAX position. (b) Detector at 25 cm off-axis. (c) Detector 50 cm off-axis. (d) Detector 75 cm off-axis. (e) Detector 100 cm off-axis. This model is symmetrical on both axes.

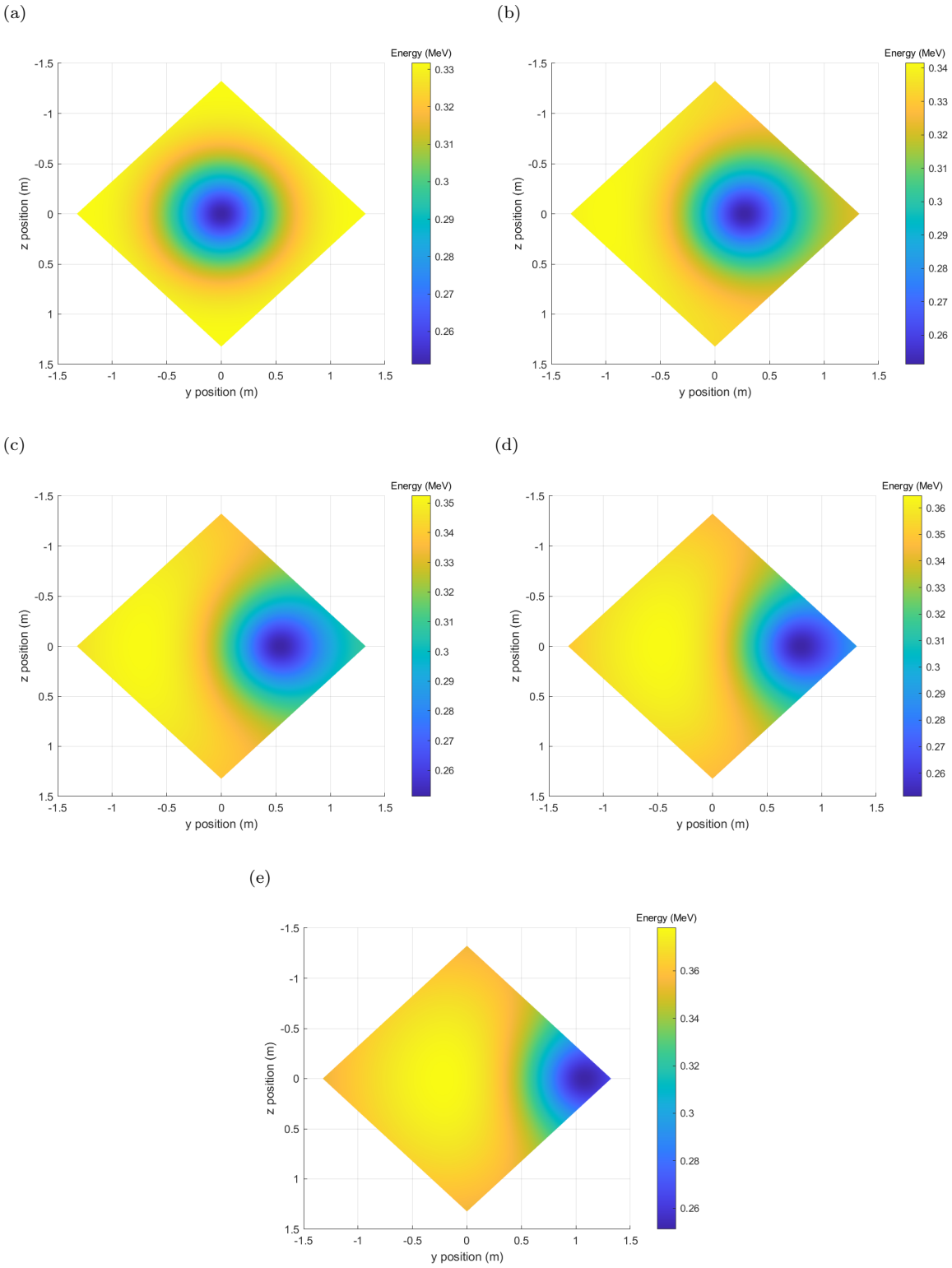

Figure 5.7: T2 Photon energy from points along the wall in the radiation field projected onto the wall as received by the detector at SMD. (a) With detector at CAX position. (b) Detector at 25 cm off-axis. (c) Detector 50 cm off-axis. (d) Detector 75 cm off-axis. (e) Detector 100 cm off-axis. This model is symmetrical on both axes.

Profiles and TPRs in a Block Phantom

5.4.1 Previous Commissioning Measurements

Data from previous (latest) commissioning measurements were used as a reference to see how the PMD could improve upon measurement methodology. Previous commissioning measurements were conducted using a 28.4 cm × 30 cm × 30 cm PTW T41023 water phantom[44] with 0.6 cm thick of fitted red wax and 1 cm of blue solid water to fill in the small gap in the exterior of the tank and build up to 30 cm × 30 cm × 30 cm total volume.[50,51] For depths $z > 30$ cm additional blue solid water was used to build up the depth. A NE2571 farmer chamber was placed in a holder within the tank and moved when necessary to measure doses at depth and off-axis. When performing measurements off-axis and for some depths the entire water tank and solid water ensemble had to be physically moved, this was not only a time consuming endeavor per-measurement, but also contributed a significant (±1 cm with 95 % confidence interval) amount of uncertainty with respect to chamber position.

(a) (b)

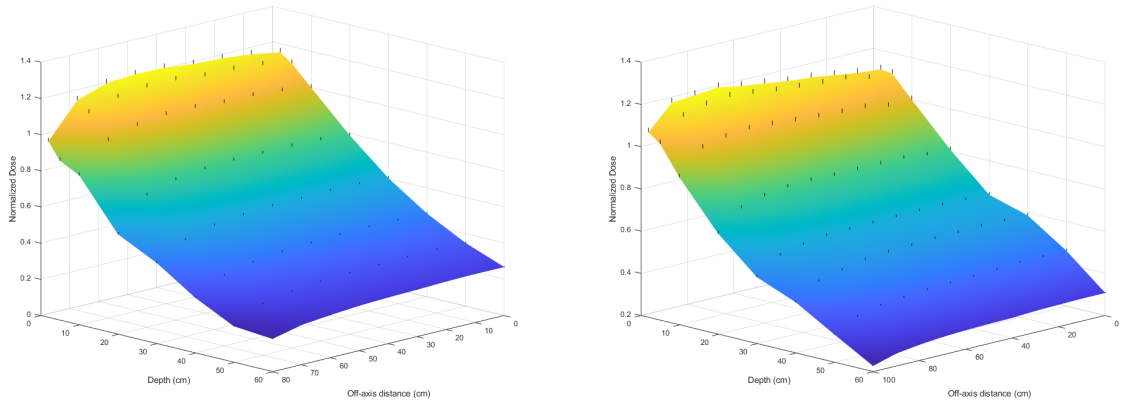

Figure 5.8: Dose normalized from previous commissioning data to the output point for various OADs and depths, plotted against OAD and depth for (a) T1 treatment room and (b) T2 treatment room. Profiles and TPRs are shown by these 3D plots with uncertainty bars (95 % confidence interval) plotted for each measured point in black.

Fig. 5.8 shows the previous commissioning results for T1 and T2. T1's TPRs and profiles qualitatively look as we would expect until we get to 70 cm off-axis where we see the TPR becomes quite noisy and appears jagged instead of a smooth depth dose we would expect. T2 by contrast was markedly inconsistent with what a normal TPR should look like throughout all off-axis distances. If profile is looked at alone, T2 would seem to be normal, however when we plot both together we see that at depths 40 cm and 50 cm the dose begins to level off, rather than smoothly decreasing as expected. This presented

an immediate challenge when looked at, and was resolved by repeating measurements for depths 40 cm and 50 cm using identical apparatus under conditions described above. It was found that the previous commissioning data was about 14 % greater than the newly acquired data.

5.4.2 Measurements Using the PMD

Measurements of profiles and TPRs in T1 and T2 used the PMD in step and record mode (discussed in Sec. 3.3.5) with a 10 s record time for each point off-axis. The ambient temperature and pressure inside T1 and T2 were also recorded at the start and end of profile acquisitions. Variations in temperature and pressure were found to be less than 0.2 °C and 0.5 hPa respectively for all profile measurements in T1 and T2.

Absorbed dose to water is determined using TRS-398's Eq. 2.12 as discussed in Sec. 2.1.4.1. The final quantity to be determined is the OOAR given by 2.16, substituting the Eq. 2.12 into Eq. 2.16 yields Eq. 5.6.

$$OOAR(h\nu, A, z, x) = \frac{\cancel{N_{D,w,Q_0}} \times M_Q(z,x) \times \cancel{k_{Q,Q_0}} \times k_{TP}(z,x) \times \cancel{k_s} \times \cancel{k_{pol}}}{\cancel{N_{D,w,Q_0}} \times M_Q(10\,\text{cm}, 0\,\text{cm}) \times \cancel{k_{Q,Q_0}} \times k_{TP}(10\,\text{cm}, 0\,\text{cm}) \times \cancel{k_s} \times \cancel{k_{pol}}} \tag{5.6}$$

Since N_{D,w,Q_0}, k_{Q,Q_0}, k_{pol} and k_s are identical for the output point and points off-axis these terms cancel. Given the maximum variations in temperature and pressure during measurement, using Eq. 2.13 the maximum change in k_{TP} would be approximately 0.03 % given T and P are of the order of T_0 and P_0 respectively. Therefore due to Δk_{TP} being insignificant, along with the fact that the ratio of charge is interchangeable with the ratio of charge rate, we can finally simplify our calculation of OOAR to Eq. 5.7.

$$OOAR(h\nu, A, z, x) = \frac{\dot{Q}(z,x)}{\dot{Q}(10\,\text{cm}, 0\,\text{cm})} \tag{5.7}$$

Where $\dot{Q}(z,x)$ is the charge rate at depth z and off-axis distance x, and $\dot{Q}(10\,\text{cm}, 0\,\text{cm})$ is the charge rate at the output point, $z = 10\,\text{cm}$ and $x = 0\,\text{cm}$.

Fig. 5.9 shows both our measured profiles and TPRs for both T1 and T2 treatment rooms. The uncertainty of these profiles and TPRs are determined by combining the type A relative uncertainty of dose rate fluctuation (discussed in Sec. 5.1), and relative type B estimated uncertainty associated with geometrical setup uncertainties, equipment variation and small changes in ambient conditions. These uncertainties are then combined using Eq. B.5.

(a) (b)

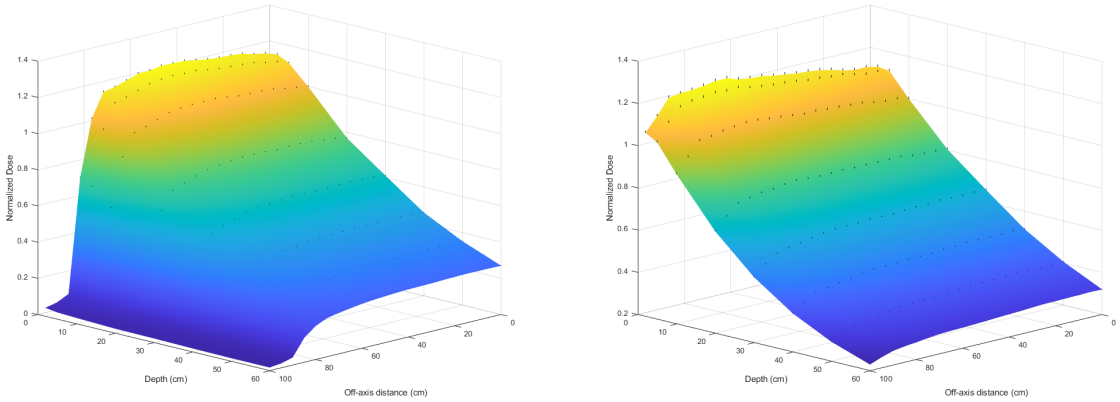

Figure 5.9: Charge rates from PMD measurement normalized to the output point for various OADs and depths, plotted against OAD and depth for (a) T1 treatment room and (b) T2 treatment room. Profiles and TPRs are shown by these 3d plots with uncertainty bars (95 % confidence interval) plotted for each measured point in black.

5.4.3 DD Comparison

To compare our sets of PMD measured profiles and TPRs to the previous commissioning set, DD analysis was performed. The DD for T1 and T2 was determined using Eq. 2.17 with the previous commissioning OOARs being subtracted from the PMD measured OOARs.

	OAD (cm)								
Depth (cm)	0	10	20	30	40	50	60	70	80
2	-1.44 %	-1.06 %	-0.27 %	-0.25 %	0.07 %	0.22 %	0.19 %	1.10 %	5.54 %
5	-0.25 %	-0.15 %	0.51 %	0.86 %	1.23 %	1.46 %	1.93 %	2.26 %	10.62 %
10	0.00 %	-0.12 %	0.50 %	0.74 %	1.05 %	1.04 %	1.67 %	1.73 %	3.79 %
20	-2.42 %	-1.78 %	-0.91 %	-1.04 %	-0.32 %	-0.05 %	0.37 %	0.79 %	10.31 %
30	-1.77 %	-0.56 %	-0.32 %	-0.01 %	0.27 %	0.62 %	0.45 %	1.42 %	0.01 %
40	-3.27 %	-1.25 %	-1.38 %	-1.05 %	-0.50 %	-0.18 %	0.58 %	0.77 %	4.34 %
50	-2.07 %	-1.16 %	-0.31 %	-0.05 %	0.70 %	0.66 %	0.68 %	2.81 %	15.92 %
60	-2.57 %	-1.66 %	-0.55 %	0.16 %	0.66 %	0.74 %	1.91 %	1.27 %	1.02 %

Table 5.3: T1 DD between OOARs calculated from measured data using the PMD and previous commissioning OOARs.

Table 5.3 shows a reasonable DD between previous and current measurement, most DDs within our clinically useful field size are $< 3\%$ with the exception of one point with a DD of $-3.27\,\%$ which is acceptable.

	OAD (cm)										
Depth (cm)	0	10	20	30	40	50	60	70	80	90	100
2	0.72 %	0.85 %	1.80 %	2.02 %	2.28 %	2.48 %	2.19 %	1.99 %	1.70 %	1.58 %	-0.65 %
5	0.76 %	1.39 %	1.33 %	1.74 %	1.80 %	1.93 %	1.91 %	1.77 %	2.58 %	3.39 %	0.28 %
10	0.00 %	1.81 %	1.50 %	1.91 %	2.11 %	1.91 %	2.12 %	2.31 %	2.31 %	2.92 %	1.26 %
20	-0.26 %	0.23 %	0.07 %	0.41 %	0.54 %	0.64 %	0.79 %	0.96 %	1.32 %	2.24 %	0.90 %
30	-0.44 %	-0.33 %	0.38 %	-0.10 %	-0.69 %	-0.51 %	-0.95 %	-1.39 %	-1.77 %	-1.26 %	-2.35 %
40	-14.74 %	-14.04 %	-14.05 %	-13.88 %	-14.86 %	-14.40 %	-14.66 %	-14.47 %	-13.87 %	-13.36 %	-14.34 %
50	-15.02 %	-14.47 %	-14.11 %	-13.70 %	-13.64 %	-13.96 %	-13.92 %	-14.23 %	-14.52 %	-13.91 %	-13.25 %
60	0.53 %	1.06 %	1.44 %	1.63 %	1.74 %	0.50 %	-0.16 %	0.78 %	0.26 %	1.28 %	-0.73 %

Table 5.4: T2 DD between OOARs calculated from measured data using the PMD and previous commissioning OOARs.

Table 5.4 shows that with an exception of measurements at depths 40 cm and 50 cm, we have a reasonable DD between previous and current measurement, with only one point where the DD is $-3.39\,\%$ which is acceptable. We have discussed that the previously measured data had doses approximately 14% larger than a newly acquired data set under identical conditions. DDs for 40 cm and 50 cm seem to confirm these approximate overdoses from the previous commissioning data set. It is unclear what may have caused these overdoses in previous measurement, whether it be positioning error, large changes in ambient conditions, or equipment setup over the long time (approximately 12 h) these measurements took. Confidence in the fact that previous measurements were in-fact overdoses came from carefully (over several hours) remeasuring a couple of doses along the central axis using the same equipment (water tank setup), where results were less than 1 % different from those measured using the PMD. Additionally a few sets of measurements using the PMD were carried out over a few months where differences in results between them were less than 2 %. It is clear that the speed at which the PMD can carry out commissioning measurements and the improved chamber positioning accuracy provide a huge benefit, both in time saving and accuracy for conducting profile and TPR commissioning measurements with block phantoms.

Point Doses in an Anthropomorphic Phantom

Point doses were measured both with film and diodes using the RANDO phantom. In each measurement case, two spoilers were used, and rice bags were packed around RANDO as tightly as possible stacked up to the height of the spoilers with 20 cm of rice bags extending from the most superior and inferior points of RANDO to be as close to a typical clinical set up as possible. This section will discuss the two different measurement types explored, along with their individual methods, results and discussion.

5.5.1 Film Measurements

Immediately prior to measurement within RANDO, a set of calibration measurements were taken so that the RGB colour of the film could be calibrated against dose delivered. Eleven $4\,\text{cm} \times 4\,\text{cm}$ squares of

film were cut out and marked with a number at the upper left corner for orientation and dose delivered. Four cross hairs were also marked at the edges of the film for alignment of the film to the linac's cross hairs. Each piece of film was placed beneath 10 cm of blue solid water at isocenter (100 cm SAD with a 10 cm × 10 cm fieldsize), and were irradiated from 50 MU to 500 MU in 50 MU steps for films 1 to 10 respectively, the zeroth piece of film was not irradiated. The numbered orientation and delivered dose labelling of the calibration film along with cut direction is best shown by Fig. 5.10a. A farmer chamber measurement was also taken at 10 cm deep in blue solid water at isocenter under identical conditions such that the MU could be converted to Gy therefore allowing for a calibration curve of RGB values of film versus dose to be determined.

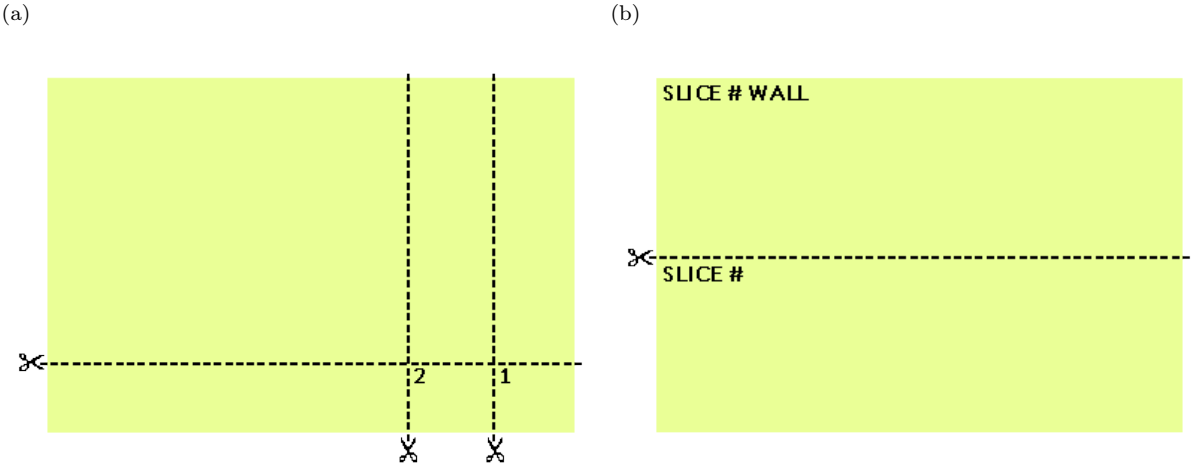

Figure 5.10: Film cut methodology with consistent orientation using labels and numbering at the upper left hand corner of each film. (a) Shows the numeric labelling of calibration film where numbers corresponded to the increments in dose, (b) shows the labelling of the measurement film which labelled the slice number and direction the wall was facing for the film closest to the wall.

For measurement within RANDO, each piece of film was cut into different equally sized strips with their orientation marked, and slotted into various transverse slices in RANDO. The orientation direction was identical to the calibration film. The orientation was marked with the slice number in the upper left corner, along with wall being labelled on the film which would be closest to the wall, this is best illustrated by Fig. 5.10b. Five different slices were used for representation: 3-4 (head), 9-10 (neck), 17-18 (mid chest), 30-31 (umbilicus), 34-35 (groin). Due to the transverse width of RANDO, two different film slices were required for all but the head and neck measurement region so that a PDD could be determined through RANDO, these two films were taped together and did not overlap. When the films were slotted into place, the entrance and exit points of RANDO were drawn using a marker on all films.

Due to timing constraints and to keep everything consistent between TPS modelling and measurement, only a single left field was used. 1500 MU was delivered for T1 and 2400 MU was delivered for

T2.

(a) (b)

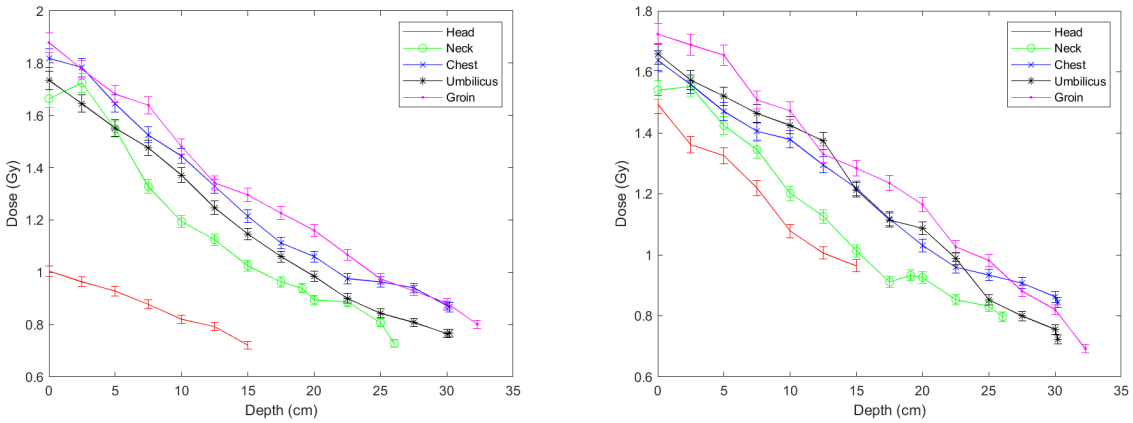

Figure 5.11: Film measured depth doses in RANDO in (a) T1 treatment room and (b) T2 treatment room.

Films were analysed using FilmQA Pro (Ashland LLC), using triple channel correction with the blue channel correcting for film density variation. The resulting depth doses are shown by Fig. 5.11. Qualitatively these depth doses appear noisy, though this could simply be a consequence of inhomogeneities in RANDO.

5.5.2 Diode Measurements

A set of diode measurements were also taken to compare in-vivo dosimetry commonly measured during patient treatment to Monaco results. Diodes were placed in accordance to local practice in-vivo positions Sec. 2.4.4 with the single groin diode replaced with an entrance and exit groin diode and the exclusion of the thighs, calves and ankles as these were not part of the RANDO phantom. Since diodes representing the exit doses were facing away from the beam, a diode orientation factor (DOF) had to be determined so that exit doses could be corrected to truly reflect dose to the point. This orientation factor was measured using 5 different diodes between slices 20-21 at the exit of the phantom, diodes were placed orientated toward the beam with dose measured and then flipped to face away from the beam at the same point with dose measured. The orientation factor was then calculated by averaging the ratios of dose toward the beam and dose away from the beam.

$$DOF_{T1} = 1.20 \pm 0.02,$$

$$DOF_{T2} = 1.16 \pm 0.02.$$

The diode orientation factor was measured at the exit of RANDO under full scatter conditions with

ricebag packing and spoilers so that a true representation of exit dose scaling could be attained which would take into account beam hardening and scatter.

	Region				
Field + Diode	Head	Neck	Chest	Umbilicus	Groin
Left ENT	0.630	1.297	1.834	1.698	1.668
Left EXIT	0.564	0.931	0.828	0.655	0.670
Right ENT	0.377	1.190	1.667	1.584	1.814
Right EXT	0.539	1.027	0.721	0.668	0.709
Average ENT	0.504	1.244	1.751	1.641	1.741
Average EXIT	0.551	0.979	0.775	0.662	0.689

Table 5.5: T1 exit-corrected diode measurements of dose (Gy) with TBI setup using the RANDO phantom, with the left and right fields averaged. ENT and EXIT are abbreviations for the entrance and exit respectively where the entrance is the closest diode to the beam at the entrace of RANDO and exit is the diode on the contralateral side.

	Region				
Field + Diode	Head	Neck	Chest	Umbilicus	Groin
Left ENT	1.340	1.382	1.828	1.639	1.680
Left EXIT	0.824	1.040	0.905	0.700	0.736
Right ENT	1.482	1.431	1.689	1.588	1.618
Right EXT	0.906	1.099	0.848	0.750	0.732
Average ENT	1.411	1.407	1.759	1.614	1.649
Average EXIT	0.865	1.070	0.876	0.725	0.734

Table 5.6: T2 exit-corrected measurements of dose (Gy) with TBI setup using the RANDO phantom, with the left and right fields averaged. ENT and EXIT are abbreviations for the entrance and exit respectively where the entrance is the closest diode to the beam at the entrace of RANDO and exit is the diode on the contralateral side.

Tables 5.5 and 5.6 show the left and right field entrance and exit doses on RANDO along with the

left and right field entrance and exit doses averaged for T1 and T2 respectively. Uncertainties for these doses are ±2 % (95 % confidence interval) given by the calibration tolerances and having made repeated measurements to confirm. The approximate peak lung dose with bilateral fields can be calculated by the sum of the average entrance and exit doses divided by two. For T1 and T2 the approximate peak lung doses are 1.253 Gy and 1.318 Gy respectively. These results are useful for making comparisons to Monaco modelled entrance and exit doses (from Sec. 4.2.2.2) later in Ch. 6.

5.5.3 Farmer Chamber Measurements

A farmer chamber was placed along the midline in the groin region taped in-place directly between RANDO's thighs. The total charge was measured three times for both the left and right fields and averaged, temperature and pressure were also measured for calculation of k_{TP}. Absorbed dose to water was then calculated using Eq. 2.12. The results for these measurements are:

$$D_w(T1) = (1.04 \pm 0.02)\,\text{Gy},$$
$$D_w(T2) = (1.07 \pm 0.02)\,\text{Gy}.$$

$D_w(T1)$ and $D_w(T2)$ are the averaged calculated absorbed doses to water.

Chapter 6

Discussion

Up until now results from TPS modelling of block and anthropomophic phantoms in TBI conditions (Ch. 4) and linac measurements in TBI conditions (Ch. 5) have been presented. The goal of this chapter is to compare, contrast and discuss the treatment planning modelled data with measured data so we can evaluate Monaco and the existing spreadsheet calculation for TBI planning. Measured and modelled results will be compared on a DD basis using Eq. 2.17 where D_1 corresponds to measured results, and D_2 are TPS modelled results. Since our linac measurements primarily used the PMD which was evaluated in Ch. 3, we will also be discussing the use of the PMD in relation to the data acquired.

Firstly measured and modelled profiles and TPRs in the block-phantom geometry will be compared using both the CCC and MC algorithms for both T1 and T2 treatment rooms. Next point doses and depth doses will be compared in an anthropomorphic phantom for select slices, with the aim of achieving a broad evaluation of DD between film, diode and Farmer chamber measurements and the TPS CCC model of RANDO. Comparisons to the existing spreadsheet will then be made for discussions around existing treatment planning. Finally an overall discussion and summary will be made discussing the results of this thesis as a whole which will lead into the conclusion and future research in this area.

Block Phantom

For comparison of the TPS model with linac measurements in a block-phantom geometry, the measurement of profiles and TPRs in Sec. 5.4.2 were corrected by interpolated wall scatter results for depths 30 cm to 60 cm as discussed in Sec. 5.3. The wall scatter-corrected measurements were then compared with TPS modelled results by DD comparison using Eq. 2.17 where D_1 corresponds to normalized measured doses and D_2 are normalized modelled doses in Monaco. Monaco modelled results were clinically acceptable if $DD < 6\,\%$, this is because the maximum uncertainty of the measured and modelled results when combined was 4 % (with 95 % confidence interval), therefore if the DD was greater than 6 %, then there may exist some values where the true value of DD may exceed 10 % given the uncertainty. This would therefore be outside of the TG-17 required TBI accuracy [13,14] and hence why 6 % was chosen as

the cut-off for clinically acceptable agreement.

This section will evaluate the MC and CCC Monaco models in both T1 and T2 treatment rooms with the aim of quantitatively determining the agreement between profiles measured in Ch. 5 and those calculated using Monaco in Ch. 4. This determines whether using Monaco is feasible at eSSD with simple phantom and setup geometries, to provide justification for or against making comparisons in more complex (heterogeneous) media with an anthropomorphic phantom.

6.1.1 MC Model Comparison

Due to the qualitative noisy appearance of the MC model as discussed in Sec. 4.1.2.1, only tabulated DD comparisons were analysed for the MC model rather than graphical analysis.

	OAD (cm)										
Depth (cm)	0	10	20	30	40	50	60	70	80	90	100
2	10.78%	17.13%	4.10%	15.86%	12.20%	1.53%	16.09%	10.48%	5.50%	-16.50%	-35.88%
5	-11.01%	14.33%	-1.73%	13.80%	21.84%	5.65%	8.97%	10.09%	5.69%	-16.54%	-53.91%
10	0.00%	10.82%	-4.58%	17.92%	2.63%	8.68%	10.04%	-3.69%	18.14%	-9.59%	-34.88%
20	-7.97%	16.46%	18.82%	18.77%	0.13%	0.38%	10.03%	19.39%	6.87%	-7.86%	-26.65%
30	0.64%	13.18%	-2.03%	3.04%	17.93%	7.70%	-13.60%	1.52%	21.04%	-30.12%	67.91%
40	-3.05%	-3.13%	-7.33%	5.29%	44.51%	9.84%	-0.95%	24.06%	-7.35%	-18.24%	45.92%
50	17.38%	0.50%	19.83%	18.65%	0.93%	16.84%	34.00%	13.03%	-1.02%	72.13%	46.84%
60	5.86%	1.03%	14.61%	18.92%	21.58%	39.34%	41.17%	39.40%	7.28%	-1.74%	90.76%

Table 6.1: T1 Table of DD between measured and MC modelled OOARs for various OADs and depths colour coded for specific DD thresholds. Green where DD $< 3\,\%$, yellow where DD $< 6\,\%$, red where DD $> 6\,\%$.

	OAD (cm)										
Depth (cm)	0	10	20	30	40	50	60	70	80	90	100
2	-2.40%	1.72%	-3.61%	2.26%	-8.73%	-4.57%	4.24%	8.15%	4.87%	-0.42%	6.19%
5	-1.13%	-2.31%	-3.08%	-2.30%	-6.04%	-3.57%	-0.18%	1.76%	5.12%	1.41%	3.22%
10	0.00%	-1.73%	-3.75%	-3.66%	-5.66%	-5.53%	1.87%	-1.54%	4.69%	-0.65%	0.32%
20	-2.15%	-9.64%	-0.96%	-5.40%	-9.25%	-5.55%	-5.72%	-4.47%	-4.94%	-0.15%	-2.89%
30	-3.57%	-10.41%	-4.79%	-7.00%	-12.15%	-4.23%	-3.53%	-5.29%	-4.07%	-4.42%	-7.74%
40	-8.10%	-4.64%	6.78%	-0.58%	-5.37%	-3.65%	-1.81%	-0.60%	-2.39%	-3.35%	7.37%
50	-4.70%	-10.96%	-5.24%	-2.53%	-11.18%	-1.60%	-12.50%	-6.59%	-3.97%	-17.49%	-4.13%
60	-3.55%	-3.96%	-4.52%	-6.21%	-0.76%	4.24%	-1.35%	6.26%	-3.81%	-8.31%	-1.72%

Table 6.2: T2 Table of DD between measured and MC modelled OOARs for various OADs and depths colour coded for specific DD thresholds. Green where DD $< 3\,\%$, yellow where DD $< 6\,\%$, red where DD $> 6\,\%$.

Poor agreements between measured and modelled profiles and TPRs are shown by Tables 6.1 and 6.2 over the entire range of off axis distances and depths for T1 and T2. While there are fewer points of difference exceeding $6\,\%$ in T2 compared with T1, T2 still contains several points of difference which

could not be characterised. These comparisons show that the MC algorithm cannot be used with the existing beam model in both T1 and T2 TBI geometries.

6.1.2 CCC Model Comparison

6.1.2.1 T1 Treatment Room

With respect to profiles and TPRs for T1 (shown in Fig. 6.1, Fig. 6.2, Fig. 6.3 and Fig. 6.4 below) we show with Table 6.3 that either the Monaco TPS model breaks down >80 cm or the measure of charge rate in the penumbral region has too great of an uncertainty due to steep dose gradients (with uncertainty in dose being affected significantly more with small uncertainties in chamber localisation) and the dose rate being much lower relative to the central axis dose. However since the usable field region for T1 is 120 cm, TPRs modelled only need to be valid to 60 cm off-axis distance. The maximum DD is 5.77 % (from table 6.3) up to 60 cm off-axis, with the most common DD being in the 3 % range (median of 3.04 %). The DD results for T1 show clinically acceptable agreement between the Monaco and measurement over 2 cm to 60 cm depths within the clinically useful field size.

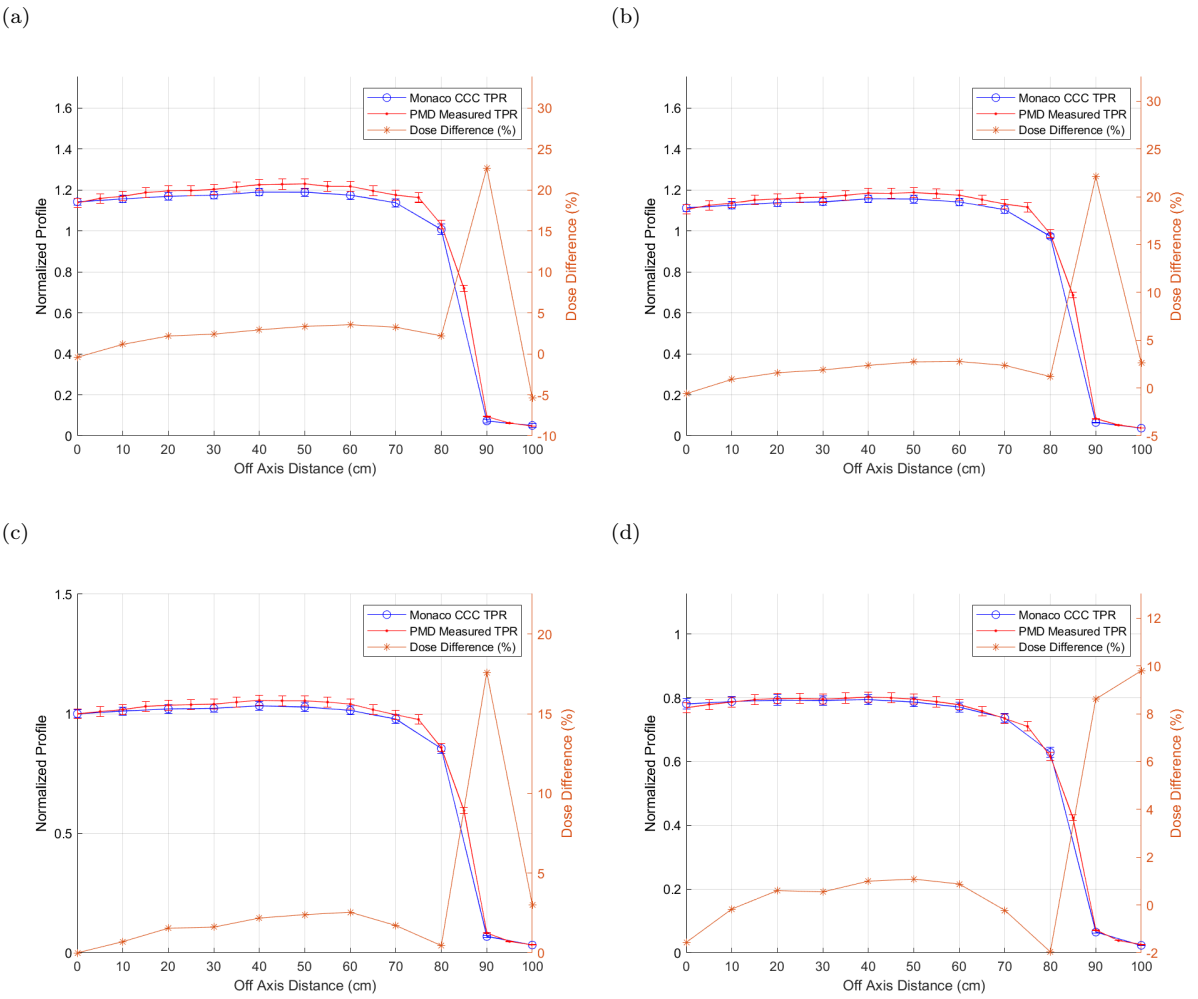

Figure 6.1: T1 Profiles for depths (a) 2 cm (b) 5 cm (c) 10 cm (d) 20 cm, normalized to the point where output was measured. Profiles, simulated in Monaco (blue), measured with the PMD (red), and compared by DD (orange). Uncertainty bars represent 95 % confidence intervals.

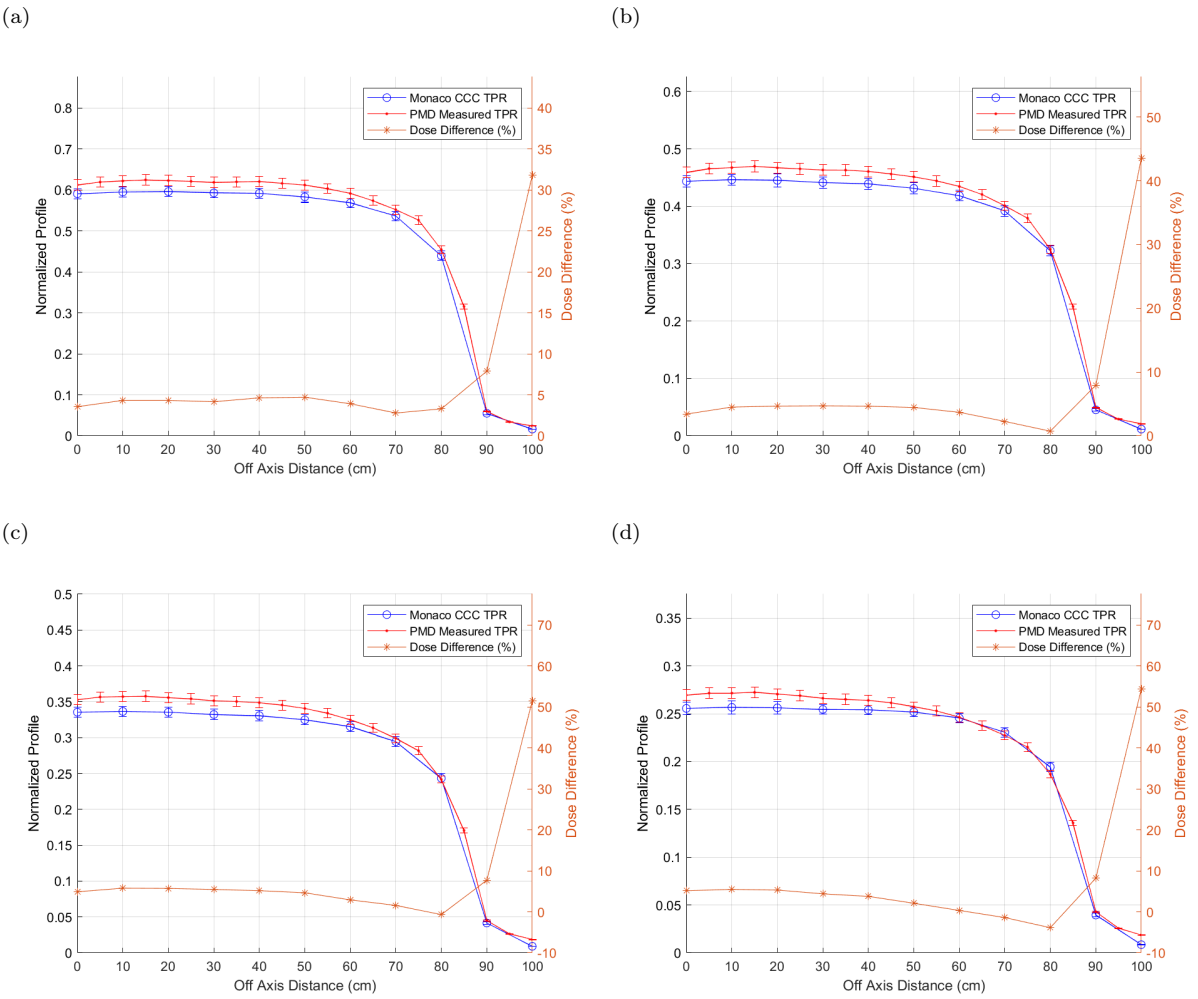

Figure 6.2: T1 Profiles for depths (a) 30 cm (b) 40 cm (c) 50 cm (d) 60 cm, normalized to the point where output was measured. Profiles simulated in Monaco (blue), measured with the PMD (red), and compared by DD (orange). Uncertainty bars represent 95 % confidence intervals.

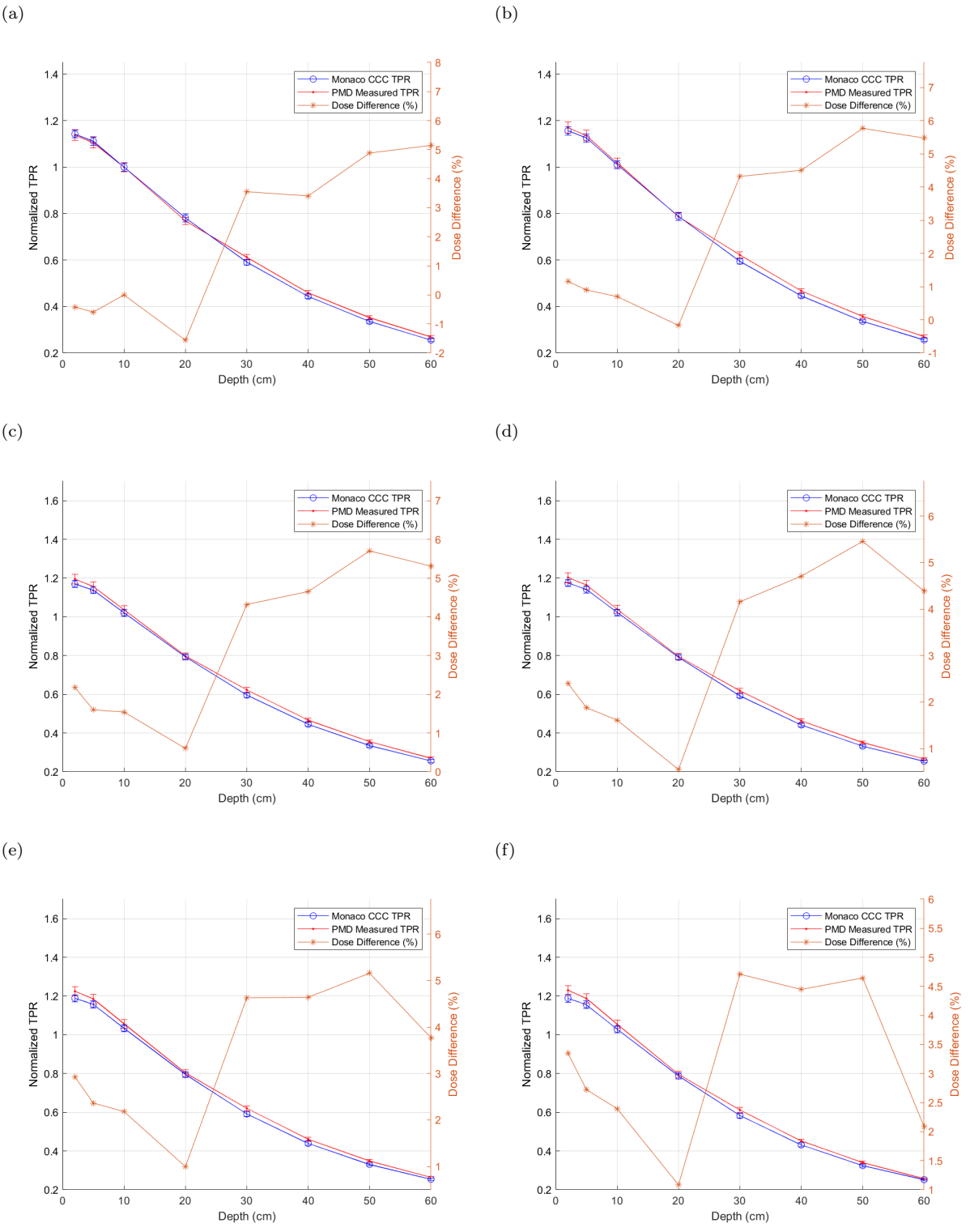

Figure 6.3: T1 TPRs for OADs (a) 0 cm (b) 10 cm (c) 20 cm (d) 30 cm (e) 40 cm (f) 50 cm, normalized to the point where output was measured. TPRs simulated in Monaco (blue), measured with the PMD (red), and compared by DD (orange). Uncertainty bars represent 95 % confidence intervals.

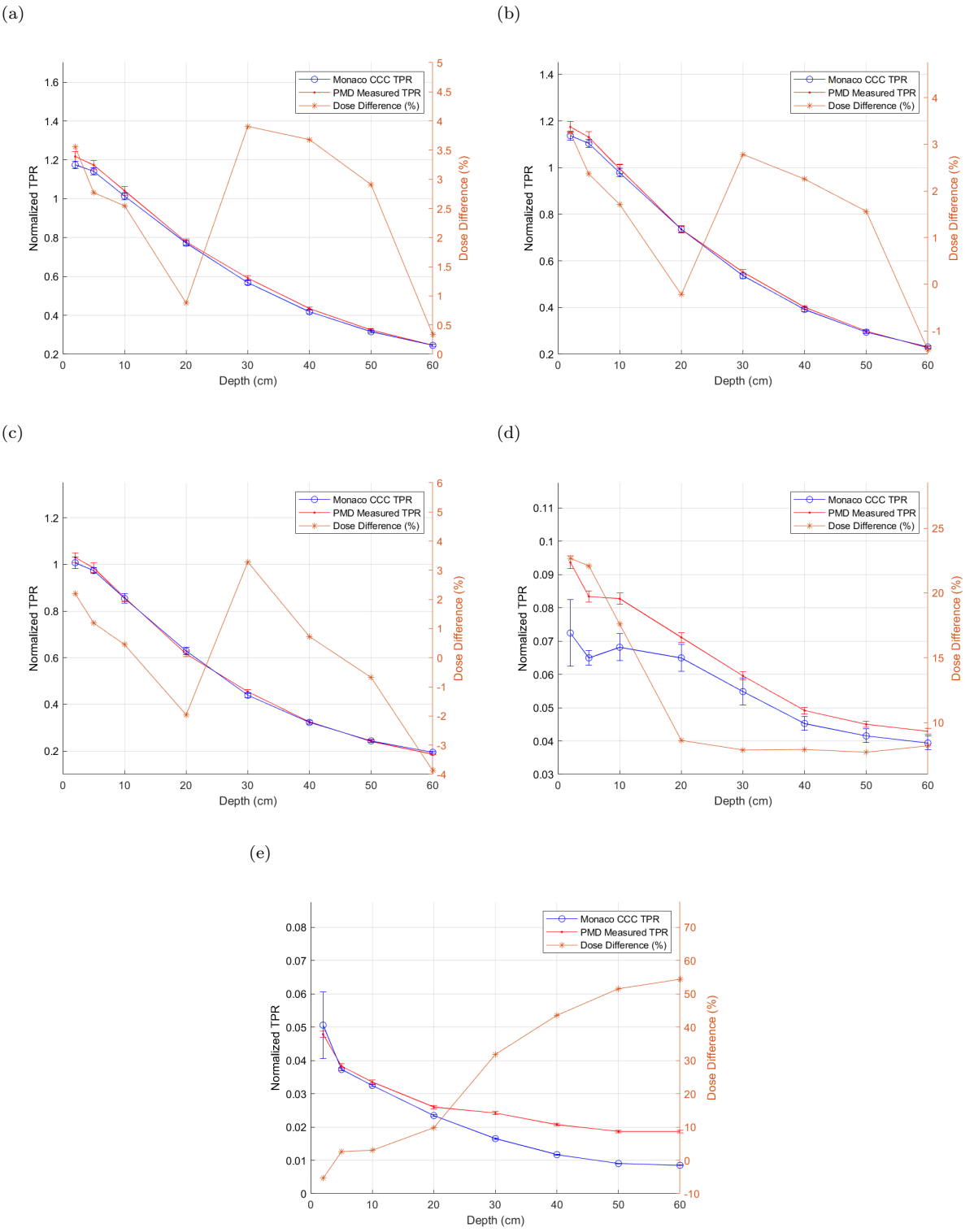

Figure 6.4: T1 TPRs for OADs (a) 60 cm (b) 70 cm (c) 80 cm (d) 90 cm (e) 100 cm, normalized to the point where output was measured. TPRs simulated in Monaco (blue), measured with the PMD (red), and compared by DD (orange). Uncertainty bars represent 95 % confidence intervals.

	OAD (cm)										
Depth (cm)	0	10	20	30	40	50	60	70	80	90	100
2	-0.42 %	1.15 %	2.18 %	2.40 %	2.93 %	3.35 %	3.55 %	3.25 %	2.20 %	22.67 %	-5.41 %
5	-0.59 %	0.90 %	1.60 %	1.88 %	2.36 %	2.72 %	2.77 %	2.36 %	1.19 %	22.10 %	2.62 %
10	0.00 %	0.70 %	1.54 %	1.61 %	2.18 %	2.40 %	2.55 %	1.71 %	0.45 %	17.59 %	3.02 %
20	-1.56 %	-0.17 %	0.60 %	0.55 %	1.00 %	1.08 %	0.88 %	-0.22 %	-1.96 %	8.61 %	9.80 %
30	3.55 %	4.32 %	4.32 %	4.16 %	4.63 %	4.71 %	3.91 %	2.78 %	3.29 %	7.88 %	31.80 %
40	3.41 %	4.51 %	4.65 %	4.71 %	4.64 %	4.45 %	3.68 %	2.25 %	0.73 %	7.92 %	43.53 %
50	4.88 %	5.77 %	5.70 %	5.46 %	5.16 %	4.65 %	2.91 %	1.56 %	-0.68 %	7.70 %	51.52 %
60	5.15 %	5.48 %	5.31 %	4.39 %	3.77 %	2.09 %	0.34 %	-1.41 %	-3.87 %	8.20 %	54.37 %

Table 6.3: T1 Table of DD between measured and CCC modelled OOARs for various OADs and depths colour coded for specific DD thresholds. Green where DD $< 3\,\%$, yellow where DD $< 6\,\%$, red where DD $> 6\,\%$.

6.1.2.2 T2 Treatment Room

With respect to Profiles and TPRs for T2 (shown by Fig. 6.5, Fig. 6.6, Fig. 6.7 and Fig. 6.8) it is shown that the Monaco TPS model breaks down at points 2 cm depth and 90 cm off-axis, 50 cm depth and 100 cm off-axis, and 60 cm depth for off-axis distances greater than 60 cm. Since the usable field region for T2 is 170 cm, TPRs modelled only need to be validated to 85 cm off-axis distance. The maximum DD is $-10.78\,\%$ (from Table 6.4) up to 90 cm off-axis, with the most common DD being in the $1\,\%$ range (median of $1.32\,\%$). The DD results for T2 show clinically acceptable agreement between Monaco and measurement over 5 cm to 50 cm depths over the clinically useful field size, with 60 cm depth acceptable up to 60 cm off-axis.

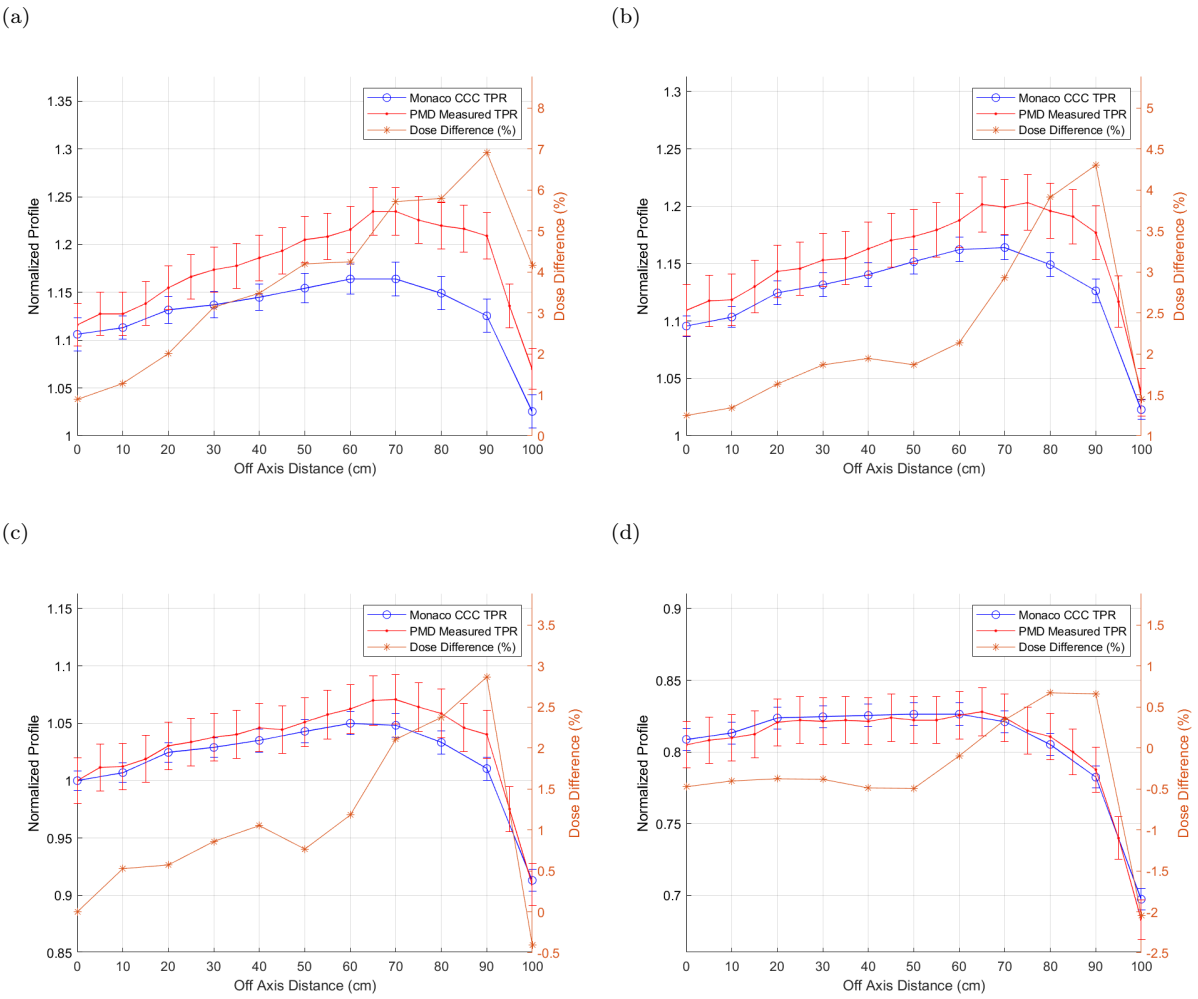

Figure 6.5: T2 Profiles for depths (a) 2 cm (b) 5 cm (c) 10 cm (d) 20 cm, normalized to the point where output was measured. Profiles simulated in Monaco (blue), measured with the PMD (red), and compared by DD (orange). Uncertainty bars represent 95 % confidence intervals.

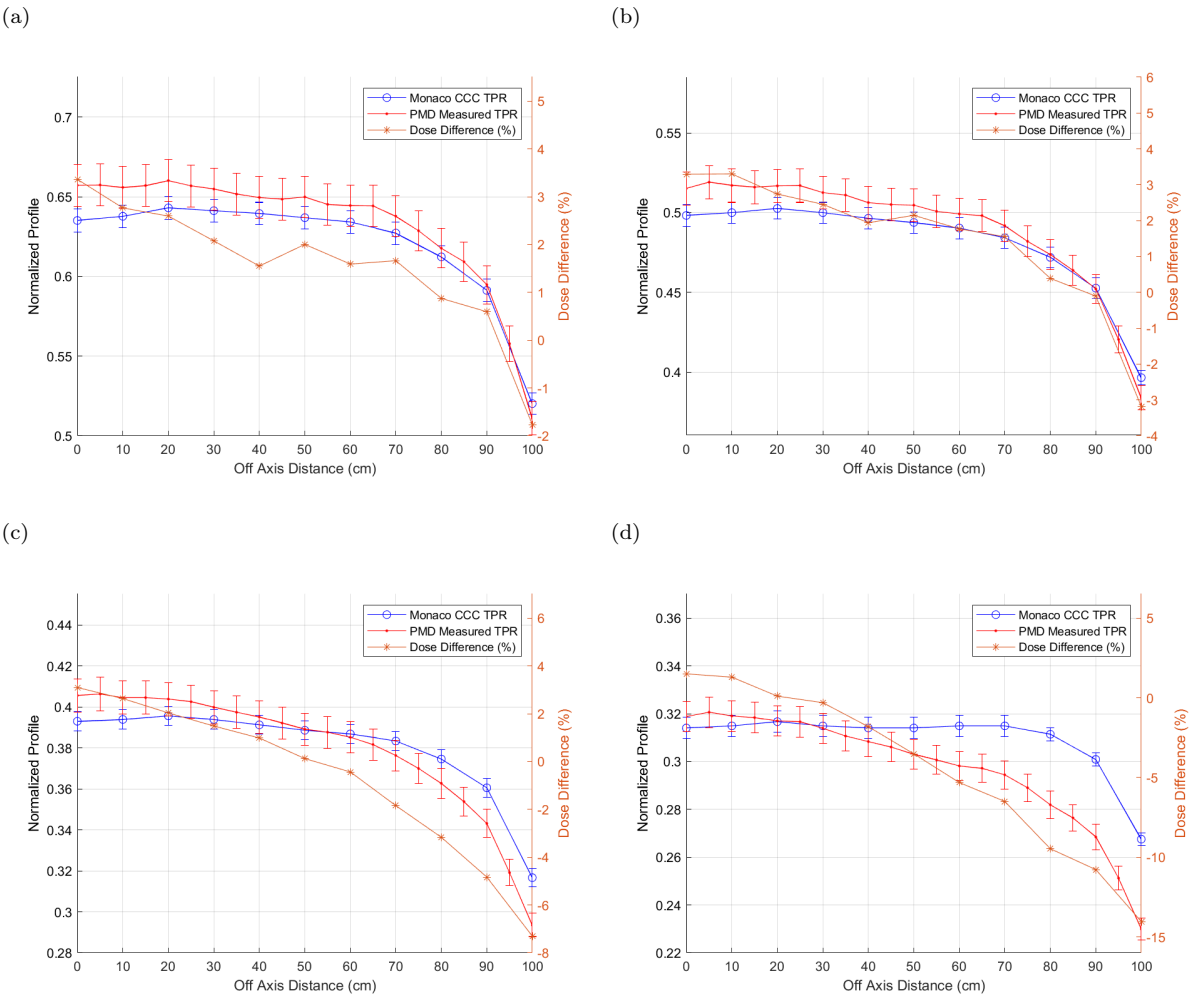

Figure 6.6: T2 Profiles for depths (a) 30 cm (b) 40 cm (c) 50 cm (d) 60 cm, normalized to the point where output was measured. Profiles, simulated in Monaco (blue), measured with the PMD (red), and compared by DD (orange). Uncertainty bars represent 95 % confidence intervals.

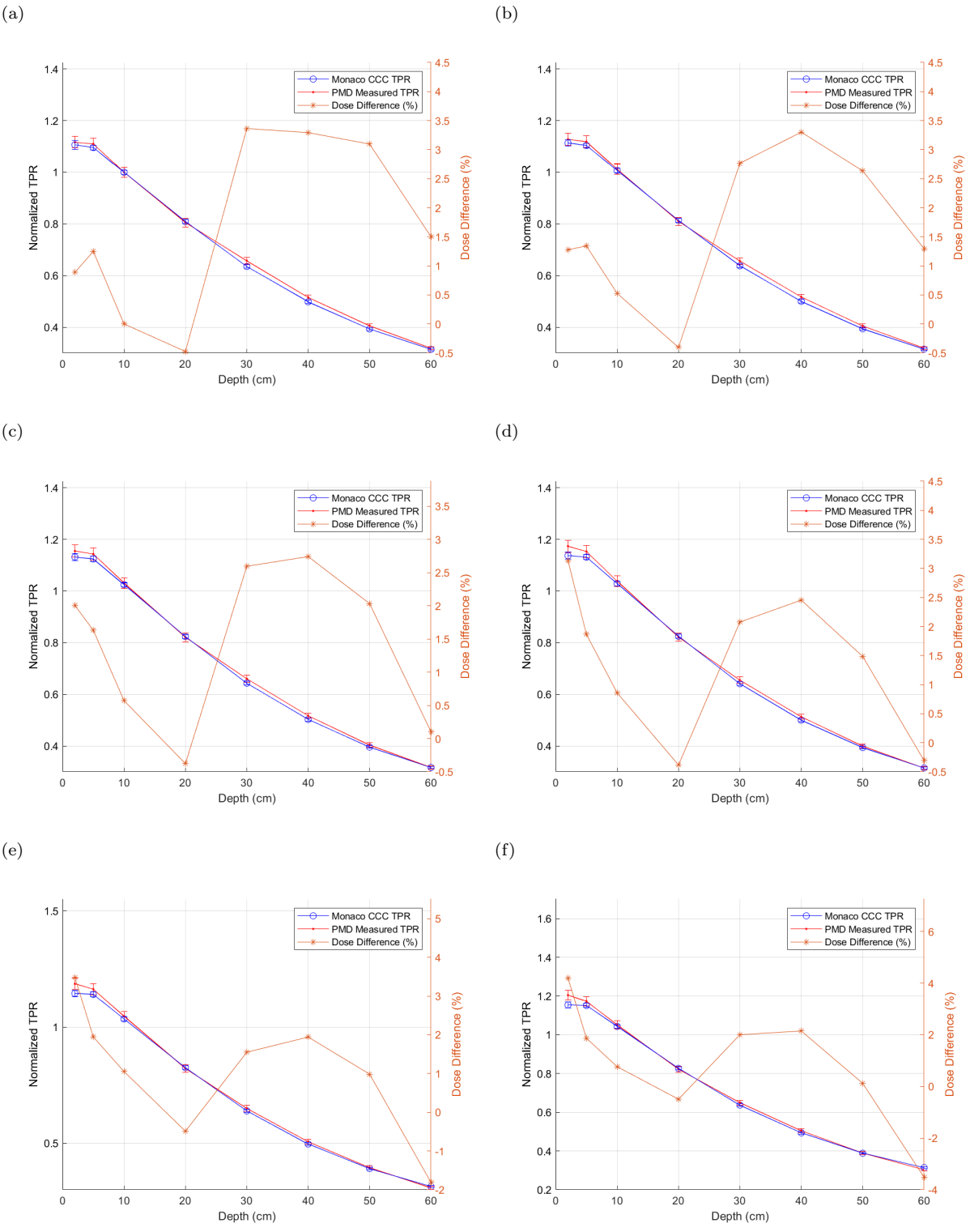

Figure 6.7: T2 TPRs for OADs (a) 0 cm (b) 10 cm (c) 20 cm (d) 30 cm (e) 40 cm (f) 50 cm, normalized to the point where output was measured. TPRs, simulated in Monaco (blue), measured with the PMD (red), and compared by DD (orange). Uncertainty bars represent 95 % confidence intervals.

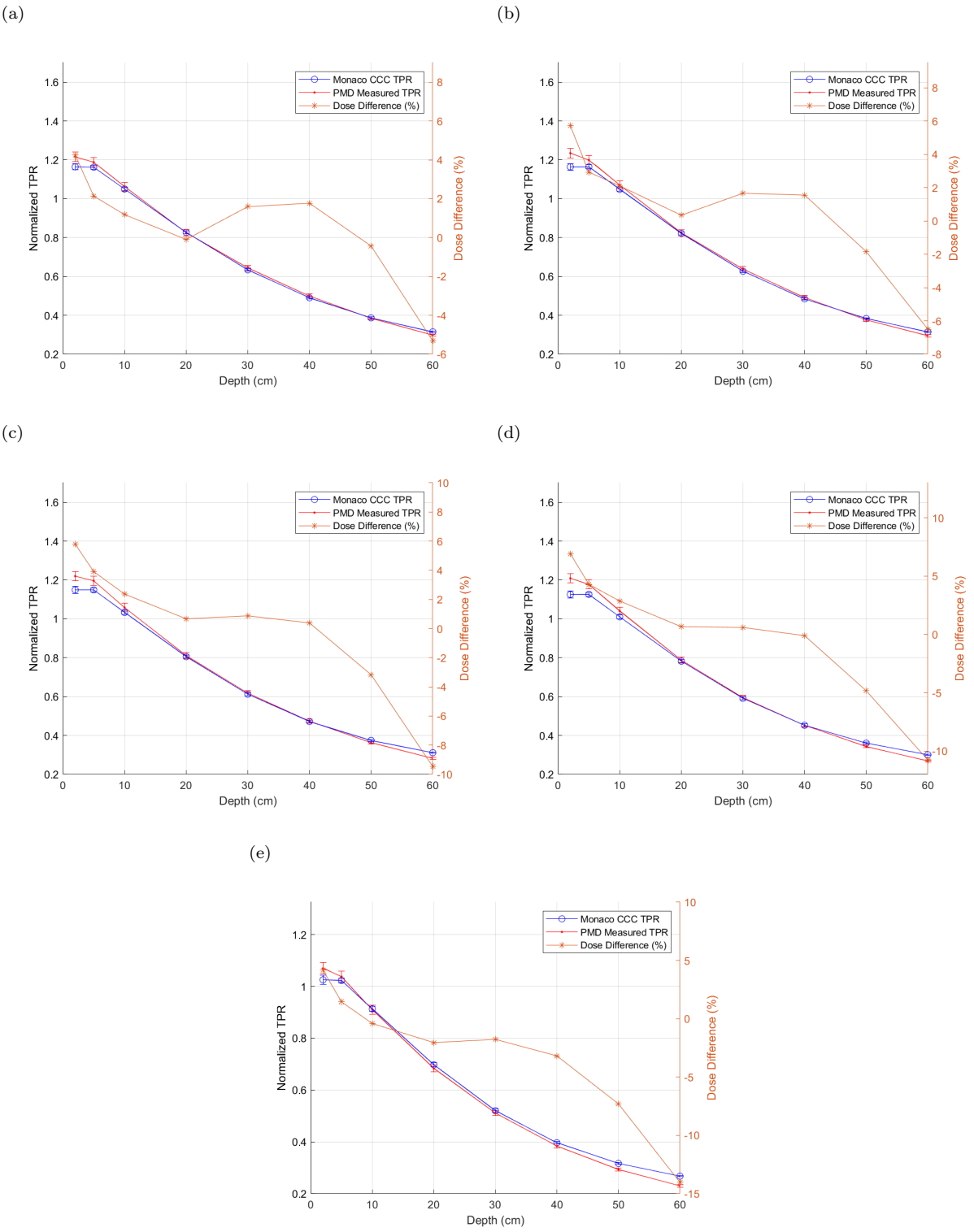

Figure 6.8: T2 TPRs for OADs (a) 60 cm (b) 70 cm (c) 80 cm (d) 90 cm (e) 100 cm, normalized to the point where output was measured. TPRs, simulated in Monaco (blue), measured with the PMD (red), and compared by DD (orange). Uncertainty bars represent 95 % confidence intervals.

	OAD (cm)										
Depth (cm)	0	10	20	30	40	50	60	70	80	90	100
2	0.89 %	1.28 %	2.01 %	3.14 %	3.48 %	4.20 %	4.24 %	5.71 %	5.79 %	6.92 %	4.16 %
5	1.25 %	1.34 %	1.63 %	1.87 %	1.94 %	1.87 %	2.14 %	2.93 %	3.91 %	4.30 %	1.45 %
10	0.00 %	0.53 %	0.57 %	0.86 %	1.05 %	0.77 %	1.18 %	2.10 %	2.37 %	2.86 %	-0.40 %
20	-0.47 %	-0.40 %	-0.38 %	-0.38 %	-0.49 %	-0.50 %	-0.10 %	0.34 %	0.67 %	0.66 %	-2.04 %
30	3.36 %	2.77 %	2.60 %	2.08 %	1.55 %	2.00 %	1.59 %	1.66 %	0.87 %	0.60 %	-1.77 %
40	3.29 %	3.30 %	2.74 %	2.45 %	1.94 %	2.15 %	1.77 %	1.55 %	0.39 %	-0.10 %	-3.18 %
50	3.10 %	2.63 %	2.03 %	1.49 %	0.98 %	0.12 %	-0.43 %	-1.84 %	-3.17 %	-4.83 %	-7.30 %
60	1.50 %	1.29 %	0.10 %	-0.31 %	-1.81 %	-3.52 %	-5.32 %	-6.50 %	-9.47 %	-10.78 %	-14.04 %

Table 6.4: T2 Table of DD between measured and CCC modelled OOARs for various OADs and depths colour coded for specific DD thresholds. Green where DD $< 3\,\%$, yellow where DD $< 6\,\%$, red where DD $> 6\,\%$.

6.1.2.3 Summary of Block Phantom Comparisons

For both T1 & T2 we had to take into consideration the clinically useful field regions and the depths of TCPE (discussed in Sec. 2.1.3.1 and Sec. 2.1.4.1). The clinically useful field regions were previously defined as up to 60 cm & 85 cm (for half the beam), and the depths where TCPE applies are those above 2.5 cm & 3 cm for T1 & T2 respectively. Measured dose discrepancies for ionisation chambers in the buildup region are much greater than those measured when TCPE is established.[52] Additionally the AAPM Task Group 53 (TG-53) provides a tolerance for TPS determined point doses which is large ($\pm 20\,\%$)[53] in this buildup region. Therefore for conclusions drawn with respect to feasibility, use of Monaco should be constrained to the depths between 5 cm to 60 cm for T1, 5 cm to 50 cm for T2, and off-axis distances between 0 cm to 60 cm (T1) and 0 cm to 85 cm (T2). Subsequent modelling with anthropomorphic phantoms should note these as depth and off-axis positional constraints for the interpretation of data and potential use for patient dose calculations.

Overall depths between 50 cm and 60 cm are less important clinically to the total dose, since the patient is treated bilaterally these output doses are weighted significantly less than the input doses from each side. Additionally, much like the argument made for 2 cm depth, the dose delivered at 60 cm depth would also be delivered to the perspex panel on the opposite side (maximum treatment side panel internal separation of 57.5 cm). The comparisons for depths 30 cm to 50 cm also show that there are greater uncertainties in the surface of the widest region of the patient (i.e around the shoulder furthest from the beam).

Anthropomorphic Phantom

It has been shown in the previous section that Monaco can effectively predict dose distributions in homogeneous phantoms at the eSSDs used clinically, given certain off axis and depth constraints. Following from this film, diode and farmer chamber dosimetry were used to measure point doses at various depths

in RANDO, and were compared with Monaco and spreadsheet calculated doses at identical points. The maximum uncertainties of measurement and modelled doses combined were all approximately 4 % and hence a 6 % DD was determined to be the cut-off for clinically acceptable agreement between Monaco and measured results. This section provides a comparison between measured point doses and Monaco's CCC and spreadsheet calculated doses so that the Monaco and the existing treatment planning methods can be evaluated in a heterogeneous phantom. First, point doses measured with film will be compared with identical points in Monaco. In-vivo point doses measured using diodes and Farmer chambers will then be compared with Monaco point doses. A comparison will then be made between the existing spreadsheet calculated midline and peak lung doses to film and diodes measurements are provided along with contrasting comparisons with those made to Monaco, with the aim of determining the superior treatment planning approach. Finally comparisons will be summarised to provide a clearer picture of the conclusions drawn.

6.2.1 Film Comparisons

Differences between Monaco and film measured depth doses are shown by Fig. 6.9 below for T1 and T2. These comparisons were made using Eq. 2.17 with film measured doses from Ch. 5 being D_1 and Monaco calculated doses from Ch. 4 being D_2.

(a) (b)

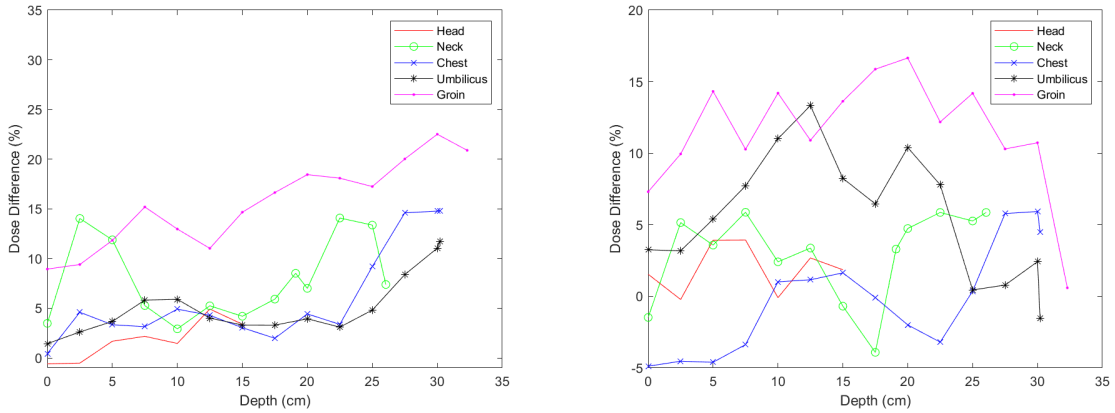

Figure 6.9: Dose differences between film measured and Monaco modelled depth doses for (a) T1 treatment room and (b) T2 treatment room.

For T1, Fig. 6.9a shows that there are a few regions where Monaco and measured results are not within clinically acceptable agreement. For the groin, there is no clinically acceptable agreement between measured film results and Monaco calculated results for all depths in RANDO. The neck region also has several points of disagreement, and is only clinically acceptable between 7.5 cm to 17.5 cm depths and at the entrance 0 cm depth. The chest, umbilicus and head regions are regions of best agreement, with

the chest being clinically acceptable over 0 cm to 22.5 cm depths, the umbilicus is clinically acceptable over 0 cm to 25 cm depths, and finally the head is clinically acceptable over its entire 15 cm depth.

Similar to T1, T2's results shown in Fig. 6.9b also show a few regions of significant disagreement. The groin region only has one point of clinical agreement at the exit depth of 32.5 cm. The umbilicus region has a range of disagreement between 7.5 cm to 22.5 cm depths and is only clinically acceptable outside of this range. The chest, neck and head are all within clinically acceptable agreement over their entire 30.2 cm, 26 cm, and 15 cm respective depths.

There are a few potential reasons why some depths in regions validate where others do not. The first reason are potential errors in measurement setup both geometrically and with rice bag packing. The entire RANDO phantom was extremely difficult to setup in a reproducible way when rice bags and spoilers were included, therefore this may have added in additional uncertainties which may have been unaccounted (or improperly accounted for the rice bag packing case) for in the model. Additionally RANDO is not a perfect model of a patient as has a hard exterior shell meaning that rice bags are not packed as conformally and efficiently compared to an actual patient. These difficulties in setup may have contributed to additional unexpected uncertainties in the measurements which could cause larger differences of agreement than expected. A second reason could be errors with calibration of the film, this is unlikely as the response from all three colour channels qualitatively seemed to be as expected and uncertainties were used appropriately to account for film processing. However, it is possible that uncertainties with calibration and processing of film (when used according to protocol) were greater than shown in literature and this could have contributed to additional discrepancies in dose. Thirdly the CCC model in Monaco may not appropriately be determining the scatter and absorption from inhomogeneities correctly at eSSD. It qualitatively looks like DDs are less clinically acceptable in regions where there are more dense (bony) inhomogeneities distributed through the region like the Groin, Neck and Umbilicus. Therefore it could be a case where Monaco's CCC algorithm does not properly consider the scatter and absorption processes correctly in the dense inhomogeneities and therefore in regions where there are more distributed throughout there are larger dose discrepancies between measured and modelled doses. Finally there may be other unknown influencing factors not considered which may have contributed to additional dose discrepancies between measured and modelled doses.

6.2.2 Diode Comparisons

Comparisons between measured diode results from Sec. 5.5.2 and those determined with similar points in Monaco from Sec. 4.2.2.2 were made by averaging the doses from the left and right fields for each point and then calculating the DD using Eq. 2.17 with D_1 being diode measured dose and D_2 Monaco modelled dose.

	Region				
Comparison	Head	Neck	Chest	Umbilicus	Groin
T1 Average ENT DD	2.48 %	2.98 %	-1.66 %	-4.45 %	0.09 %
T1 Average EXIT DD	-1.80 %	2.21 %	12.01 %	-1.74 %	11.58 %
T2 Average ENT DD	4.00 %	5.65 %	3.75 %	-0.22 %	1.79 %
T2 Average EXIT DD	-2.88 %	1.63 %	13.86 %	-0.86 %	8.85 %

Table 6.5: DDs between measured diode doses and Monaco modelled doses for similar points in RANDO, averaged from the left and right fields for both T1 and T2. Green where DD $< 3\,\%$, yellow where DD $< 6\,\%$, red where DD $> 6\,\%$.

It is shown in Table 6.5 that the averaged entrance doses have good agreement between measurement and Monaco for all regions. For exit doses however, the chest and groin exit doses exceed the clinically acceptable dose difference. The DD in approximate peak lung dose is $1.756\,\%$ and $7.096\,\%$ for T1 and T2 respectively. These DDs show Monaco underestimates the peak lung dose for both linacs, for T1 the DD is within clinically acceptable agreement, however for T2 no clinically acceptable agreement exists for the approximate peak lung dose. It is important to note that what is called the peak lung dose is not actually within the lung but rather the dose at the surface of the skin closest to the lung (armpit). This means the "peak lung dose" is an overestimate of the true peak lung dose and therefore this being underestimated is not necessarily an issue clinically as may actually be more representative of the true peak lung dose which would be less than the dose at the surface closest to the lung. Additionally we can see the difference is not too far from clinical significance (only $1.096\,\%$ off) and this difference in representation (being an additional few centimeters of skin) could actually make up this difference, meaning that this underestimation may be acceptable when additional depth is considered.

There are a few potential reasons why the chest and groin exit doses have significant dose discrepancies between Monaco and diode measurements. These include those mentioned in Sec. 6.2.1, additionally since diodes require an orientation correction factor with an orientation representative of the diode position during measurement, if the diodes during measurement had deviated slightly (due to rice bag packing and placement) this could have had a significant affect on the final measured results for the exit diodes. Ultimately it is unclear why only the chest and groin exit results were not clinically acceptable, this highlights an opportunity for further investigation of diode orientation and measured diode results when using the RANDO phantom.

6.2.3 Farmer Chamber Comparison

The midline groin doses measured with the farmer chamber in Sec. 5.5.3 are compared with those calculated using Monaco in Sec. 4.2.2.3. These are compared by their DDs using Eq. 2.17 where D_1

are the measured doses and D_2 are Monaco calculated doses for the left field. These DDs are shown below for both T1 and T2 treatment rooms:

$$DD(T1) = 0.978\,\%,$$
$$DD(T2) = 0.935\,\%.$$

The small differences in groin dose show a strong, clinically acceptable agreement between the measured and Monaco calculated doses for the left field. Additionally whilst these DDs were only determined for the left fields (since the farmer chamber measurements were only carried out using the left field), it can be seen by inspecting the doses in Sec. 5.5.3 and Sec. 4.2.2.3 that the maximum difference in dose does not exceed 6 %, even if the left field doses are compared with the right field doses. Farmer chamber results are regarded as the most reliable clinically (as uncertainties are well understood) and therefore agreement results have more weight than the diode of film results in terms of supporting the Monaco model results validity.

6.2.4 Spreadsheet Comparison

Spreadsheet midline doses were compared with Monaco midline doses in Sec. 4.2.2.4, it was found that with the exception of one dose (which existed in the penumbra region), that the spreadsheet had a clinically acceptable agreement with Monaco. Just because the two calculation methods agree however does not mean that they necessarily agree with measurement. This section compares spreadsheet calculated doses with measured midline doses from Ch. 5 to evaluate the spreadsheet and discuss with respect to Monaco midline DDs from Sec. 6.2.1. DDs were calculated using Eq. 2.17 with D_1 being film measured or diode-interpolated midline doses and D_2 the Monaco modelled dose.

	Region				
Comparison	Head	Neck	Chest	Umbilicus	Groin
T1 Interpolated Diodes DD	-50.049 %	2.878 %	6.730 %	6.510 %	12.099 %
T1 Film DD	-13.766 %	2.085 %	2.645 %	5.774 %	15.506 %
T2 Interpolated Diodes DD	2.636 %	10.089 %	11.305 %	7.521 %	9.732 %
T2 Film DD	9.106 %	-0.987 %	3.707 %	10.505 %	14.739 %

Table 6.6: DDs between interpolated diode and film measurements and spreadsheet calculated midline doses for T1 and T2. Green where DD $< 3\,\%$, yellow where DD $< 6\,\%$, red where DD $> 6\,\%$.

DDs from Table 6.6 show few areas of clinically acceptable agreement with respect to midline doses. The interpolated diode results and film results are not directly comparable (as the measurement positions differ), so these results do not necessarily show a discrepancy between the measured results themselves, but rather highlights the fact that inhomogeneities are not considered with the existing spreadsheet

since these DDs between film and diode for T1 and T2 should be closer together if inhomogeneities were considered with the spreadsheet.

For T1 the large DD from the head is expected, as this is within the penumbral region, however the discrepancies outside of this region which result in several regions not being within clinically acceptable agreement are concerning. The film DDs do validate the use of the spreadsheet for the calculation of lung doses, though unfortunately for every point of agreement (the exception being the T1 neck DD) with one measurement type, there seems to be a contradicting point of disagreement from the other measurement type. This makes it very difficult to make an accurate conclusion based on this alone.

The groin dose was also similarly compared with Farmer chamber measurements made and DDs were found to be:

$$DD(T1) = -2.622\,\%,$$
$$DD(T2) = -0.558\,\%.$$

These DDs indicate the spreadsheet has clinically acceptable agreement between measured and modelled results for the groin midline, this differs from Table 6.6 where midline doses for the groin region had no clinical agreement whatsoever. As discussed earlier the positions of measurement devices differed and therefore are not directly comparable. These differences may have more to do with how the spreadsheet deals with changes in positions and lack of inhomogeneity consideration.

The peak lung dose was also compared with averaged diode measurements from Sec. 5.5.2, the DDs were determined to be:

$$DD(T1) = 6.624\,\%,$$
$$DD(T2) = 8.159\,\%.$$

With respect to the peak lung DDs above, no clinically acceptable agreement exists for either T1 or T2. The spreadsheet underestimates the peak lung dose significantly more than Monaco does (in Sec. 6.2.2). Overall the spreadsheet shows poor agreement with measurement with the Farmer chamber measurement being the exception. The spreadsheet calculation has fewer regions which are within clinically acceptable agreement than Monaco. It is important to note that what is considered to be the peak lung dose is not actually within the lung but rather the dose at the surface of the skin closest to the lung (armpit). This means what we call the peak lung dose is an overestimate of the true peak lung dose and therefore this being underestimated is not necessarily an issue clinically as may actually be more representative of the true peak lung dose which would be less than the dose at the surface closest to the lung. Additionally we can see the difference is not too far from clinical significance (only 2 % to 3 % off) and this difference in representation (being an additional few centimeters of skin) could actually make up this difference, meaning that this underestimation could be technically acceptable as it considers additional depth.

Overall it is unclear exactly why the spreadsheet results are not clinically acceptable when compared with film and diode measurements however are clinically acceptable when compared with the Farmer chamber results. It is possible measurement and setup errors, or lack of inhomogeneity modelling (both discussed in Sec. 6.2.1) may be responsible for some of these differences, however at this stage this is unclear. Farmer chamber results are considered to have the most dosimetric confidence with respect to absolute dose because they are calibrated and used often with limitations well understood. Interestingly the fact that the Farmer chamber measurements agree well with both Monaco and the spreadsheet where film and diodes fail adds significant complications in discussing results appropriately, it does however provide a clear path for future work which can be done to improve results and comparisons made.

6.2.5 Summary

There are several points of clinically acceptable agreement and disagreement between measured and Monaco determined point doses. Results do not definitively show whether Monaco can determine clinically acceptable doses for the key interest regions in a patient. There have been several potential reasons provided as to why dose difference results do not clearly show in all regions clinically acceptable agreement between measured and modelled doses both in Monaco and with the existing spreadsheet. Although several reasons have been provided, ultimately it is unclear why results do not agree, the spreadsheet in particular has been used at Christchurch Hospital for several years, and there have been no reported issues from ROs or physicists in terms of toxicities like interstitial penumonitis arising from overdoses, or ineffective treatments from underdoses. The uncharacterisable disagreement between diode and film measured and modelled results, and strong agreement between Farmer chamber measured and modelled results show a clear need for further investigation of doses for clinical recommendations to be made.

Whilst no issues have been reported with the current technique thus far, accurate dosimetry for TBI using treatment planning systems is still necessary to allow for patient specific modelling of dose distributions. This will bring the TBI treatment approach into line with other modern radiation therapy treatment techniques, and allow for better TBI treatment outcomes for patients overall.

Chapter 7

Conclusion

Summary

The work in this thesis was driven by two main goals. One was to develop and validate a PMD for improving the accuracy of profile and TPR acquisition under eSSD TBI conditions. This has been achieved by discussing and building the device with the UC workshop, validating necessary dosimetry equipment, developing software for automatic profile acquisition, and characterizing the scatter introduced by the PMD.

In Ch. 3 we presented the purpose, design and evaluation of the PMD and relevant dosimetry equipment. Evaluation showed that the temporal resolution of the electrometer was approximately 0.5 s, which was incorporated into the TBIControl software. The PMD in both T1 and T2 was shown to contribute no measurable scatter to a point in a solid water phantom given the measurement uncertainty as is shown by in-air measurement. These characterizations were important to consider when the PMD is used for measurement of profiles and TPRs. Successful measurements of profiles and TPRs were then conducted using the PMD in Ch. 5 and it was shown to be an effective device at significantly reducing the total TBI commissioning measurement time by an order of magnitude, and reducing the uncertainty of measurement point localization from ±2 cm to ±1 mm (95 % confidence interval).

The second goal of this work was to evaluate the Monaco TPS and the existing spreadsheet treatment planning in TBI conditions. This was achieved by comparing Monaco and the spreadsheet with measurements in both simple block-phantom geometries and in a complex anthropomorphic phantom. To do accurate comparisons, several quantities were needed to be both measured and determined, these included wall scatter and diode orientation factors to name a couple.

Ch. 4 presented the necessary introduction, methodology and results evaluating the MC and CCC models in Monaco at eSSD with block-like phantoms. It was found at this stage that the MC model was unsuitable for eSSD as the model was noisy and produced profiles and TPRs which qualitatively looked irregular. Following from this, a CT of the anthropomorphic RANDO phantom was imported with point doses determined for comparison to measured results. Finally a brief comparison between

midline doses calculated using the existing spreadsheet and Monaco showed all but one region were within clinically acceptable agreement with one other, there a couple of significant differences in a few regions.

Measurements for comparison were presented in Ch. 5. Methods, results and discussion for the measurement of dose in both block-like and anthropomorphic phantoms was provided, along with the measurement of wall scatter and diode orientation factor as correction quantities so that an accurate comparison to modelled results could be given. Comparisons between measured results and treatment planning results were then presented in Ch. 6. The complete quantitative comparison given as DDs were shown to effectively determine the agreement between measured and modelled results in both simple block-like phantoms, and complex anthropomorphic phantoms. Comparisons show that for the simple block-like homogeneous phantom, that the existing Monaco CCC model is within 6 % DD between measured and modelled results over the clinically useful field size for T1. For T2 however the model only validates to 6 % in the depth range between 5 cm to 50 cm which is an acceptable constraint for the majority of TBI treatments.

Comparisons to point doses using inhomogeneous anthropomorphic phantoms were the next step once results in homogeneous block phantoms were determined to be clinically acceptable. DD results showed that whilst Monaco seemed to outperform the spreadsheet for various areas, there were still many points where Monaco seemed to disagree with measured results. The point dose measurements in RANDO using the film and diodes were logistically challenging and due to time and resource constraints a larger array of measurements could not be done, these likely could have been reasons for some of the points of disagreement where measurements may not have been performed perfectly. Overall it was unclear why disagreements exist, though there are several areas to investigate which include comparisons with past patient data, remeasuring depth doses in RANDO using a Farmer chamber, the uncertainties associated with changes in amounts of rice bag material, and diode orientation uncertainty with respect to angular differences between the determined orientation factor diode positions and measurement diode positions. At this stage clinical recommendations with respect to the use of Monaco as a TPS for eSSD TBI treatment planning cannot be definitively made, comparison of results indicates an opportunity for further investigation in anthropomorphic phantoms.

Future Prospects

The next logical step in this work would be to re-evaluate dose differences between Monaco and measurement with anthropomorphic phantoms. Rather than measuring point doses, several large 2D dose maps could be measured with pieces of film cut to fit entire RANDO slices, which would allow for a simple overlay comparison of measured and modelled results and direct comparison of measurements made with different dosimetric approaches. The use of a Farmer chamber rather than diodes for measuring entrance and exit doses whilst significantly more time-consuming, would provide superior results with greater confidence to improve upon accuracy of comparisons to Monaco.

Next investigating the depth dose uncertainty with respect to rice bag packing efficiency would provide a clear idea of how significantly differently sized air gaps within and between the rice bags impact the depth dose for various regions in RANDO. This would likely be best done using Farmer chambers for greater confidence in measurements made. Results would provide a quantitative uncertainty associated with the rice bag packing efficiency during measurement rather than an estimated inefficiency built into the model.

The RANDO phantom is not a perfect representation of a patient and measured doses may have been affected by the physical difficulty in packing rice bags due to the hard phantom material and spoiler positions. In practice, rice bag packing is significantly more efficient due to the rice bags conforming easily with the patient's body. Using past and future patient CT data in comparison to in-vivo measurements made during treatments could provide better comparisons between measured and modelled data.

There are a couple of other quantities which would be of interest to investigate. Angular deviations in diode orientation in measurement may mean the orientation factor may not apply correctly to all diodes, especially when curvature (and thus possible angular deviation of the measurement diode) of RANDO depends on diode location. Quantifying the change in orientation factor with respect to angular deviations $< 30^\circ$ and measuring the approximate angular deviation from the orientation factor measurement position of the diode in measurement would provide a more appropriate orientation factor for diodes at their respective positions on RANDO and therefore providing greater measurement accuracy. In Sec. 5.3 the reasoned assumption was made that wall scatter does not need to be considered for Monaco comparison with the anthropomorphic phantom due to rice bag packing and beam spoilers. It would increase the measurement certainty to measure quantitatively whether wall scatter under full TBI patient conditions is significant or not, and therefore whether this negligibly assumption holds true.

Further investigating these potential sources of uncertainty in measurement provides a clear path towards acquiring results with improved accuracy and clinical confidence. These improvements will allow for appropriate clinical recommendations to be made as to whether Monaco can be used as a treatment planning system for TBI treatments at Christchurch Hospital.

Appendix A

Best practices for TBI measurements using the Phantom Mobility Device

Using Solid Water

1. Align farmer chamber to shallowest depth first (i.e. 2cm)
2. Use 50 % Blue SW and 50 % Brown SW.
3. Solid water being stacked from front to back should be stacked in additive amounts which sum up to subsequent depths, i.e. if our measurements are 2 cm, 5 cm, 10 cm, 20 cm, 30 cm then solid water should be stacked (from front to back): 10 cm, 10 cm, 5 cm, 3 cm. This is illustrated by Fig. A.1.
4. Initially 2 cm should be aligned at the centre of the wooden holding tray, this is so that when Solid water is stacked from the back to the front, it can be added up to 30 cm in total without exceeding the bounds of the tray.
5. For depths greater than 30 cm depth, the 30 cm × 30 cm × 30 cm block of water should be used with the chamber block (and up to 10 cm of material including the chamber block) behind the water block, this allows for 40 cm depth + 20 cm depth (up to 60 cm depth) to be done in a single re-align (single realigning from 30 cm × 30 cm × 30 cm to up to 60 cm × 30 cm × 30 cm). This is illustrated by Fig. A.2.

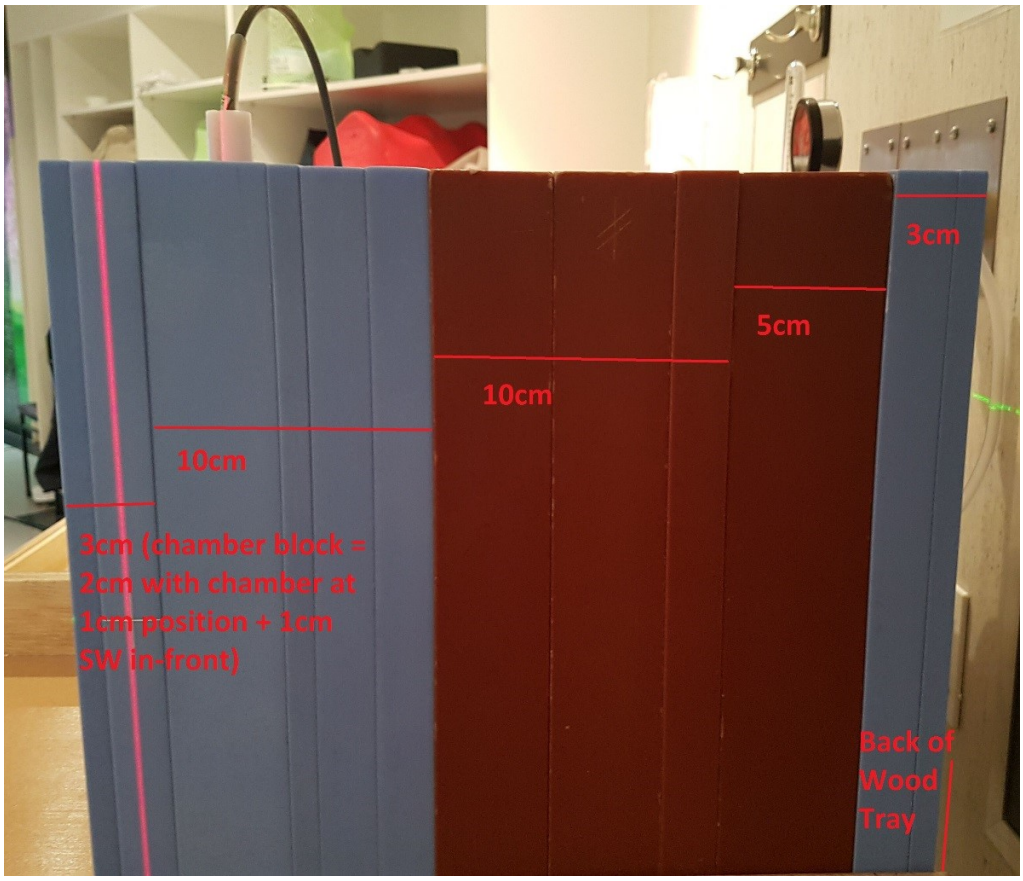

Figure A.1: Solid water set up for up to 30 cm depth.

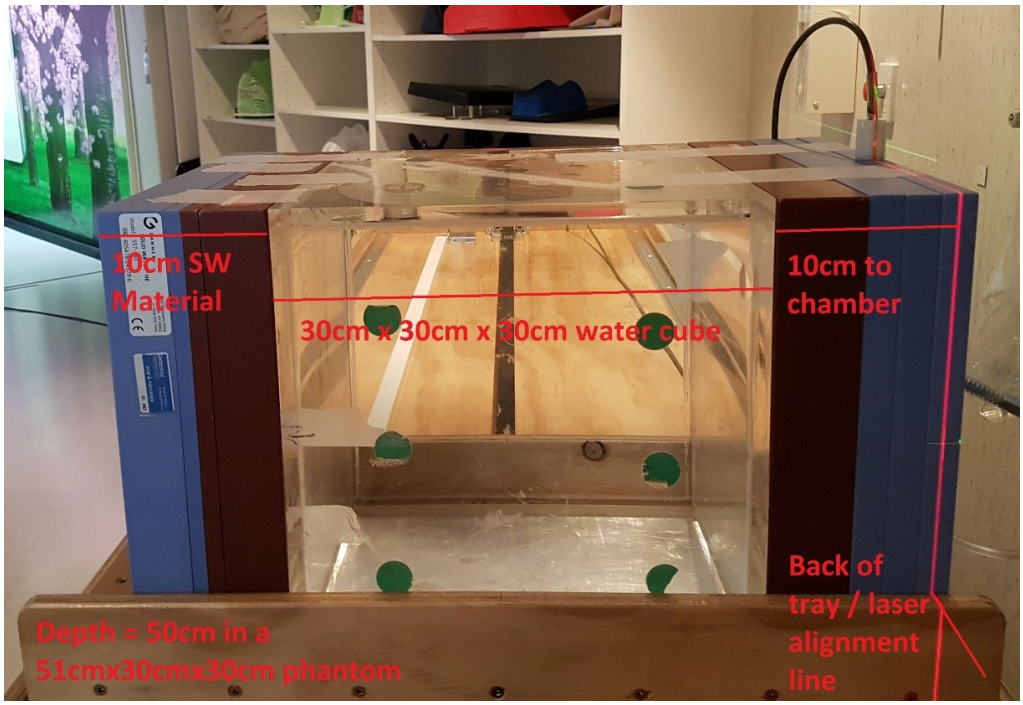

Figure A.2: Solid water and water block set up for measurement depths greater than 30 cm.

Equipment Set-up

1. Set PMD on top of TBI Treatment couch, pushing the corner of the PMD to one of the corners of the TBI couch (and ensuring it stays in this position by pushing it back into the corner when making any changes like moving the couch). The reason this is done is to make sure that the position of the PMD and phantom with respect to the PMD and couch frame are constant throughout measurement and do not become skewed, this allows for quicker repeatability of measurement (as you do not need to continually check alignment once initially aligned) and ensures consistency.
2. Align the PMD with the central axis using the red and green room lasers, align the red laser to the black marked lines which run from end to end of the PMD and through the Solid water holding tray.
3. Plug the leads for the drive and termination points into the PMD from the PMD drive box.
4. Plug the long (coiled) RS232 lead into the PMD drive box and into the computer (using the green/grey RS232 to USB Cable).
5. Plug the Electrometer into the PC using the black RS232 cable.

Beam Control

1. Ensure that T-CTRL mode is used to overcome the 1000 MU limit interlock, such that measurement for long periods (required by the software) can take place, and set Total MU to 9999.
2. Make sure to wait 2 minutes (T2) to 4 minutes (T1) after beam turned on (for T1 and T2 to allow for drifting) before starting each measurement.
3. Once measurements are complete make sure Interlock override has been turned off.

TBIControl Software

A.4.1 Step and Record Mode

1. Select the RS232 ports for the PMD and Electrometer respectively, once connected these should output their model thus allowing you to check you have connected the correct one under the right heading.
2. At the top left hand corner there is a drop down menu, from this select "Step and Record".
3. Specify the PMD Speed (Speed at which the device will move at), time period to record at each step, start position (start position of the PMD), final position and PMD step, and if required

specifying the CAX Position (If this is unspecified it will use the Start position as the CAX Position).

4. Specify the record depths (depths of the chamber to record at), separated by commas.
5. Click Initialize to Initialize the PMD and Zero the electrometer
6. Click "Start", this will re-initialize the PMD and then begin to measure starting at the first depth to record, make sure the beam is ON at this point.
7. At each depth, post measurement it will ask if the measurement has been successful, if there has been a problem with the beam mid-measurement (I.e. Unexpected termination), then wait for this profile measurement to complete, re-run the beam and select "No", this will cause the measurement for the depth to be repeated. If there has been no problems select yes.
8. After selecting yes, the PMD will reinitialize to the CAX point, this will allow for the setup of the water block/solid water for the next measurement depth. Once you have it set up for the next depth, and are ready to go make sure turn the beam back on for 2 minutes (T2) to 4 minutes (T1), to allow for drifting, then hit "OK" on a message box that will prompt asking If it is ready for the next depth.
9. Recommended: Terminate and Redo the beam at each depth or two, in order to make sure that the beam does not reach the MU Limit before the profile measurement completes.
10. Once Measurement complete it will prompt advising this, and will save the data in Json format locally, it will also appear beneath the "Initialize" Button in the Format of SRsave-DDMMYYYYhhmmss (Day Month Year hour minute second).

A.4.1.1 Plotting Controls

- Plotting controls provide a means of a "quick check" of TPRs and Profiles such that one can see if these qualitatively "look right". They do not currently provide statistical analysis and therefore should not be used in lieu of such.
- You can click on the data set (SRsave- or CRsave- depending on Step and Record or Continuous Record), Once clicked on a number of check boxes should show for plotting various OADs/Depths, select those you wish to plot and then click on "Plot Data", this will plot the respective TPRs and Profiles into two graphs.
- There is a normalization control allowing for the normalization of the profiles/TPRs to a specific depth and off-axis position, this can be specified by ticking the "Normalize" box and specifying the depth and off axis Distance to normalize to (a default one for each will be automatically selected).

A.4.2 Individual Electrometer Measurements

1. Select "Electrometer Read" from upper left hand corner dropdown menu
2. Input Time period to record for in seconds.
3. Wait 2 minutes (T2) to 4 minutes (T1) after beam on to allow for drifting.
4. Click "Read", this will read the dose rate every time the buffer updates (or has been more than the buffer update / "temporal resolution" time), and once complete will output the charge rates recorded, the average charge rate, and the standard deviation.

A.4.3 Individual PMD Movement

1. Select "Move PMD" from upper left hand corner dropdown menu.
2. Click Initialize to Initialize the PMD
3. Input the distance to move the PMD by (in mm)
4. Input the speed (in mm/s)
5. Input the movement mode;
    - Absolute move drives the PMD to move to/by distance specified.
    - Relative move either adds or subtracts the move to/by distance from the current distance and drives the PMD to this position.
    - Drive out drives the PMD out to the maximum distance.
    - Drive in drives the PMD in to the minimum distance (nominally 0).

Appendix B

Expression and Evaluation of Uncertainty

Uncertainty in measurement is an important subject to discuss, especially when comparing results and drawing conclusions. The guide to the expression of uncertainty in measurement (GUM) [54] provides a rigorous framework for the evaluation and expression of uncertainties. This framework includes both the expression of absolute and relative uncertainties along with the determination of combined uncertainty for a measured quantity.

The GUM establishes two primary types of uncertainty, type A and type B uncertainties. Type A uncertainties are any uncertainties obtained by statistical analysis of a sample of measurements, these can typically be reduced by increasing the sample size of measurements taken. Type B uncertainties are obtained by any other means than measurement.

Type A Uncertainties

The statistical determination of uncertainty relies upon a sample including multiple measurements of a quantity. These measurements can be averaged over the number of total measurements taken providing the arithmetic mean, the standard deviation or spread of values can then be determined from the differences between each data point and the mean. Suppose we have some measured quantity x measured n number of times, the arithmetic mean is determined by Eq. B.1.

$$\mu(x) = \frac{1}{n}\sum_{i=1}^{n} x_i \tag{B.1}$$

The standard deviation of these measurements is then given as Eq. B.2

$$\sigma(x) = \sqrt{\frac{1}{n-1}\sum_{i=1}^{n}(x_i - \bar{x})^2} \tag{B.2}$$

Finally an experimental standard deviation can be determined, which is an estimate of how far the sample mean is likely to be from the population mean, and therefore how representative the mean of our measurement is in relation to all possible measurements in the population. The experimental standard deviation is given by Eq. B.3

$$s(\bar{x}) = \frac{\sigma(x)}{\sqrt{n}} \tag{B.3}$$

When working with data set where data points are normalized by another given data point, the relative uncertainty (u_r) is a useful quantity as it allows for the calculation of uncertainty of the normalized quantity. The relative uncertainty is determined using Eq. B.4.

$$u_r = \frac{s(\bar{x})}{\mu} \tag{B.4}$$

This thesis relies upon the determination of normalized profiles and TPRs, the relative uncertainty is therefore useful in the determination of the associated uncertainties, therefore allowing for appropriate discussion and conclusions to be drawn from analysed data. Finally the type A uncertainty, whether relative or absolute will be expressed as the quantity u_A.

Type B Uncertainties

Type B uncertainties are those not calculated through statistical analysis. Instead they can only be estimated from a variety of sources. These include manufacturers specifications, data provided in calibration certificates, experience with or general knowledge of the behaviour and properties of materials and instruments, uncertainties from reference data in literature, etc. Type B uncertainties can be reduced by improvement in equipment, better understanding of measurement apparatus and setup. The estimated type B uncertainties for a measurement is expressed as the quantity u_B.

Combined Uncertainty

Given that no correlation exists between type A and type B uncertainties for a particular set of measurements, these can be combined in quadrature to determine total measurement uncertainty. This combined uncertainty is given by Eq. B.5.

$$u_c = \sqrt{u_A^2 + u_B^2} \tag{B.5}$$

It is important to note that if u_A is expressed as a relative uncertainty, then u_B must also be expressed as a relative uncertainty. Then the total absolute uncertainty u_c is computed by multiplying the combined relative uncertainties by the mean value of quantity measured. Throughout this thesis, the uncertainty in measured quantities is either determined or assumed to be based on a gaussian distribution, therefore a coverage factor of $k = 2$ is applied by ku_c to achieve a 95 % confidence level.

Appendix C

Electrometer Temporal Resolution Validation Code

```
# Packages required: numpy, matplotlib, pyvisa (pip install -U pyvisa) and pyvisa-py (pip install -U pyvisa-py)
import visa
import time
import datetime
import re
import numpy
import time
import matplotlib.pyplot as plt

rm = visa.ResourceManager()
print(rm.list_resources())

comport = input("Please input COM Number from list above i.e. for ASRLCOM5::INSTR the COM number is 5: ")

inst = rm.open_resource("ASRLCOM"+str(comport)+"::INSTR",baud_rate = 19200)

iters = 100 # Total Number of iterations to grab data for
charge = [0]
current = [0]
timeelapsed = [0]

starttime = time.time() # Starting time in s
start = inst.query("STA")
```

```
for ii in range(0,iters):

    print(ii)

    t = time.time()
    elapsed = t-starttime
    drdata = inst.query("D1") #Dose rate query
    qdata = inst.query("D0") # Charge Query

    current.append(float(re.split(';',drdata)[5]))
    charge.append(float(re.split(';',qdata)[5]))

    timeelapsed.append(elapsed)

hold = inst.query("HLD")
reset = inst.query("RES")

charge = numpy.array(charge) * (10**9) # Convert charge from C to nC
current = numpy.array(current) * (10**9) # Convert current from A to nA

inst.close() # Close instance of COMX

plt.plot(timeelapsed,current,'.')
plt.plot(timeelapsed,current)
plt.ylabel('Current (nA)')
plt.xlabel('time (s)')
plt.title('Current vs time with 3.3 Hz Square Wave Signal 3Vpp amplitude')
plt.show()

plt.plot(timeelapsed,charge,'.')
plt.plot(timeelapsed,charge)
plt.ylabel('Charge (nC)')
plt.xlabel('time (s)')
plt.title('Charge vs time with 3.3 Hz Square Wave Signal 3Vpp amplitude')
plt.show()
```

Appendix D

TBIControl Source Code Release

The TBIControl software developed during this project is open-source. The entire code base was written over a one week period and is therefore not perfectly optimized in terms of multi-threading and code abstraction. There are thousands of lines of code which have been written and as such have been committed to a Github repository for full access of the code and compiled binary application. I fully support any centres/individuals who wish to use and extend/improve the code and therefore will keeping up to date with any pull requests submitted and merging changes appropriately. The release and source code can be found at: `https://github.com/Phillip-Duncan/TBIControl/releases`.

Bibliography

1. Radiology Support Devices Inc. The Alderson Radiation Therapy Phantom. URL http://rsdphantoms.com/radiation-therapy/the-alderson-radiation-therapy-phantom/.

2. New Zealand Ministry of Health. Cancer new registrations and deaths 2013. *New Zealand Ministry of Health*, 2013. URL https://www.moh.govt.nz/notebook/nbbooks.nsf/0/8B3C32C587F377194C2565D7000E0C67/$file/cancer-new-registrations-deaths-2013-nov16.pdf.

3. New Zealand Government Statistics. Births and Deaths: Year Ended December 2013. *Wellington: Stats NZ*, 2013. URL http://archive.stats.govt.nz/browse_for_stats/population/births/BirthsAndDeaths_HOTPYeDec13.aspx.

4. Geoff Delaney, Susannah Jacob, Carolyn Featherstone, and Michael Barton. The role of radiotherapy in cancer treatment. *Cancer*, 104(6):1129–1137, 9 2005. ISSN 0008-543X. doi: 10.1002/cncr.21324. URL https://doi.org/10.1002/cncr.21324.

5. Carson Wills, Sheen Cherian, Jacob Yousef, Kelin Wang, and Heath Mackley. Total body irradiation: A practical review. *Applied Radiation Oncology*, 2:11–17, 6 2016.

6. J.M. Cosset, T. Girinsky, E. Malaise, M.P. Chaillet, and J. Dutreix. Clinical basis for TBI fractionation. *Radiotherapy Oncology*, 18(1):60–67, 1990. doi: 10.1016/0167-8140(90)90179-z.

7. E.D. Thomas, C.D. Buckner, R.A. Clift, and et al. Marrow transplantation for acute nonlymphoblastic leukemia in first remission. *The New England Journal of Medicine*, 301(11):597–599, 1979. doi: doi:10.1056/NEJM197909133011109.

8. E.D. Thomas, R.A. Clift, J. Hersman, and et al. Marrow transplantation for acute nonlymphoblastic leukemic in first remission using fractionated or single-dose irradiation. *International Journal of Radiation Oncology and Biological Physics*, 8(5):817–821, 1982.

9. Andreas Springer, Josef Hammer, Erwin Winkler, Christine Track, Roswitha Huppert, Alexandra Böhm, Hedwig Kasparu, Ansgar Weltermann, Gregor Aschauer, Andreas L Petzer, Ernst Putz, Alexander Altenburger, Rainer Gruber, Karin Moser, Karin Wiesauer, and Hans Geinitz. Total body irradiation with volumetric modulated arc therapy: Dosimetric data and first clinical experience.

Radiation oncology (London, England), 11:46, 3 2016. doi: 10.1186/s13014-016-0625-7. URL https://www.ncbi.nlm.nih.gov/pubmed/27000180.

10. Petra M Härtl, Marius Treutwein, Matthias G Hautmann, Manuel März, Fabian Pohl, Oliver Kölbl, and Barbara Dobler. Total body irradiationâan attachment free sweeping beam technique. *Radiation Oncology*, 11(1):81, 2016. ISSN 1748-717X. doi: 10.1186/s13014-016-0658-y. URL https://doi.org/10.1186/s13014-016-0658-y.

11. Amjad Hussain, Jose Eduardo Villarreal-Barajas, Peter Dunscombe, and Derek W Brown. Aperture modulated, translating bed total body irradiation. *Medical Physics*, 38(2):932–941, 2 2011. ISSN 0094-2405. doi: 10.1118/1.3534196. URL https://doi.org/10.1118/1.3534196.

12. Ulrich Quast. Whole body radiotherapy: A TBI-guideline. *Journal of medical physics*, 31(1):5–12, 2006. doi: 10.4103/0971-6203.25664. URL https://www.ncbi.nlm.nih.gov/pubmed/21206634.

13. J. Van Dyk, J. M. Galvin, G. P. Glasgow, and E. B. Podgorsak. *AAPM Report No. 017 - The Physical Aspects of Total and Half Body Photon Irradiation*. 1986. ISBN 978-0-883185-13-1.

14. Iris Rusu. Total Body Irradiation (TBI). In Luther W Brady and Theodore E Yaeger, editors, *Encyclopedia of Radiation Oncology*, pages 904–910. Springer Berlin Heidelberg, Berlin, Heidelberg, 2013. ISBN 978-3-540-85516-3. doi: 10.1007/978-3-540-85516-3{_}38. URL https://doi.org/10.1007/978-3-540-85516-3_38.

15. G Narayanasamy, C Bosse, D Saenz, W Cruz, P Mavroidis, N Papanikolaou, and S Stathakis. SU-E-T-194: Commissioning of Monaco Treatment Planning System On An Elekta VersaHD Linear Accelerator. *Medical Physics*, 42(6Part14):3376, 6 2015. ISSN 0094-2405. doi: 10.1118/1.4924555. URL https://doi.org/10.1118/1.4924555.

16. Jeffrey E Snyder, Daniel E Hyer, Ryan T Flynn, Amanda Boczkowski, and Dongxu Wang. The commissioning and validation of Monaco treatment planning system on an Elekta VersaHD linear accelerator. *Journal of Applied Clinical Medical Physics*, 20(1):184–193, 1 2019. ISSN 1526-9914. doi: 10.1002/acm2.12507. URL https://doi.org/10.1002/acm2.12507.

17. J López-Tarjuelo, R García-Mollá, X J Juan-Senabre, J D Quirós-Higueras, A Santos-Serra, N de Marco-Blancas, and S Calzada-Feliu. Acceptance and Commissioning of a Treatment Planning System Based on Monte Carlo Calculations. *Technology in Cancer Research & Treatment*, 13(2):129–138, 4 2014. ISSN 1533-0346. doi: 10.7785/tcrt.2012.500361. URL https://doi.org/10.7785/tcrt.2012.500361.

18. Roumiana Chakarova and Marcus Krantz. A Monte Carlo evaluation of beam characteristics for total body irradiation at extended treatment distances. *Journal of applied clinical medical physics*, 15(3):4708, 5 2014. ISSN 1526-9914. doi: 10.1120/jacmp.v15i3.4708. URL https://www.ncbi.nlm.nih.gov/pubmed/24892344https://www.ncbi.nlm.nih.gov/pmc/articles/PMC5711064/.

19. Marie-Claude Lavallée, Luc Gingras, Mario Chrétien, Sylviane Aubin, Carl Côté, and Luc Beaulieu. Commissioning and evaluation of an extended SSD photon model for PINNACLE3: An application to total body irradiation. *Medical Physics*, 36(8):3844–3855, 8 2009. doi: 10.1118/1.3171688. URL https://doi.org/10.1118/1.3171688.

20. Narottam Lamichhane, Vivek N Patel, and Matthew T Studenski. Going the distance: validation of Acuros and AAA at an extended SSD of 400 cm. *Journal of Applied Clinical Medical Physics*, 17(2):63–73, 3 2016. ISSN 1526-9914. doi: 10.1120/jacmp.v17i2.5913. URL https://doi.org/10.1120/jacmp.v17i2.5913.

21. P. Duncan-Gelder. Feasibility of modelling extended SSD and large field dosimetry in Monaco for Total Body Irradiation (TBI). Hamilton, New Zealand, 2020. New Zealand Physics and Engineering and Medicine (NZPEM).

22. Ervin Podgorsak. Radiation Oncology Physics: A Handbook for Teachers and Students. *Medical Physics*, 33:1920, 6 2006. doi: 10.1118/1.2201870.

23. Ervin Podgorsak. Radiation Physics for Medical Physicists. 1 2016. doi: 10.1007/978-3-319-25382-4.

24. F M Khan. *The Physics of Radiation Therapy*. LWW Doody's all reviewed collection. Lippincott Williams & Wilkins, 2003. ISBN 9780781730655. URL https://books.google.co.nz/books?id=hmbbyF9ZHo8C.

25. H E Johns and J R Cunningham. *The Physics of Radiology*. American Lecture Series, Publication No. 932. a Monograph in. Thomas, 1974. ISBN 9780398030070. URL https://books.google.co.nz/books?id=7DprAAAAMAAJ.

26. Robert F Cleveland and Jerry L Ulcek. Questions and Answers about Biological Effects and Potential Hazards of Radiofrequency Electromagnetic Fields. *Office of Engineering and Technology Federal Communications Commission Washington, D.C. 20554*, 4, 1999. URL https://transition.fcc.gov/Bureaus/Engineering_Technology/Documents/bulletins/oet56/oet56e4.pdf.

27. J. H. Hubbell. Photon cross section attenuation coefficients,and energy absorption coefficients from 10 keV to 100 GeV. *US National Bureau of Standards*, 29, 1969. URL https://nvlpubs.nist.gov/nistpubs/Legacy/NSRDS/nbsnsrds29.pdf.

28. K Horikawa, S Miyamoto, T Mochizuki, S Amano, D Li, K Imasaki, Y Izawa, K Ogata, S Chiba, and T Hayakawa. Neutron angular distribution in (γ, n) reactions with linearly polarized γ-ray beam generated by laser Compton scattering. *Physics Letters B*, 737:109–113, 2014. ISSN 0370-2693. doi: https://doi.org/10.1016/j.physletb.2014.08.024. URL http://www.sciencedirect.com/science/article/pii/S0370269314005917.

29. Joe Deasy. ICRU Report 49, Stopping Powers and Ranges for Protons and Alph Particles. *Medical Physics*, 21(5):709–710, 5 1994. doi: 10.1118/1.597176. URL https://doi.org/10.1118/1.597176.

30. M J Berger, M Inokuti, H H Anderson, H Bichsel, J A Dennis, D Powers, S M Seltzer, and J E Turner. ICRU Report 37 Stopping Powers for Electrons and Positrons. *Journal of the International Commission on Radiation Units and Measurements*, os19(2):NP–NP, 4 2016. doi: 10.1093/jicru/os19.2.Report37. URL https://doi.org/10.1093/jicru/os19.2.Report37.

31. P. Andreo, D. Burns, K. Hohlfeld, M. Huq, T. Kanai, F. Laitano, V. Smyth, and S. Vynckier. IAEA TRS-398: Absorbed Dose Determination in External Beam Radiotherapy An International Code of Practice for Dosimetry based on Standards of Absorbed Dose to Water. *IAEA*, 12(1), 2006. URL http://www-naweb.iaea.org/nahu/DMRP/documents/CoP_V12_2006-06-05.pdf.

32. R C MURTY. Effective Atomic Numbers of Heterogeneous Materials. *Nature*, 207(4995):398–399, 1965. ISSN 1476-4687. doi: 10.1038/207398a0. URL https://doi.org/10.1038/207398a0.

33. Hideharu Miura, Shuichi Ozawa, Fumika Hosono, Naoki Sumida, Toshiya Okazue, Kiyoshi Yamada, and Yasushi Nagata. Gafchromic EBT-XD film: Dosimetry characterization in high-dose, volumetric-modulated arc therapy. *Journal of Applied Clinical Medical Physics*, 17(6):312–322, 11 2016. doi: 10.1120/jacmp.v17i6.6281. URL https://doi.org/10.1120/jacmp.v17i6.6281.

34. Antony Palmer, Alexis Dimitriadis, Andrew Nisbet, and Catharine Clark. Evaluation of Gafchromic EBT-XD film, with comparison to EBT3 film, and application in high dose radiotherapy verification. *Physics in medicine and biology*, 60:8741–8752, 10 2015. doi: 10.1088/0031-9155/60/22/8741.

35. Suphalak Khachonkham, Ralf Dreindl, Gerd Heilemann, Wolfgang Lechner, Hermann Fuchs, Hugo Palmans, Dietmar Georg, and Peter Kuess. Characteristic of EBT-XD and EBT3 radiochromic film dosimetry for photon and proton beams. *Physics in Medicine & Biology*, 63(6):065007, 2018. ISSN 1361-6560. doi: 10.1088/1361-6560/aab1ee. URL http://dx.doi.org/10.1088/1361-6560/aab1ee.

36. N. Reynaert, S. van der Marck, D. Schaart, W. van der Zee, M. Tomsej, C. van Vliet-Vroegindeweij, J. Jansen, M. Coghe, C. De Wagter, and B. Heijmen. Monte Carlo Treatment Planning - An Introduction. Technical report, Netherlands Commission on Radiation Dosimetry, Netherlands, 2006.

37. Woong Cho, Tae-Suk Suh, Jeong-Hoon Park, Lei Xing, and Jeong-Woo Lee. Practical implementation of a collapsed cone convolution algorithm for a radiation treatment planning system. *Journal of the Korean Physical Society*, 61(12):2073–2083, 2012. ISSN 1976-8524. doi: 10.3938/jkps.61.2073. URL https://doi.org/10.3938/jkps.61.2073.

38. Anders Ahnesjö. Collapsed cone convolution of radiant energy for photon dose calculation in heterogeneous media. *Medical Physics*, 16(4):577–592, 7 1989. ISSN 0094-2405. doi: 10.1118/1.596360. URL https://doi.org/10.1118/1.596360.

39. Keyvan Jabbari. Review of fast monte carlo codes for dose calculation in radiation therapy treatment planning. *Journal of medical signals and sensors*, 1(1):73–86, 1 2011. ISSN 2228-7477. URL https://pubmed.ncbi.nlm.nih.gov/22606661https://www.ncbi.nlm.nih.gov/pmc/articles/PMC3317764/.

40. Sun Nuclear Corporation. Solid Water HE, 2019. URL https://www.sunnuclear.com/products/solid-water-he/.

41. Sun Nuclear Corporation. Original Solid Water, 2019. URL https://www.sunnuclear.com/shopgammex/original-solid-water/.

42. Phoenix Dosimetry Ltd. NE2571 and NE2581 Ionisation Chambers. URL http://mail.phoenix-dosimetry.co.uk/drupal/?q=2571.

43. CNMC. UNIDOS® E Field-Class Electrometer/Dosimeter. URL http://www.teambest.com/CNMC_docs/radPhysics/electrometers/CNMC_T10010.pdf.

44. PTW Freiburg GmbH. Water Phantom 41023 for Horizontal Beams. URL https://www.ptwdosimetry.com/en/products/water-phantom-41023-for-horizontal-beams/.

45. Elekta AB. Elekta Synergy, 2020. URL https://www.elekta.com/radiotherapy/treatment-delivery-systems/elekta-synergy/.

46. Elekta AB. Elekta Versa HD, 2020. URL https://www.elekta.com/radiotherapy/treatment-delivery-systems/versa-hd/.

47. Gerald J Kutcher, Lawrence Coia, Michael Gillin, William F Hanson, Steven Leibel, Robert J Morton, Jatinder R Palta, James A Purdy, Lawrence E Reinstein, Goran K Svensson, Mona Weller, and Linda Wingfield. Comprehensive QA for radiation oncology: Report of AAPM Radiation Therapy Committee Task Group 40. *Medical Physics*, 21(4):581–618, 4 1994. ISSN 0094-2405. doi: 10.1118/1.597316. URL https://doi.org/10.1118/1.597316.

48. Eric E Klein, Joseph Hanley, John Bayouth, Fang-Fang Yin, William Simon, Sean Dresser, Christopher Serago, Francisco Aguirre, Lijun Ma, Bijan Arjomandy, Chihray Liu, Carlos Sandin, and Todd Holmes. Task Group 142 report: Quality assurance of medical accelerators. *Medical Physics*, 36 (9Part1):4197–4212, 9 2009. doi: 10.1118/1.3190392. URL https://doi.org/10.1118/1.3190392.

49. Ioannis Tsalafoutas, S Xenofos, A Papalexopoulos, and Stylianos Nikoletopoulos. Dose calculations for asymmetric fields defined by independent collimators using symmetric field data. *The British journal of radiology*, 73:403–409, 5 2000. doi: 10.1259/bjr.73.868.10844866.

50. Alicia Moggré and Ben Wilder. Total Body Irradiation (TBI) Recommissioning Report. *Christchurch Hospital, Canterbury District Health Board. Christchurch, New Zealand*, 2017.

51. Alicia Moggré and Ben Wilder. Total Body Irradiation Protocol. *Christchurch Hospital, Canterbury District Health Board. Christchurch, New Zealand*, (15), 2017.

52. Shu-Hui Hsu, Jean M Moran, Yu Chen, Ravi Kulasekere, and Peter L Roberson. Dose discrepancies in the buildup region and their impact on dose calculations for IMRT fields. *Medical physics*, 37(5): 2043–2053, 5 2010. ISSN 0094-2405. doi: 10.1118/1.3377769. URL `https://pubmed.ncbi.nlm.nih.gov/20527537https://www.ncbi.nlm.nih.gov/pmc/articles/PMC2866257/`.

53. Benedick Fraass, Karen Doppke, Margie Hunt, Gerald Kutcher, George Starkschall, Robin Stern, and Jake Van Dyke. American Association of Physicists in Medicine Radiation Therapy Committee Task Group 53: Quality assurance for clinical radiotherapy treatment planning. *Medical Physics*, 25(10):1773–1829, 10 1998. ISSN 0094-2405. doi: 10.1118/1.598373. URL `https://doi.org/10.1118/1.598373`.

54. Joint Committee For Guides In Metrology Jcgm. Evaluation of measurement data â Guide to the expression of uncertainty in measurement. *International Organization for Standardization Geneva ISBN*, 50(September):134, 2008. ISSN 00099147. doi: 10.1373/clinchem.2003.030528. URL `http://www.bipm.org/en/publications/guides/gum.html`.